NBS MONOGRAPH   130

The Divergent Beam (Kossel) X-Ray Method and Its Uses in Measuring Strain Contours in an Individual Grain of Fe-3 Weight Percent Si Transformer Sheet

NATIONAL BUREAU OF STANDARDS

The National Bureau of Standards [1] was established by an act of Congress March 3, 1901. The Bureau's overall goal is to strengthen and advance the Nation's science and technology and facilitate their effective application for public benefit. To this end, the Bureau conducts research and provides: (1) a basis for the Nation's physical measurement system, (2) scientific and technological services for industry and government, (3) a technical basis for equity in trade, and (4) technical services to promote public safety. The Bureau consists of the Institute for Basic Standards, the Institute for Materials Research, the Institute for Applied Technology, the Institute for Computer Sciences and Technology, and the Office for Information Programs.

THE INSTITUTE FOR BASIC STANDARDS provides the central basis within the United States of a complete and consistent system of physical measurement; coordinates that system with measurement systems of other nations; and furnishes essential services leading to accurate and uniform physical measurements throughout the Nation's scientific community, industry, and commerce. The Institute consists of a Center for Radiation Research, an Office of Measurement Services and the following divisions:

Applied Mathematics — Electricity — Mechanics — Heat — Optical Physics — Nuclear Sciences [2] — Applied Radiation [2] — Quantum Electronics [3] — Electromagnetics [3] — Time and Frequency [3] — Laboratory Astrophysics [3] — Cryogenics [3].

THE INSTITUTE FOR MATERIALS RESEARCH conducts materials research leading to improved methods of measurement, standards, and data on the properties of well-characterized materials needed by industry, commerce, educational institutions, and Government; provides advisory and research services to other Government agencies; and develops, produces, and distributes standard reference materials. The Institute consists of the Office of Standard Reference Materials and the following divisions:

Analytical Chemistry — Polymers — Metallurgy — Inorganic Materials — Reactor Radiation — Physical Chemistry.

THE INSTITUTE FOR APPLIED TECHNOLOGY provides technical services to promote the use of available technology and to facilitate technological innovation in industry and Government; cooperates with public and private organizations leading to the development of technological standards (including mandatory safety standards), codes and methods of test; and provides technical advice and services to Government agencies upon request. The Institute consists of a Center for Building Technology and the following divisions and offices:

Engineering and Product Standards — Weights and Measures — Invention and Innovation — Product Evaluation Technology — Electronic Technology — Technical Analysis — Measurement Engineering — Structures, Materials, and Life Safety [4] — Building Environment [4] — Technical Evaluation and Application [4] — Fire Technology.

THE INSTITUTE FOR COMPUTER SCIENCES AND TECHNOLOGY conducts research and provides technical services designed to aid Government agencies in improving cost effectiveness in the conduct of their programs through the selection, acquisition, and effective utilization of automatic data processing equipment; and serves as the principal focus within the executive branch for the development of Federal standards for automatic data processing equipment, techniques, and computer languages. The Center consists of the following offices and divisions:

Information Processing Standards — Computer Information — Computer Services — Systems Development — Information Processing Technology.

THE OFFICE FOR INFORMATION PROGRAMS promotes optimum dissemination and accessibility of scientific information generated within NBS and other agencies of the Federal Government; promotes the development of the National Standard Reference Data System and a system of information analysis centers dealing with the broader aspects of the National Measurement System; provides appropriate services to ensure that the NBS staff has optimum accessibility to the scientific information of the world. The Office consists of the following organizational units:

Office of Standard Reference Data — Office of Technical Information and Publications — Library — Office of International Relations.

---

[1] Headquarters and Laboratories at Gaithersburg, Maryland, unless otherwise noted; mailing address Washington, D.C. 20234.
[2] Part of the Center for Radiation Research.
[3] Located at Boulder, Colorado 80302.
[4] Part of the Center for Building Technology.

The Divergent Beam (Kossel) X-Ray Method and Its Uses in Measuring Strain Contours in an Individual Grain of Fe-3 Weight Percent Si Transformer Sheet

Harvey Yakowitz

Metallurgy Division
Institute for Materials Research
National Bureau of Standards
Washington, D.C. 20234

Contents

The Divergent Beam (Kossel) X-Ray Method and Its Uses in Measuring Strain Contours in an Individual Grain of Fe-3 Weight Percent Si Transformer Sheet

Harvey Yakowitz

Residual and impressed stresses and strains in Fe-3 wt% Si alloy transformer sheet were studied. Results were obtained by the divergent beam (Kossel) x-ray microdiffraction techniques. The optically opaque Fe-3 wt% Si alloy was mapped for residual and impressed stresses and strains. These maps are roughly analogous to polarized light stress analysis of transparent materials. The results showed that a variable strain distribution existed in the alloy sheet at the time it was ready for insertion into a transformer core. Small applied compressive and tensile loads tended to rearrange this variable strain distribution but not to appreciably alter the total stored elastic energy.

Key words: Divergent beam x-ray diffraction; electron probe microanalysis; iron-silicon alloy; Kossel; strain; stress; transformer sheet.

I. Introduction

Iron alloyed with about 3 percent by weight of silicon (Fe-3 Si) is one of the most important commercial materials used in the electrical industry. This alloy is used as core material in virtually all transformers presently manufactured. In fact, Fe-3 Si has been used in transformers since the early part of the century. As with most commercial materials, steady improvements in the material were made with the primary goal being to eliminate or, more realistically, to reduce to the lowest practical level hysteresis losses in the transformer core.

A prime source for the power losses is that ferromagnetic crystals are very anisotropic in their behavior. Body centered cubic (BCC) Fe-3 Si has the $\langle 100 \rangle$ directions (the cube edges) as its easy magnetization directions. Thus, a relatively low field in any edge direction will magnetize Fe-3 Si to saturation. All other directions are more difficult to magnetize; they cost more input energy for the same result. For these reasons, Goss [1][1] correctly postulated that producing Fe-3 Si having a special grain orientation would reduce power losses.

In Goss Fe-3 Si, the (110) plane is made parallel to the rolling direction which is the [001] direction. This preferred orientation is achieved by secondary recrystallization. Today the power loss at 50 Hz and 15 kG is about 0.4 to 0.5 watts/pound for 12 mil (0.305

mm) thick laminations when this material is used in transformers. This material has been in continuous use since 1937.

In 1957, the so-called cube texture denoted by (100) [001] orientation was developed by Assmus [2]. This material has almost equal magnetic properties in two directions at right angles within the sheet. Power losses can be reduced and the transformer designer has a bit more latitude in working with this material. But the manufacturing process for the cube texture is more expensive and difficult than that for the Goss texture. Thus, an economic balancing act of improved performance savings versus increased material costs must be performed. At present, economic considerations still favor the Goss texture for most applications. Hence, the material chosen for study here is the Goss oriented Fe-3 Si. For orientation purposes, the two textures are shown schematically in figure 1.[2]

Low level stresses in Goss Fe-3 Si can appreciably alter both power losses and magnetostriction [3,4]. Hysteresis losses pass through a minimum at tensile stresses of a few hundred psi [3,5]. This result suggests that inhomogeneous residual stresses may be present in the original material which is coarse-grained $(>1$ mm$)$ polycrystalline sheet. The presence of the grain boundaries is known to increase average power loss as well [5]. Another source of loss is that temperature gradients of up to 200 °C can occur between the center and the edge of

---

[1] Italicized figures in brackets indicate the literature references on pages 36 and 37.

[2] All figures are at the end of this publication beginning on page 60.

1

a transformer core. These in turn can generate internal stresses in the core laminates of 400 to 500 psi. Stresses above 500 psi (0.35 MN/m²) cause power losses to increase rapidly [4].

To date, no one has correlated quantitative local stress-strain characteristics in Fe-3 Si with the relatively large amount of electrical property data now available. There is at least one good experimental method available for locally determining the strain state of individual grains in a polycrystalline material—the divergent beam diffraction method usually referred to as the Kossel method [6]. With this method, the entire thickness of the transformer sheet can be sampled; the total volume of crystal sampled is only about 200 μm³ for 3 mil (0.076 mm) thick Fe-3 Si sheet.

The Kossel method can be made to yield data giving (1) lattice strains, (2) Cauchy strains, (3) principal strains, (4) principal strain axes, (5) maximum shear strain in any (hkl) plane (known), (6) principal stresses, (7) principal stress axes, and (8) total stored elastic energy in the irradiated region of the crystal. These quantities can be determined to within a probable error of about ± 10 percent relative.

The stress-strain configuration at individual regions within a grain of a polycrystalline sheet can thus be investigated by the Kossel method. However, such studies have not been carried out previously on any material. In any study of local stress-strain variations, possible variations in chemical composition must be taken into account. Electron probe microanalysis can be used to correlate local variations in Si content with the stress-strain data.

II. Problems Relating to Fe-3 Si Transformer Sheet

Attention will now be shifted to a detailed discussion of Fe-3 Si—especially from the point of view of the effect of strain on such quantities as power losses and magnetostrictive effects. Then we shall see how information provided by the Kossel method can be meshed with the electrical information to indicate substantive explanations for some of the electrical observations.

The knowledge of the effects of stress on the magnetic and electrical properties of Fe-3 Si can be distilled into ten basic ideas as follows:

1. All experimental and theoretical studies agree that small, 0.7 MN/m² (1000 psi) stresses, either tensile or compressive, degrade the magnetic and electrical properties. For instance, compressive stresses of 0.3 MN/m² (400 psi) increase power losses by 20 to 30 percent [4].

2. There is the belief that small residual stresses, say 0.1 to 0.35 MN/m² (100 to 500 psi), remain in the material that is used commercially [3,4,5].

3. Certain observed improvements in the magnetic and electrical properties occurring after externally applied stresses of 0.1 to 0.35 MN/m² (100 to 500 psi) are thought to result from overcoming residual stress effects.

4. It has been predicted theoretically [7] and shown experimentally [8] that the magnetization curve (**B** vs **H**) deteriorates under applied tensile stresses. Consequently, both hysteresis and power losses can be expected to increase with increasing tensile stress [4].

5. Magnetic domain studies at low values of applied stress [9,10,11] show complete domain rearrangement as the stress level is increased to 0.7 to 1.4 MN/m² (1000 to 2000 psi). New domain structures appear to be completely established at 1.4 MN/m² (2000 psi) [9]. However, observable domain structures are, of necessity, surface domains. Thus, no information is available on domain configurations within the Fe-3 Si sheet. Therefore, any attempt to explain the effect of applied macrostresses in terms of local events within the Fe-3 Si sheet is open to question.

6. The magnetization, **B**, degrades more rapidly under compression as compared to tension [4].

7. Magnetostrictive strain increases rapidly with compressive stress but falls to and remains nearly zero at tensile stresses of 200 psi or more [12].

8. Power losses are apt to be two to three times as large at grain boundaries or at misaligned grains as they are for the average of the material [4] (see fig. 2).

9. The effect of increasing the temperature of the sheet is to cause the losses to fall by a few percent per 100 °C rise. The applied stress has little effect on this observation [4].

10. The alternating power loss in the cube edge orientation is only slightly less than that of the Goss oriented Fe-3 Si.

In brief, stresses always cause problems. There are some clues as to the cause of these problems based on domain structure studies. There is also evidence that the effect of the stresses is not

2

homogeneous. The latter point tends to indicate that the stresses cannot be homogeneously distributed.

Why would stresses—residual or purposely applied—originate in the commercial Fe-3 Si sheets? In order to answer this question, it is necessary to look briefly at the method of preparation of the material and also at the way the finished Fe-3 Si sheets are used. Figure 3 is a flow sheet showing the basic steps in the production of the sheets. The portions which need to be examined in more detail are the 1200 °C batch anneal and, to a lesser extent, the thermal flattening process. The former is of interest since it is in this step that the desired texture is developed, while the latter is a process which may introduce stresses.

The initiation of the growth of the Goss texture occurs, to a large extent, as a result of the presence of a suitably dispersed second phase (usually MnS, but lately Si_3N_4 has been used) which allows the desired secondary texture (Goss) to begin to develop and grow. Naturally, it is necessary for there to be some correctly oriented grains in the primary texture. The dispersion of the second phase impurity is controlled by the cooling rate from the solution temperature during the hot-rolling step. Some of the sulfur bearing impurities are removed during the final anneal by a reaction involving the coating.

Once the secondary recrystallization is begun, the Fe-3 Si strips are brought to the 1200 °C annealing temperature. The batch anneal is best carried out in alumina tubes of the highest purity obtainable. At 1200 °C, the (110) crystals grow rapidly so that the secondary recrystallization is completed quickly. The 1200 °C anneal favors the Goss orientation; lower annealing temperatures favor the (100) [001] texture [13]. Furthermore, the Goss orientation grows more rapidly and more easily in thin, ≤ 0.3 mm, (12 mil) Fe-3 Si sheets than in thicker sheets.

These observations can be explained using Mullins' theory [14]. The orientation relationships between the primary and the secondary—very large—grains are consistent with the dependence of surface free-energy on orientation. Surface free-energy unbalances will produce growth of large textured grains. May and Turnbull [15] postulated that the (110) [001] grains have the lowest average surface free-energies of all the grains. It has been found that the large grained texture type growth occurs most easily at the surface [14]. As Mullins puts it, a low surface-energy crystal wets the surface of the Fe-3 Si sheet from underneath. The dispersed phase inhibits normal grain growth of the primary recrystallized matrix. Thus, the required surface energy unbalance is provided and the (110) [001] grain boundary is released for growth. When the sheet is brought to 1200 °C, the surface tension at the boundary is the driving force for the rapid completion of the secondary recrystallization. For undisturbed surface conditions, the close packed (110) crystal plane is then preferred [14]. This hypothesis fits the observation that the Goss orientation grows more favorably in thin sheets since there the boundary is under greater surface tension and hence will migrate more rapidly [13]. The end result is a coarse-grained Goss oriented texture containing 85 to nearly 100 percent of (110) [001] grains.

Apparently, the interaction of the energetic relations favoring the growth of the desired texture is very critical. A small cold-rolling strain applied after primary recrystallization but before the texture anneal causes the (110) [001] orientation to be almost nonexistent [15].

After the texture-anneal is complete, a thermal flattening process is carried out. This is necessary so that no compressive stresses are introduced during actual transformer construction. For thermal flattening, tension is applied while the strip is at a temperature of 400-500 °C. A stress-relief anneal is then carried out and the sheet is ready for use.

In view of the findings about the deleterious effects of small stresses and the observation that the electrical properties vary with test position in the sheet, the stress distribution within the sheet would seem to be of great importance. Especially of interest is whether or not any residual stress rises to a maximum near or at grain boundaries in the sheet or whether or not these stresses are compressive or tensile in nature. If residual stresses are predominantly compressive in nature, the sheet can be placed under an external tensile load in order to see if the overall stress-strain configuration tends toward a no-stress condition. This would not only confirm the conjecture that such a rearrangement occurs; it would also show how the rearrangement occurs. Of course, the question "Why are the residual stresses predominantly compressive even after the (tensile) thermal flattening step and process annealing?" would remain to be considered. A knowledge of the possible local variation of silicon content within the grains of the sheet is of great interest in considering such a question. The addition of Si to the Fe lattice causes an overall shrinkage of the unit cell of the lat-

3

tice; figure 4 shows the unit cell size versus percentage Si added. Thus, an inhomogeneous Si distribution might be expected to create very definite local lattice strains.

A set of definitive experiments aimed at answering the foregoing questions was designed. The Kossel method was used to evaluate local stress-strain configurations in the as-received Fe-3 Si sheet. Then, with an appropriate tensile loading device available, low tensile stresses were applied in order to observe their effect on the original stress-strain configuration. Naturally, the same regions were studied in these tests. Finally, local Si content variations were observed by means of electron probe microanalysis. The desired result was to obtain a point-by-point local analysis for Si within the grain.

At the time this study was first contemplated (1963), the Kossel method was still largely a laboratory curiosity. However, in recent years the technique has been developed to the point where reliable measurements can be made in a fairly routine manner.

III. The Kossel Method

A. The Observed Diffraction Pattern

The Kossel and pseudo-Kossel methods can be employed for generating divergent beam x-ray patterns. In the Kossel method, the x-ray source is excited within the specimen itself by a focused electron probe or a collimated x-ray beam of suitable energy. In this case, the atoms of the crystal act as independent sources of monochromatic radiation, and the waves diverging from these excited atoms will be diffracted by atom planes of the lattice. The effect of such diffraction is to give rise to a wavefield which exits from the crystal and in which the radial directions lying at the Bragg angle, θ, with respect to the diffracting planes form right circular cones. Thus, the external wave-field may be considered to lie on the loci of a set of cones rigidly fixed to the source of x-ray excitation. A flat film intercepting this system of waves shows a set of conic sections superimposed upon a general background blackening. The axis of any specific cone is the normal to its plane of diffraction; the semi-apex angle of such a cone is $(90° - \theta)$, where θ is the Bragg angle.

The attenuation of the diverging primary beam is often greatly increased along the set of cone elements by the x-ray extinction effects produced within the crystal. Whether the appropriate extinction effect is purely due to primary or secondary extinction or, as is most likely, a combination of both, depends upon the state of perfection of the specimen crystal. This point will be examined in detail later. For the present discussion, it is sufficient to state that the primary beam radiation transmitted by the crystal may be deficient in intensity along the cone elements. Therefore, a film placed to intercept the transmitted radiation will often show conic sections lighter than the general background; these are called deficiency conics.

Furthermore, diffracting planes will lie at some angle, Φ, with respect to the crystal surface nearest the source (the entrance surface). If Φ is greater than the Bragg angle, θ, then a diffraction conic containing an excess of energy with respect to the background may be observed in the transmission pattern. Hence, both dark and light conics may be expected on a transmission pattern.

In back-reflection, the film is placed on the same side of the crystal as the source. Diffraction conics darker than background will be observed for planes whose Bragg angle, θ, is greater than the angle Φ in the case of crystals having an appreciable mosaic spread, ζ. For a perfect crystal in which ζ is negligible, conics or portions of conics may appear lighter than background.

Figure 5, taken from Sharpe [16], shows the geometry for the formation of both diffraction and deficiency conics for the case of a mosaic crystal. Note that the diffraction conic is represented as being somewhat broadened with respect to the deficiency conic. This is the case since reflection occurs from a large number of parallel planes. For each plane, there is a cone of semi-apex angle $(90 - \theta)$ but all cones have vertices displaced by one interplanar distance, d. Therefore, reflection conics are generally not as sharp as deficiency conics, all of which have the x-ray source as a common vertex [17].

Another extremely important feature is that each separate plane of a family is represented by a separate conic, i.e., there is no averaging effect as in a polycrystalline diffractometer. Thus, even in a cubic material, if the conic trace of $(\bar{h}k\bar{l})$ is seen, then the (hkl) trace also appears as a separate entity. This circumstance is the experimental keystone on which strain analysis by the Kossel method rests.

The pseudo-Kossel case is entirely analogous to the foregoing except that the source is external to the

4

sample, i.e., the apices of the cones are external to the parent crystal. In the pseudo-Kossel method, the source is usually a thin foil of the material whose radiation is desired. This source foil is either placed directly upon or slightly above the crystal of interest; the 180° divergence of x rays in the sample direction gives rise to the same behavior of the diffracted energy as in the Kossel case.

To continue this qualitative discussion of the divergent beam pattern, consider now the geometry of the conics observed on a film. Maier [18] gave the conic shape as a function of the Bragg angle and the angle Φ. These results suggest the type of pattern expected, in that θ, Φ and the observed conics are mutually dependent.

In the case where Φ is greater than θ, a hyperbola is formed. Diffracted radiation from planes lying such that Φ is greater than θ will not exit the crystal on the same side as the source. Hence, these conics will never be observed on a back reflection pattern, but rather only on a transmission photograph. Figure 5 is seen to conform in this case ($\Phi > \theta$). A deficiency conic from planes (hkl) is also formed and appears as a mirror image of the diffraction conic on the film. (In practice, a true mirror image may not be observed due to projection distortion effects on a flat film.) Lonsdale has pointed out that if both light and dark conics from planes (hkl) are recorded on the film, then complementary light and dark conics from planes $(\overline{hkl})$ will also be recorded. The dark line from planes (hkl) is parallel to the light line from planes $(\overline{hkl})$ and vice versa. The physical separation between the parallel complementary light and dark conics depends upon the distance from the x-ray source to the opposite side of the crystal taken in a direction perpendicular to the film [19].

For Φ equal to θ, a parabola results. In this case, both the back reflection and transmission patterns will show diffraction conics and in the transmission pattern a complementary deficiency conic will also be present. The probability for Φ equal to θ is extremely small for any given case.

When Φ is less than θ, ellipses occur. Any diffraction conic trace will appear only on the same side of the crystal as the source. Thus, in back reflection, a series of ellipse-like figures will be observed on the pattern. In transmission, the corresponding deficiency ellipses will result; they will be unaccompanied by complementary diffraction conics. As Ellis and Weissman pointed out, strictly speaking the curves

are of higher order than ellipses but the deviation is negligible [20].

For Φ equal to zero, a circle is obtained. This is a special case of Φ less than θ and the comments for that situation apply. It should be noted that a circular trace indicates immediately that some plane is parallel to the crystal surface which is usually placed parallel to the film.

Summarizing, a back reflection pattern of a real crystal may be expected to contain largely elliptical conics with perhaps some circular traces all of which are darker than background. A transmission pattern may contain complementary light and dark hyperbolic traces, light elliptical traces, and perhaps some light circular traces. The chances of finding a parabolic trace in either type of pattern are very slight.

To this qualitative view of the divergent beam photograph must be added considerations concerning the intensity and contrast of the conics on the film with respect to background. Contrast is spoken of rather than intensity for deficiency conics since these conics, as such, do not represent energy deposited per unit area but rather the absence of energy. Contrast is taken to mean that portion of the peak appearing above or below the general background on the film. When discussing the diffraction cones, intensity will be used as the descriptive term.

Two cases are to be considered: (1) the diffracting volume comes from a portion of the crystal having a finite mosaic spread, ζ, and (2) the diffracting volume has ζ of zero. The former will cause secondary extinction of the incident divergent x-ray beam; primary extinction may be present to some degree. The latter will cause only primary extinction to be operable and may be called "perfect" crystal volume for purposes of this discussion. Extinction exists when the measured integrated intensity of a conic is less than that predicted by the mosaic formula [21].

The following brief discussion of extinction is greatly simplified. The concept of primary and secondary extinction is itself rather idealized [21]. An extensive discussion and development of the topic will be found in James [17].

Primary extinction is usually said to operate when diffraction occurs from large "perfect" regions of the crystal. These regions may be called coherent domains or large mosaic blocks. In this case, the integrated diffracted intensity is not proportional to

5

the volume of the coherent domain. The attenuation of the primary beam is large in such a block due to multiple reflections of the beam by the perfect lattice. Instead of the usual x-ray absorption coefficient, the crystal is said to have an extinction coefficient, τ, such that $I_r/I_0 = \exp\text{-}(\pi x)$. The value of τ may be found from:

$$\tau = \frac{\pi}{2}\left(\frac{l^2}{mc^2}\right) FN'\lambda \qquad (1)$$

Calculation will show that τ is usually two to five orders of magnitude greater than the ordinary linear x-ray attenuation coefficient, μ.

Secondary extinction is said to be operable when the coherent domains are small enough so that in a single block, the effect of τ is negligible. However, the crystal is considered to be composed of a number of these smaller blocks most of which are closely parallel to one another. Hence, a loss of intensity in the primary beam is experienced by a robbing due to diffraction by properly oriented domains above the domain of interest [21].

When secondary extinction is dominant, the attenuation of a monochromatic ray of the primary beam incident upon the crystal at an angle $(\theta \pm u)$ where u is a small angular quantity is apparently enhanced. Peace and Pringle [22] have expressed this attenuation as:

$$\exp\text{-}(\mu.x) = \exp-\{2\mu + G.(u)]x\} \qquad (2)$$

Equation (2) is in effect the probability of survival of a packet of energy [22]. It is possible to define a secondary extinction coefficient "g" such that:

$$g \equiv [1/2\sqrt{2\pi}]\,[\exp\text{-}(u^2/2\zeta^2)] \qquad (3)$$

The total amount of secondary extinction present is then given by

$$G'(u) = gQ' \qquad (4)$$

Q' is the volume reflecting power of a mosaic crystal reduced by the presence of primary extinction, i.e., the actual reflecting power.

It should be noted that "g" is peculiar to the sample at hand and is not a general physical property. Furthermore, the mosaic spread, ζ, which is the root-mean-square of random rotations of small magnitude of the coherent domains about a common axis (assuming a normal distribution) will usually vary for different planes of the same crystal. Thus "g" may

be expected to vary slightly from plane to plane within the crystal. The value of Q' decreases as $\sin\theta/\lambda$ increases. Therefore, $G'(u)$ decreases as planar index increases.

Peace and Pringle [22] deduced that the deficiency line breadth, W, depends upon the amount of secondary extinction present rather than being proportional to the mosaic spread. Their expression for the line breadth is

$$W = \int_{-\infty}^{+\infty} (1 - \exp\left[-2G'(u)\,x\sec\theta\right]\,du \qquad (5)$$

The value of W/ζ can then be plotted against $Q' \times \sec\theta/\zeta$ as shown in figure 6. Among other things, this curve shows that the contrast of unresolved lines or the breadth of resolved lines increases very slowly with Q' in the case where a large amount of secondary extinction is present. By resolved and unresolved are meant the angular structure of the deficiency conic being observed or not observed [22].

The observation of the angular structure depends on ζ, the crystal to film distance, Z, and the source size. Under the usual experimental conditions for transmission Kossel photography, the crystal to film distance is about 10 cm, and the x-ray source size is about a 3 to 30 μm diameter hemisphere. For a value of ζ of 1 minute of arc, the angular structure width is 30 μm at a 10 cm distance. However, blurring due to multiple reflections also occurs causing a resolution decrease. Furthermore, the great majority of deficiency conics observed have their angular structure unresolved. For the case of unresolved deficiency conics the contrast, σ, in the presence of a background due to continuum radiation has been given as [22]:

$$\sigma = \frac{W}{s[1 + (K)\exp{(\mu x - \bar{\mu}x)}]} \qquad (6)$$

The contrast is thus a sensitive function of the crystal thickness, x, the operating voltage used to produce the x rays (through $\bar{\mu}$), the x-ray source size, s, the mosaic spread, the amount and distribution of both primary and secondary extinction, and finally of the film response and exposure used. While some conclusions on proper values of x and operating voltage in order to maximize σ can be drawn [23], values of "g" are not usually known for the crystal of interest. Therefore, measurements of the contrast of deficiency conics may not give unambiguous information concerning the crystal.

6

It is now necessary to consider the intensity to be expected for diffraction conics found on a transmission Kossel pattern, i.e., from planes where $\Phi > \theta$. Again the crystal is assumed to have a finite mosaic spread. Recalling when secondary extinction is dominant that $\mu' = \mu + gQ'$, the integrated intensity, P, for the transmitted diffraction conics is given by James for the case of $\Phi = 90°$ as [17]:

$$P = (Q'x \sec\theta)(\exp-[(\mu+gQ')x \sec\theta]) \quad (7)$$

For cases where Φ is not 90°, the relation for P is of the form of eq (7) except that extra geometrical factors must be included [24]. In any case, for a given Q' and θ, departure of Φ from 90° lowers the value of P. Equation (7) is valid for a single reflection; however, diffraction conics are usually composed of multiple reflections overlapping one another due to the previously mentioned cone vertex displacement. Peace and Pringle were able to deduce, by a statistical argument, the intensity issuing from a given point in the range of multiple reflections. The expression depends upon the same variables as eq (7) [22]. From this they were able to show that the total spread, S_T, of the emergent beam including the direct ray is not less than:

$$S_T = \frac{x \sin \theta}{\sin \Phi \sin (\Phi - \theta)} \quad (\Phi > \theta) \quad (8)$$

If this result is coupled with Lonsdale's relation for the separation of black and white conics in transmission, the condition for black and white overlap can be found [19]. Overlap will cause intensity and contrast cancellation. This in turn will make meaningful measurements involving the lines difficult if not impossible to obtain. Overlap occurs if the inequality of eq (9) is fulfilled.

$$\frac{\sin \theta}{2 \sin \Phi \sin (\Phi - \theta)} > \frac{\sin 2\theta}{\sin^2 \Phi - \sin^2 \theta} \quad (\Phi > \theta)$$

$$(9)$$

Diffraction conics observed on a back reflection pattern from a mosaic crystal are entirely analogous to those produced in transmission. The value of P_B is different, however [17].

$$P_B = \frac{Q'}{2(\mu + gQ')} \quad (10)$$

Equation (8) is also still applicable so that the lateral line spread can be calculated.

Consider now the mosaic crystal in which the domains are of random orientation. Lonsdale states that all secondary extinction effects will be smeared out in such a case [19]. This is tantamount to setting g equal to zero in the foregoing discussion; Q' may also increase to Q. This will lead to no deficiency conic contrast and an increased background absorption in transmission. Diffraction conics may appear in transmission and in back reflection since their integrated intensity is increased by setting g equal to zero. It might be parenthetically stated that this condition is apparently difficult to obtain since an iron foil broken in torsion gave deficiency conic contrast from a point about 10 μm from the fracture surface.

Perfect crystal regions can now be considered. Primary extinction is operable but secondary extinction is negligible. This means that the attenuation coefficient, τ, is far more important than μ. Typically, the primary beam intensity loss is greater than 90 percent after only two or three micrometers depth within the crystal. Thus, deficiency conic contrast exists for thicknesses greater than this. The continuous background still appears as the primary beam intensity attenuation is still $\exp \bar{\mu}x$ away from Bragg angles. However, the line is extremely sharp, ranging from far less than one second to perhaps one minute of arc for a perfect crystal; the higher the planar index, the less the line breadth [17]. In this angular range, essentially total reflection of the primary beam occurs. Hence, one would expect very high deficiency conic contrast. Unfortunately, such contrast is usually not obtained.

The reasons for this lack of contrast may be severalfold. First, the source size, s, must be as small as practicable in order to prevent blurring of the deficiency conics and direct contrast loss [19,22]. Second, graininess of the film may obliterate the line; this may also cause the line to appear broadened by truncating the peak [24]. Therefore, the finest grained film possible must be employed when perfect crystals are to be investigated. Finally, if the crystal is too thick, $\exp(\bar{\mu}x)$ lightens the background and causes contrast loss.

One other comment on contrast is germane: James indicates that the intensity drop-off within the cones should be proportional to $1/Z^2$ where Z is the source-to-film distance. Thus, for equal exposures, the greater Z is, the better the contrast for diffraction conics [17]. This is not true for deficiency

conics in general; their contrast is relatively independent of Z and may in fact become worse as Z increases [16]. The reason is that the intensity defect of the conic is fixed by the crystal perfection. The lightened background resulting from increasing Z may cause less white line contrast.

Having considered the formation and contrast of the lines on the pattern, it is necessary to explore the means for indexing patterns, determining lattice spacings and orientations, and to consider the effect of lattice imperfections.

B. Pattern Projection

The pattern which would be observed on a spherical film surrounding the sample consists of circles, the size and position of each of which depends upon Φ, θ, and the angle between a reference diameter on the sphere and the cone axis [19]. However, it is not feasible to use spherical film, and it is almost universal practice to use a flat film placed normal to the direction of excitation of the x-ray source. Using the perpendicular source to film distance, Z, as a radius, a sphere can be constructed. The film is tangent to this sphere at a point along the normal to the plane containing the source and the film plane. The line joining this point and the source of x rays will be called the projection axis; the point of intersection with the film is in fact the geometric pattern center. Although it is also referred to as the "film center," the point does not lie at the geometric center of the sheet of film in general.

The pattern observed on such a film is a gnomonic projection. The projection of any circle from the sphere onto the film plane is a conic section. Figure 7 suggests the process involved. The gnomonic projection means the angle χ which is equivalent to arc nD on the sphere is given by $\chi = n'D/DC$ on flat film. Lonsdale suggested the use of the stereographic projection to represent the expected pattern. In this case, circles on the sphere project as circles on the projection having angular radii, $(90°-\theta)$. However, the projection of the center of the circle from the sphere is not the center of the projected circle; thus, lines which are parallel on the sphere are not parallel in the stereographic projection [19].

To plot the projection requires that one know λ and however many lattice parameters there are. Then $(90° - \theta)$ is obtained as $\cos^{-1}(\lambda/2d)$. It should be mentioned that no plane for which $d \leqslant 0.5\lambda$ will give

rise to an observable conic. Furthermore, systematic conic absences must be taken into account. The next step is to plot the poles of expected conics with respect to the arbitrarily chosen pole. In the cubic system, these are always in the same place; for systems of lower symmetry, polar positions must be calculated for each case. Three $(90° - \theta)$ positions are plotted using the pole as center; then a circle is constructed through these points. This is the stereographic projection of a single plane for a single wavelength. An example is shown in figure 8a for Goss oriented Fe-3 Si. The corresponding Kossel pattern is shown in figure 8b.

The preparation of such projections by hand is tedious, time consuming, and subject to large errors — especially when the projection contains many conics. This difficulty has been overcome by Frazer and Arrhenius who have programmed a digital computer equipped with an X-Y plotter to prepare stereographic projections for any set of lattice spacings and wavelengths [25]. When a stereographic projection is available, indexing can be carried out directly by comparison with the film; the gnomonic and stereographic projections are quite similar over the range of angles normally recorded on the film.

C. Contrast in the Kossel Pattern

A comparison of the back-reflection and transmission modes indicated that for the Fe-3 Si study, the transmission mode was the more suitable. The reasons for this choice were: (1) Actual commercial laminates could be examined throughout the entire thickness, (2) Surface effects would not interfere with the analysis (back reflection methods sample regions only a few micrometers deep at the surface), (3) Deficiency conics are sharper than reflection conics, and (4) Contrast in transmission can often be made superior to that in back reflection by a careful choice of experimental conditions.

This contrast optimization has been studied in detail [23]. Deficiency conics are most prevalent in a transmission pattern. However, experimentally it has been observed on Kossel photographs that deficiency conics are often of weak contrast and occasionally even absent [19,26,27,28]. This has led several workers to consider the question of contrast optimization particularly with respect to the sample thickness.

8

Lonsdale was the first to study this problem and presented data for "optimum thickness" values in NaCl and diamond [19]. Later in a somewhat more general treatment Peace and Pringle [22] were led to an optimum sample attenuation corresponding to $\mu x = 1$. Subsequently, Hanneman, et al. proposed on an empirical basis that μx of five was an optimum value [29]. More recently, Potts stated that the contrast was relatively independent of the sample thickness [30]. All of these workers appear to have adopted the same definition of contrast. However, none of these workers investigated the effect of the operating voltage on the contrast. Equation (6) can be used to estimate the thickness-operating voltage relationship [23].

In Kossel transmission work, the radiation used is generally chosen on the basis of crystallographic considerations. For example, a particular wavelength which yields sensitive intersections for precise lattice spacing measurements may be chosen. This fixes the value of the linear absorption coefficient. Furthermore, the values of Q' and ζ are also predetermined. The value of "s" is fixed by the capabilities of the electron probe forming column. Thus, the only variables left with respect to which contrast may be adjusted are the sample thickness and the operating voltage. The operating voltage enters since $\bar{\mu}$ is a sensitive function of the continuum distribution which is manifestly a function of operating voltage. These considerations suggest that there may be a thickness at a given voltage which will yield a maximum contrast or a voltage at a given thickness which will do likewise.

Consider the denominator of eq (6) which needs to be minimized in order to increase contrast. If $\bar{\mu}x > \mu x$, then σ can be raised by merely raising the thickness or $\bar{\mu}$. However, the total intensity, I, reaching the film is given by $I = I_0 l^{-\bar{\mu}x}$. Therefore, if $\bar{\mu}x$ is increased much beyond 3, there will be little blackening of the film with time, i.e., exposure times become prohibitively long. In fact, one would tend to prefer $\bar{\mu}x \simeq 1$ in order to maximize any diffraction conics intercepted and to reduce the exposure time. It would seem, therefore, that values of $\bar{\mu}x = 1 > \mu x$ would almost always yield high contrast patterns. Unfortunately, the nature of the numerator of eq (6) precludes this simple solution.

Peace and Pringle have plotted (W/ζ) versus $(Q'x/\zeta)$; this plot is reproduced as figure 6. At values of $(Q'x/\zeta)$ greater than six, increasing the thickness has little effect on the values of W and hence upon the contrast. However, if x is too low, the value of $(Q'x/\zeta)$ may drop below six, especially for high index planes for which Q' may have a small value [17]. This will make the contrast a critical function of x and may well cause the loss of some high index lines. Therefore, since $(Q'x/\zeta)$ is generally unknown, it is necessary to increase x to insure that the region in which $6 > (Q'x/\zeta)$ is avoided for all lines to be recorded on the pattern. If this is done a pattern of nearly uniform contrast can be obtained owing to the nature of the function in figure 6.

The next step in the evaluation of the situation is to estimate values of "$\bar{\mu}$". Let $\bar{\mu}$ be defined as $b\mu$ where "b" is a factor to be determined. The factor "b" depends upon the short wavelength limit of the continuum, λ_C, the emitted intensity as a function of wavelength, $I_0(\lambda)$, the thickness x, the long wavelength limit, λ_f, of the spectrum, and the transmission of the sample as a function of wavelength. $\exp - [\widetilde{\mu}(\lambda)x]$.

An approximate relation giving the value of "b" can be obtained for incident electrons of given energy by using Kramers' approximation to the shape of the continuum band from a thick target [31] coupled with the function $[\widetilde{\mu}(\lambda)]$ which is tabulated [32].

It is found that "b" increases with decreasing thickness at a given operating voltage and also that "b" increases with decreasing operating voltage at a given thickness [23].

Three considerations are important in choosing a suitable thickness-operating voltage relationship. When the overvoltage ratio (E/E_0), denoted by "U", is decreased below two, characteristic peak to background ratios decrease rapidly as does the absolute spectral intensity. Furthermore, it should be recalled that the thickness chosen should yield a $Q'x/\zeta$ value greater than six. Opposing this is the fact that a $(\bar{\mu}x)$ value greater than three gives prohibitively long exposure times coupled with an increased K value in eq (6). It therefore appears that for most cases, a choice of $1.5 \leqslant \mu x \leqslant 2.5$ combined with $2.5 \leqslant U \leqslant 3.0$ will yield transmission Kossel or pseudo-Kossel photographs having nearly optimum contrast characteristics. Such a choice reduces the need for extremely thin, hard-to-prepare samples, yet gives a high enough overvoltage ratio to produce enough x-ray intensity for good photographic characteristics. Furthermore, such thickness values tend to help the value of $(Q'x/\zeta)$ rise above six [23].

Thus, the thickness required can be chosen and specimen preparation carried out accordingly. While a transmission pattern is representative of the entire specimen thickness used, it is desirable to carry out specimen preparation so that the inherent crystal perfection is not disturbed. It is possible to do this for Fe-3 Si by electropolishing to the final surface finish and thickness desired. The appropriate electropolishing solution is 5 percent $HClO_3$ in CH_3COOH run at 30 v, 3 amp/decimeter (temp. < 24 °C). A perfect metallographic finish is not really required for good transmission Kossel work.

In order to take full advantage of the properly prepared specimen for obtaining good contrast, the exposure time must be correct. According to Lonsdale, the exposure time of a Kossel photograph has an optimum value [19]. Depending upon the experimental conditions, the exposure time may vary from a few seconds to several hours [23,28]. Therefore, it is necessary to be able to estimate closely the exposure time.

Yakowitz and Vieth obtained semiempirical relations for the exposure time which are valid to about ±10 or 15 percent [34]. For the case of the film being in vacuum and a pseudo-Kossel experiment, they obtained for a transmission pattern as shown in figure 8.

$$t_E = \frac{2.7 \times 10^{-15} E_0 Z^2 (1-r) (\sec^2 \eta')}{n_0 i_s} \cdot$$

$$\{\exp (2/3) [\bar{\mu}_f x_f + \bar{\mu}_s x_s]\} \qquad (11)$$

Equation (11) takes into account the number of photons produced per incident electron, the operating voltage (through n_0) and the fact that the exposure is greatest at the central portion of the film and least at the edges. The latter is the result of a combination of two effects, the first of which is an increasing absorption path within the sample with increasing emergence angle. The other effect is geometrical in that a unit of solid angle subtends a larger area on the film at the edge than at the center.

The quantity E_0 is that exposure density yielding the maximum contrast between the Kossel conics and the background blackening for a given film at a given distance, Z. It must be determined empirically. Once this is done, it is to be expected that E_0 will be essentially constant for a given film type independent of other camera parameters [34]. The E_0 value represents a compromise between the exposure at the edge and central portions of the film.

Based on the previous discussion, it is clear that, by a careful choice of experimental conditions, transmission Kossel patterns of Fe-3 Si having good contrast can be prepared. The sensitivity of the contrast to experimental conditions implies that using contrast measurements may not be physically meaningful.

Certain authors have postulated that changes in atomic position associated with changes in the physical state of a crystal could be traced by consecutive measurements of intensity changes (sic) in a critical set of deficiency conics [25]. However, the contrast of a transmission Kossel pattern is a critical function of the x-ray source size, crystal thickness and mosaic spread, extinction characteristics of the crystal, operating voltage, exposure time, development technique, and the exciting wavelength spectrum. The overall deficiency of intensity is strongly dependent on the crystal perfection which is apt to vary with temperature and with any small change in strain state; less strong is the dependence on atom position changes. In fact, according to figure 6 and eq (6), in some cases, the apparent contrast for a given plane form can vary by a factor of two for a relatively small change in crystal perfection. However, a similar change in a thicker sample of the same crystal may lead to a contrast difference so small as to be nearly undetectable (plateau region of fig. 6). For these reasons, measurements of the contrast of deficiency conics are probably not useful as *quantitative* indicators of the physical state of the specimen crystal.

IV. Measurement of Lattice Strains

We are interested in internal strains on a microscopic scale. For the measurement of internal strains, it is customary to use the quantity $\Delta d/d$ where d_{hkl} is the interplanar spacing for a crystallographic plane having Miller indexes hkl. Once these lattice strains have been determined experimentally, elastic theory can be applied in order to obtain the complete strain picture including principal strains, principal stresses and their respective axes, stored elastic energy, shear stored elastic energy and maximum shear strain in any plane.

The Kossel method gives a pattern on which all planes of a multiplicity set are separated, i.e., if hkl

appears, so does $hk\bar{l}$, $\bar{h}k\bar{l}$, etc. This multiplicity separation occurs for all crystallographic lattices including cubic. The multiplicity separation provides two unique advantages for the Kossel method:

1. Anisotropic strains, whatever their source, can be unequivocally located and evaluated;

2. Having separate lattice strain values for each plane removes the necessity for complex "strain effect on an x-ray line" averaging as is required in the Warren-Averbach [35] x-ray strain analysis treatment. (Unfolding is required in other experimental x-ray analysis — of cubic materials because all planes of a multiplicity set appear as one peak — a consequence of Bragg's law and the instrumentation.)

Since all other strain information is inferred from the individual $\Delta d/d$ values these must be as accurate as possible. Therefore, measurement methods for the d values must be evaluated in terms of applicability and sources of error.

Four basic methods for determining lattice spacing data by means of the transmission Kossel technique have been described [36,29,37,38,39]:

1. The tangency method [36] requires that two conics on the Kossel pattern be nearly tangent to one another. In the cubic system, one can then directly calculate the lattice parameter, a, since the angles between any two crystallographic poles are always known. The disadvantages are that: (a) Only a lattice parameter is measured and then using only two of the available planes, (b) The sensitivity of the method depends directly on Bragg's law — the higher the θ values of the conics, the better the sensitivity. Thus, obtaining high sensitivity in any specific case is a matter of chance. (c) The method cannot be generalized to measuring individual d values. For these reasons, the tangency method was discarded.

2. The lens method [29,37] takes its name from the shape of the figure resulting when two conics on the film overlap. The pertinent relations for a lens in terms of the lattice parameter for a cubic material are shown in figure 9. This method can give very precise lattice parameters, but it has several disadvantages for strain measurements. Among these are (a) Special orientations of lens figures are required to eliminate gnomonic projection distortion errors, (b) Only lattice parameters, not d spacings are measured directly, (c) Not one but two lenses of a suitable type are required on the same pattern in order to eliminate uncertainties due to errors in the source to film distance, Z. Getting two suitable lenses on one

pattern is often difficult. The lens method was discarded for the Fe-3 Si problem.

3. The intersection method requires three or more conics to nearly intersect in a point. There are two types of intersections, invariant and accidental. Invariant intersections [19] are a function only of crystal symmetry and as the name implies, always occur. An example is the (220), (211), (121) intersection on figure 8. Invariant intersections are useless for strain measurements. Accidental intersections can be made to yield lattice parameter data [16,38]. But the existence, motion and sensitivity of an accidental intersection cannot be predicted. The intersection method was therefore discarded.

4. The fourth method — the Regressive Analysis Conic Equation (RACE) method [39] — yields d_{hkl} measurements directly, can be analyzed for uncertainties in a rigorous way and as a by-product yields orientation information. This method was adopted for the Fe-3 Si study.

The RACE method can be summarized as follows:

An orthogonal X-Y-Z coordinate system is set up where Z is in the direction from the x-ray source to the film. The value of Z represents the x-ray source-to-film distance. The center of the pattern is the X-Y plane origin, X_0Y_0 (see fig. 10). The equation of any conic on the Kossel pattern is [39]

$$q_1X + q_2Y + q_3Z = (X^2 + Y^2 + Z^2)^{1/2}\sin\theta \qquad (12)$$

Here q_1, q_2, and q_3 are the direction cosines of the plane (hkl) taken with respect to the X-Y-Z coordinate system. Define:

$$U \equiv q_1\csc\theta$$
$$V \equiv q_2\csc\theta$$
$$W \equiv q_3\csc\theta$$
$$M \equiv (X^2 + Y^2 + Z^2)^{1/2}$$

Then eq (12) becomes:

$$UX + VY + WZ = M \qquad (13)$$

In terms of the definitions above

$$q_i = \frac{U, V, W}{(U^2 + V^2 + W^2)^{1/2}} \qquad (14)$$

$$\cos(90 - \theta) = \sin\theta = \frac{q_1}{U} = \frac{q_2}{V} = \frac{q_3}{W} \qquad (15)$$

and

$$q_1^2 + q_2^2 + q_3^2 = 1.$$

Since $\sin\theta = \lambda/2d$, we get

$$d = 0.5\lambda\,(U^2 + V^2 + W^2)^{1/2} \qquad (16)$$

In principle, we could obtain the d values for all conics on the film by measuring the X-Y coordinates of only three points on each conic. In practice, we measure several points on each conic and use regressive analysis [39].

The values of U, V and W can be obtained by the principle of least squares in which case U, V and W are obtained by minimizing the sum

$$S^* = \Sigma(M_i - X_iU - Y_iV - W_iZ)^2 \qquad (17)$$

This process of minimization leads to a system of three equations having three unknowns. The solution of this system, called the normal equations, will be, statistically, the best estimates of U, V and W.

In this case, the normal equations for U, V, W are:

$$\begin{bmatrix} [X^2] & [XY] & z[X] \\ [XY] & [Y^2] & Z[Y] \\ Z[X] & Z[Y] & nZ^2 \end{bmatrix} \begin{bmatrix} U \\ V \\ W \end{bmatrix} = \begin{bmatrix} [Xn] \\ [Yn] \\ Zn \end{bmatrix} \qquad (18)$$

where $[X]$ means $\sum_i^n X_i$, etc., n is the number of coordinate measurements for the conic. Then:

$$\begin{bmatrix} U \\ V \\ W \end{bmatrix} = \begin{bmatrix} [Xn] \\ [Yn] \\ Zn \end{bmatrix} \begin{bmatrix} \Gamma^{11} & \Gamma^{12} & \Gamma^{13} \\ \Gamma^{21} & \Gamma^{22} & \Gamma^{23} \\ \Gamma^{31} & \Gamma^{32} & \Gamma^{33} \end{bmatrix}$$

where $\Gamma^{11} - \Gamma^{33}$ represents the elements of the inverse of the first matrix in eq (18).

A. Error Evaluation

The minimum value of eq (17) is taken as an indication of the goodness of the fit of eq (16) to the d values. The standard error of the estimate is defined as

$$s_e = \left[\frac{\Sigma(M_i - X_iU - Y_iV - W_iZ)^2}{n-3} \right]^{1/2} \text{in Ref. [40].}$$
$$(19a)$$

The standard errors associated with the estimates of U, V and W are [40]:

$$\begin{aligned} S_U &= S_e\sqrt{\Gamma^{11}} \\ S_V &= S_e\sqrt{\Gamma^{22}} \\ S_W &= S_e\sqrt{\Gamma^{33}} \end{aligned} \qquad (19b)$$

In order to obtain the standard error for the d spacing, the computed values of U, V, and W are used to obtain d_1, d_2-d_n. Then the standard deviation for d is calculated in the usual way.

In practice, all of the foregoing computation is carried out by a digital computer. However, it is apparent that the statistical uncertainties are not the only source of uncertainty in the measurement of the d values. Other contributors to d value uncertainties are measurement errors in X, Y and Z, the effect of an erroneous estimation of the location of the pattern center, X_0Y_0, and the uncertainty in the wavelength, λ. This last has been exhaustively studied by Bearden [41] and is of no importance to our strain measurements which involve the ratio of d values. Thus, wavelength uncertainty has been disregarded in all of what follows.

There is apparently no direct analytical method for propagation of errors due to, say, just Z in eq (18) [42]. Therefore, values of $\Delta d/\Delta Z$ and $\Delta d/\Delta r$, r being the radial uncertainty in locating X_0Y_0 were approximated by empirical means. Furthermore, errors in lattice strains $\epsilon_d = \Delta d/d_{hkl}$ resulting from errors in Z were evaluated for Fe-3 Si.

The error evaluation was carried out by measuring all the conics on a pattern of Fe-3 Si. Some eleven sets of coordinate positions were found for each conic. The computer delivered the d values for the X_0Y_0 and Z values determined as accurately as possible. Then the Z value was altered in the computer program and the corresponding change in d recorded. The same was done for the X_0Y_0 position. Thus, values of $\Delta d/\Delta Z$ and $\Delta d/\Delta r$ could be found for each conic. As in most crystallographic studies, as θ increased, the magnitude of errors decreased.

The results are plotted in figure 11. Clearly, the higher the value of θ, the less the d error in the case of uncertainties in both Z and X_0Y_0. Note that for a given value of θ, $\Delta d/\Delta Z$ is always considerably larger than $\Delta d/\Delta r$. We are interested in the uncertainty in the strain values for our application. The effect of an error in Z was found by straining Fe-3 Si to a nominal value of 0.2 percent and repeating the computer calculations of the effect of a change in Z. (The unstrained d values were taken from the previous experiment.) The result is shown as figure 12.

12

In practice, the value of Z is typically 5 to 12 cm. The Z distance can be found to within 0.1 mm by means of a depth gage. It is possible to do even better than this by using the lens method [37] to obtain a lattice parameter which is independent of Z and then to back-calculate, Z. It thus appears that, even when using conics having a θ value of 20°, the lattice strain uncertainty can be reduced to 0.0007.

With a good comparator, the uncertainties in the individual X,Y measurements can be reduced to 10 to 20 micrometers. It is reasonable to assume that such errors will be randomly biased for a given conic. The effect of these errors is negligible compared to that of the Z distance.

The X_0Y_0 position is found by allowing the electron beam to strike the plate. This impresses a small spot at the geometric pattern center. If the plate is in air, i.e., an x-ray window is in place, the light from the filament serves the same purpose. The X_0Y_0 position can be found to within 0.1 to 0.2 mm in this way.

To summarize, we now have a method for obtaining the individual d values. Of equal importance, there is also a means for determining the reliability of these d values and of the lattice strain values derived from them.

V. Stress-Strain Analysis

The Fe-3 Si alloy is body centered cubic in the unstrained state. It will be demonstrated that virtually nothing can be gained by assuming that Fe-3 Si fails to remain cubic in the strained condition, therefore it is assumed that we will always be dealing with a cubic lattice.

In the cubic system, it is convenient to choose a point within the irradiated volume of the crystal as a reference [6]. For the cubic lattice, three mutually perpendicular axes corresponding to the crystallographic directions [100], [010], and [001] can be made to pass through the reference point. In this case, the components of the vector $\mathbf{H} = (hkl)$ are the direction numbers for the family of planes called H. In general, if j is a unit vector, the normal strain component in the j-direction is:

$$\epsilon_j = jTj'$$ (20)

where j' is the transpose of j and T is the strain tensor given by

$$T = \begin{pmatrix} \epsilon_{11} & 0.5\epsilon_{12} & 0.5\epsilon_{13} \\ 0.5\epsilon_{21} & \epsilon_{22} & 0.5\epsilon_{23} \\ 0.5\epsilon_{31} & 0.5\epsilon_{32} & \epsilon_{33} \end{pmatrix}$$ (21)

The ϵ_{ij}' are the Cauchy strain components.

Now, by analogy to eq (20), the relation between the components of the strain tensor in terms of the Miller indices of a plane and the lattice strain, s, associated with that plane is

$$|\mathbf{H}|^2 s = \mathbf{H}'T\mathbf{H}$$ (22)

where

$\mathbf{H}' = (hkl)$ is the row matrix of the Miller indices $h, k, l, \mathbf{H}$ is the column matrix of hkl, s is the lattice strain normal to the plane with Miller indices (hkl) and T is defined by eq (21).

Explicitly, Eq (22) after the matrix multiplication becomes:

$$(h^2 + k^2 + l^2)s_d = h^2\epsilon_{11} + k^2\epsilon_{22} + l^2\epsilon_{33} + kl\epsilon_{32} + lh\epsilon_{13} + hk\epsilon_{12}$$ (23)

In order to solve this equation for the six strain values, at least six independent measurements of s values are needed, e.g., the six sets of hkl numbers lead to a matrix of rank six. There is apparently no way to decide whether a particular set of (hkl) values is suitable other than constructing the matrix and testing to see that its determinant does not vanish [6].

With an appropriate set of (hkl) values a unique strain tensor can be computed. But, as with the determination of the d values by the RACE method, setting up the normal equations for the strain tensor will yield the best estimates of ϵ_{11}, ϵ_{22}, ϵ_{33}, ϵ_{13}, ϵ_{23}, ϵ_{12}. These equations are derived in a manner exactly analogous to those for the determination of U, V and W given by eq (18). Calling the best estimates $\langle\epsilon_{11}\rangle$ $\langle\epsilon_{22}\rangle$ ... $\langle\epsilon_{12}\rangle$, the six normal equations are [6]

$$\begin{pmatrix} [h^2S(h^2+k^2+l^2)] \\ [k^2S(h^2+k^2+l^2)] \\ [l^2S(h^2+k^2+l^2)] \\ [klS(h^2+k^2+l^2)] \\ [lhS(h^2+k^2+l^2)] \\ [hkS(h^2+k^2+l^2)] \end{pmatrix} = \begin{pmatrix} [h^4] & [h^2k^2] & [h^2l^2] & [h^2kl] & [h^3l] & [h^3k] \\ [h^2k^2] & [k^4] & [k^2l^2] & [k^3l] & [hk^2l] & [hk^3] \\ [k^2l^2] & [k^2l^2] & [l^4] & [kl^3] & [hl^3] & [hkl^2] \\ [k^2kl] & [k^3l] & [kl^3] & [k^2l^2] & [hkl^2] & [hk^2l] \\ [h^3l] & [hk^2l] & [hl^3] & [hkl^2] & [h^2l^2] & [h^2kl] \\ [h^3k] & [hk^3] & [hkl^2] & [hk^2l] & [h^2kl] & [h^2k^2] \end{pmatrix} \begin{pmatrix} \langle \epsilon_{11} \rangle \\ \langle \epsilon_{22} \rangle \\ \langle \epsilon_{33} \rangle \\ \langle \epsilon_{23} \rangle \\ \langle \epsilon_{31} \rangle \\ \langle \epsilon_{12} \rangle \end{pmatrix} \qquad (24)$$

where $[h^2k^2] = h_1k_1 + h_2k_2 + \ldots h_nk_n$, etc.

The solution of eq (24) for the Cauchy strains can be programmed for machine computation in a straightforward way. Thus, the best possible estimates of the Cauchy strains are obtained. Next, the principal strains can be obtained.

Elastic theory shows that there exists for all points in a deformed continuous material a set of three directions in space such that linear elements placed along these directions in the undeformed condition will be subject to strains which have maximum or minimum values with respect to strains of linear elements in all other directions [43]. These three maxima are called the principal strains $S_1 \geqslant S_2 \geqslant S_3$, and the directions on which they lie after deformation are called the principal strain axes. The principal strain axes are orthogonal to each other in both the undeformed and deformed state.

In order to obtain the principal strains and axes, the following relation [6] can be used:

$$\text{Det } (T - S_i I) = 0 \qquad (25)$$

where S_i corresponds to the three principal strains and I, the invariant of eq (25) has the components:

$$I_1 = S_1 + S_2 + S_3,$$

$$I_2 = S_2S_3 + S_1S_3 + S_1S_2,$$

$$I_3 = S_1S_2S_3$$

In explicit form, the determinant of eq (25) is written from its characteristic matrix as:

$$\begin{vmatrix} \langle \epsilon_{11} \rangle - S & 0.5\langle \epsilon_{12} \rangle & 0.5\langle \epsilon_{31} \rangle \\ 0.5\langle \epsilon_{12} \rangle & \langle \epsilon_{22} \rangle - S & 0.5\langle \epsilon_{23} \rangle \\ 0.5\langle \epsilon_{31} \rangle & 0.5\langle \epsilon_{23} \rangle & \langle \epsilon_{33} \rangle - S \end{vmatrix} = 0 \quad (26)$$

This determinant reduces to a cubic equation in S_i; the roots of which are the latent roots of eq (26) and which can be solved by standard cubic equation formulae [43]:

$$S^3 - S^2[\langle \epsilon_{11} \rangle + \langle \epsilon_{22} \rangle + \langle \epsilon_{33} \rangle] + S[\langle \epsilon_{22} \rangle \langle \epsilon_{33} \rangle + \langle \epsilon_{11} \rangle \langle \epsilon_{33} \rangle + \langle \epsilon_{11} \rangle \langle \epsilon_{22} \rangle - 0.25(\langle \epsilon_{12} \rangle^2 + \langle \epsilon_{23} \rangle^2 + \langle \epsilon_{32} \rangle^2)]$$
$$- \{\langle \epsilon_{11} \rangle \langle \epsilon_{22} \rangle \langle \epsilon_{33} \rangle - 0.25[\langle \epsilon_{11} \rangle \langle \epsilon_{23} \rangle^2 + \langle \epsilon_{22} \rangle \langle \epsilon_{31} \rangle^2 + \langle \epsilon_{33} \rangle \langle \epsilon_{12} \rangle^2] + 0.25[\langle \epsilon_{12} \rangle \langle \epsilon_{23} \rangle \langle \epsilon_{31} \rangle]\} = 0$$

$$(27)$$

Computer programs have been written which reduce lambda matrices of the type just discussed to their latent roots directly. All of the latent roots of eq (27) are real [43]. A positive principal strain value represents a tensile strain while a compressive strain results in a negative sign.

In practice, eq (27) is solved for its roots by machine computation. Thus, the principal strains $S_1 \geqslant S_2 \geqslant S_3$ are obtained. For the principal strain axes we make use of the relation [6]:

$$(T - S_i I)l = 0; \; i = 1, 2, 3 \qquad (28)$$

where l is the eigenvector giving the direction cosines of the principal axes. Explicitly:

$$\begin{pmatrix} \langle \epsilon_{11} \rangle - S_1 & 0.5\langle \epsilon_{12} \rangle & 0.5\langle \epsilon_{31} \rangle \\ 0.5\langle \epsilon_{12} \rangle & \langle \epsilon_{22} \rangle - S_1 & 0.5\langle \epsilon_{23} \rangle \\ 0.5\langle \epsilon_{31} \rangle & 0.5\langle \epsilon_{23} \rangle & \langle \epsilon_{33} \rangle - S_1 \end{pmatrix} \begin{pmatrix} l_{11} \\ l_{21} \\ l_{31} \end{pmatrix} = 0$$

$$(29a)$$

14

$$\begin{pmatrix} \langle \epsilon_{11} \rangle - S_2 & 0.5 \langle \epsilon_{12} \rangle & 0.5 \langle \epsilon_{31} \rangle \\ 0.5 \langle \epsilon_{12} \rangle & \langle \epsilon_{22} \rangle - S_2 & 0.5 \langle \epsilon_{23} \rangle \\ 0.5 \langle \epsilon_{31} \rangle & 0.5 \langle \epsilon_{23} \rangle & \langle \epsilon_{33} \rangle - S_2 \end{pmatrix} \begin{pmatrix} l_{12} \\ l_{22} \\ l_{32} \end{pmatrix} = 0 \tag{29b}$$

$$\begin{pmatrix} \langle \epsilon_{11} \rangle - S_3 & 0.5 \langle \epsilon_{12} \rangle & 0.5 \langle \epsilon_{31} \rangle \\ 0.5 \langle \epsilon_{12} \rangle & \langle \epsilon_{22} \rangle - S_3 & 0.5 \langle \epsilon_{23} \rangle \\ 0.5 \langle \epsilon_{31} \rangle & 0.5 \langle \epsilon_{23} \rangle & \langle \epsilon_{33} \rangle - S_3 \end{pmatrix} \begin{pmatrix} l_{13} \\ l_{23} \\ l_{33} \end{pmatrix} = 0 \tag{29c}$$

The eigenvalues of the l eigenvector determined from eqs (29) may be written as the orthogonal matrix:

$$\begin{pmatrix} l_{11} & l_{21} & l_{31} \\ l_{12} & l_{22} & l_{32} \\ l_{13} & l_{23} & l_{33} \end{pmatrix} = l$$

The row vectors in the l matrix determine the principal axes for the strains. Explicitly, l_{11}, l_{21}, l_{31}, are the direction cosines of the principal axis associated with principal strain, S_1 while l_{12}, l_{22}, l_{32} and l_{13}, l_{23}, l_{33} are the direction cosines of the principal axes associated with principal strains S_2 and S_3 respectively. By determining the direction numbers A, B, C and the l matrix row vectors, a nearly orthogonal set of crystallographic directions having small Miller indices is found which closely represents the principal axes [44]. Explicitly:

$$\begin{vmatrix} \dfrac{A_1}{l_{11}} = \dfrac{B_1}{l_{21}} = \dfrac{C_1}{l_{31}} \\ \dfrac{A_2}{l_{12}} = \dfrac{B_2}{l_{22}} = \dfrac{C_2}{l_{32}} \\ \dfrac{A_3}{l_{13}} = \dfrac{B_3}{l_{23}} = \dfrac{C_3}{l_{33}} \end{vmatrix} \rightarrow \begin{vmatrix} A_1 & B_1 & C_1 \\ A_2 & B_2 & C_2 \\ A_3 & B_3 & C_3 \end{vmatrix}$$

There is a uniqueness problem associated with the solutions of eqs (29). The Cauchy strains are determined by the statistical algorithm described before. Thus, they are the best estimates available. The principal strains are derived from these estimates. What happens in the solution of eqs (29) is that the nine equations never quite give "l" values that make the solution exactly equal to zero. Instead, a typical value if 0.0007. The set of l values yielding a solution to eqs (29) closest to zero is taken to be the best estimate of the "l" eigenvector. The computer tests all possible combinations of signed solutions to eqs (29). The result chosen meets the "closest to zero" criterion described. The range in the solutions for the eigenvalues of the

l eigenvector gives an idea as to the reliability of the location of the principal strain axes.

With the principal strains and their axes determined, we may turn our attention to the question of finding the maximum shear strain in any (hkl) plane. This quantity is of importance since it may be used to evaluate, quantitatively, the anisotropy of strain in each (hkl) plane of a family. Furthermore, the exact planes on which strain accommodation occurs may be identified from comparisons of the maximum shear strain values [44]. The derivation will be given in some detail since it does not appear elsewhere. The result in a nearly complete form was given by Slade et al. [44]. These authors outlined the method that they used but gave no details.

The principal strain axes will be taken to be the reference axes. Within the (hkl) plane of interest, there will be some direction where the shear strain attains its maximum magnitude. Let a unit vector in this direction be called $\tilde{k}$ and let a unit vector perpendicular to $\tilde{k}$ in the (hkl) plane be called j. Now $\tilde{k}$ and j are 3 unit column matrices whose transposes will be called k' and j' respectively. In the principal axis system (the principal frame), the strain tensor, T, reduces to the diagonal matrix [43]:

$$\begin{pmatrix} S_1 & 0 & 0 \\ 0 & S_2 & 0 \\ 0 & 0 & S_3 \end{pmatrix} = T \quad \text{(principal frame)} \tag{30}$$

The shear component associated with $\tilde{k}, j$ is [44]:

$$\epsilon_{kj} = 2k'Tj \tag{31}$$

The factor of 2 comes from the relationship between the Cauchy (engineering) and tensor notations for shear stress.

The problem involves finding (1) the magnitude of the maximum shear strain in the $\tilde{k}j$ plane along $\tilde{k}$ called $(\epsilon_{kj})_{\max}$, (2) the magnitude of the shear strain along j, i.e., perpendicular to the maximum

15

shear strain in the (hkl) plane and (3) to transform from the $\tilde{k}$, j, $(\tilde{k}Xj)$ frame back to the principal frame in the terms of the (hkl) values of interest. The final result gives the maximum shear strain in any (hkl) plane and the direction cosines of the $\tilde{k}$, j, $(\tilde{k}Xj)$ system in terms of the hkl values and the direction cosines of the already determined principal strain axes.

Now $\tilde{k}k' = jj' = 1$ and $\tilde{k}j' = jk' = 0$ since we are dealing with unit vectors. We will use the method of Lagrange multipliers to find the maximum value of $\epsilon_{\tilde{k}j}$. We have two constraints in that there can be shear strain in the $\tilde{k}$ and $(\tilde{k}xj)$ directions but not in the j direction. (This will be proved later.) Hence, we get using the Lagrange method:

$$\frac{\delta \epsilon_{\tilde{k}j}}{\delta j} + \alpha \frac{\delta(jj')}{\delta j} + \beta \frac{\delta(\tilde{k}'j)}{\delta j} = 0 \qquad (32)$$

where α and β are the two Lagrangian multipliers to be evaluated. Carrying out the indicated operations in eq (32) gives

$$k'T + \alpha j' + \beta k' = 0 \qquad (33)$$

Multiplying eq (33) by j yields

$$k'Tj + \alpha j'j + \beta k'j = 0$$

But $jj' = 1$; $k'j = 0$ so

$$\alpha = -k'Tj$$

Now multiplying eq (33) by k:

$$k'Tk + \alpha j'k + \beta \tilde{k}k' = 0$$

and

$$\beta = -k'T\tilde{k}$$

Hence:

$$k'T - j'(\tilde{k}'Tj) - k'(k'T\tilde{k}) = 0 \qquad (34)$$

Multiplying eq (34) by Tk:

$$k'T^2k - T^2\tilde{k}j'k'j - (k'T\tilde{k})^2 = 0$$

But $\tilde{k}j' = k'j$ so that:

$$k'T^2\tilde{k} - (k'Tj)^2 - (k'T\tilde{k})^2 = 0 \qquad (35)$$

But $(k'Tj) = 0.5\,\epsilon_{kj}$. Thus:

$$(\epsilon_{\tilde{k}j})_{max} = 2[k'T^2\tilde{k} - (k'T\tilde{k})^2]^{1/2} \qquad (36)$$

Evaluating the terms under the square root sign:

$$h'T^2\tilde{k} = (\tilde{k}_1\tilde{k}_2\tilde{k}_3) \begin{pmatrix} S_1^2 & 0 & 0 \\ 0 & S_2^2 & 0 \\ 0 & 0 & S_3^2 \end{pmatrix} \begin{pmatrix} \tilde{k}_1 \\ \tilde{k}_2 \\ \tilde{k}_3 \end{pmatrix}$$

$$k'T^2\tilde{k} = \tilde{k}_1^2 S_1^2 + \tilde{k}_2^2 S_2^2 + \tilde{k}_3^2 S_3^2$$

$$k'T\tilde{k} = (\tilde{k}_1\tilde{k}_2\tilde{k}_3) \begin{pmatrix} S_1 & 0 & 0 \\ 0 & S_2 & 0 \\ 0 & 0 & S_3 \end{pmatrix} \begin{pmatrix} \tilde{k}_1 \\ \tilde{k}_2 \\ \tilde{k}_3 \end{pmatrix}$$

$$k'T\tilde{k} = \tilde{k}_1^2 S_1 + \tilde{k}_2^2 S_2 + \tilde{k}_3^2 S_3$$

$$(k'T\tilde{k})^2 = \tilde{k}_1^4 S_1^2 + \tilde{k}_2^4 S_2^2 + \tilde{k}_3^4 S_3^2 + 2\tilde{k}_1^2\tilde{k}_2^2 S_1 S_2 + 2\tilde{k}_1^2\tilde{k}_3^2 S_1 S_3 + 2\tilde{k}_2^2\tilde{k}_3^2 S_2 S_3$$

Subtracting:

$$(\epsilon_{kj})_{max} = 2[(S_1 - S_2)^2 \tilde{k}_1^2\tilde{k}_2^2 + (S_2 - S_3)^2 \tilde{k}_2^2\tilde{k}_3^2 + (S_3 - S_1)^2 \tilde{k}_3^2\tilde{k}_1^2]^{1/2} \qquad (37)$$

This is the magnitude of the maximum shear strain in the $\tilde{k}j$ plane; the $\tilde{k}j$ plane lies in the (hkl) plane of interest.

Two things remain to be done: to show that there is indeed no shear strain in the j direction and to find $\tilde{k}$ in terms of the l eigenvalues and the hkl

16

values. Perhaps the most straightforward way to do the former is to consider the Cartesian coordinate system $\tilde{k}$, $(\tilde{k}xj)$[3], j. Let the strain acting along a resultant in the $\tilde{k}$, $(\tilde{k}xj)$ plane be ϵ_{ij} and the angle the resultant makes with the $\tilde{k}$ axis be θ. Then

$$\frac{\delta\epsilon_{ij}}{\delta\theta} = -\epsilon_{\tilde{k}j}\sin\theta + \epsilon_{(\tilde{k}xj)j}\cos\theta = 0$$

$$\tan\theta = \sin\theta/\cos\theta = \epsilon_{(\tilde{k}xj)j}/\epsilon_{\tilde{k}j}$$

$$\sin\theta = \frac{\epsilon_{(\tilde{k}xj)j}}{[\epsilon^2_{(\tilde{k}xj)j} + \epsilon^2_{kj}]^{1/2}}$$

$$\cos\theta = \frac{\epsilon_{\tilde{k}j}}{[\epsilon^2_{(\tilde{k}xj)j} + \epsilon^2_{kj}]^{1/2}}$$

Now let $\theta' = \theta + 90°$. In other words, we would have a resultant strain in the j direction.

$$\epsilon_{ij}(\theta') = \epsilon_{\tilde{k}j}\cos\theta' + \epsilon_{j(\tilde{k}xj)}\sin\theta'$$

$$\epsilon_{kj}(\theta') = \epsilon_{\tilde{k}j}\sin\theta + \epsilon_{j(\tilde{k}xj)}\cos\theta$$

$$\epsilon_{ij}(\theta') = -\epsilon_{\tilde{k}j}\frac{\epsilon_{j(\tilde{k}xj)}}{[\epsilon^2_{(\tilde{k}xj)j} + \epsilon^2_{kj}]} + \epsilon_{j(\tilde{k}xj)}\frac{\epsilon_{\tilde{k}j}}{[\epsilon^2_{(\tilde{k}xj)j} + \epsilon^2_{kj}]}$$

$$\epsilon_{ij}(\theta') = 0$$

Thus, in any (hkl) plane, the shear strain will be zero normal to some direction in the plane and the direction of maximum shear strain in the plane is normal to this direction.

Finally, we need $\tilde{k}$ in terms of (hkl) and the principal strain axes positions. The direction cosines of the hkl axes are given by:

$$h_n = \frac{h}{h^2 + k^2 + l^2}; \quad k_n = \frac{k}{h^2 + k^2 + l^2}; \quad l_n = \frac{l}{h^2 + k^2 + l^2}$$

The transformation required is then:

$$\tilde{k}_i = h_n k_n l_n \begin{pmatrix} l_{1i} \\ l_{2i} \\ l_{3i} \end{pmatrix} \quad (38)$$

Thus, the maximum shear strain in any (hkl) plane can be evaluated. In practice, the results given by eqs (37) and (38) are obtained by machine computation. With these results, the entire shear

[3] This notation, $(\tilde{k}xj)$, means the vector crossproduct of $\tilde{k}$ with j.

strain effect can be followed as a function of strain and/or position in an individual grain of a material.

The next step in the evaluation of the stress-strain configuration in the elastic region is the determination of the stresses in the cubic frame, and the principal stresses and their axes. In the elastic region, the generalized form of Hooke's law relates the stresses to the strains.

$$\sigma_{CUB} = CE \quad (39a)$$

which in explicit form for the cubic case is

$$\begin{pmatrix} \sigma_{11} \\ \sigma_{22} \\ \sigma_{33} \\ \sigma_{23} \\ \sigma_{31} \\ \sigma_{12} \end{pmatrix} = \begin{pmatrix} C_{11} & C_{12} & C_{12} & 0 & 0 & 0 \\ C_{12} & C_{11} & C_{12} & 0 & 0 & 0 \\ C_{12} & C_{12} & C_{11} & 0 & 0 & 0 \\ 0 & 0 & 0 & C_{44} & 0 & 0 \\ 0 & 0 & 0 & 0 & C_{44} & 0 \\ 0 & 0 & 0 & 0 & 0 & C_{44} \end{pmatrix} \begin{pmatrix} \langle\epsilon_{11}\rangle \\ \langle\epsilon_{22}\rangle \\ \langle\epsilon_{33}\rangle \\ \langle\epsilon_{23}\rangle \\ \langle\epsilon_{31}\rangle \\ \langle\epsilon_{12}\rangle \end{pmatrix} \quad (39b)$$

The C values are the elastic constants and the ϵ values are those determined using eq (24). Thus, the cubic frame stresses can be obtained. The principal stresses, $P_1 \geqslant P_2 \geqslant P_3$ are determined by solving for the latent roots of the stress-analogue of eq (26):

$$\begin{vmatrix} \sigma_{11} - P_i & \sigma_{12} & \sigma_{31} \\ \sigma_{12} & \sigma_{22} - P_i & \sigma_{23} \\ \sigma_{31} & \sigma_{23} & \sigma_{33} - P_i \end{vmatrix} = 0 \quad (40)$$

The solution gives P_1, P_2 and P_3. The principal stress axes can be found in a manner entirely analogous to that outlined for determining the principal strain axes. Again, tensile and compressive stresses are indicated by the sign of the P value.

The stresses with reference to any frame can be determined according to classical transformation techniques following an outline given by Slade et al. [44]. The transformation maxtrix can be deduced in terms of the direction cosines of the axes of the new frame and the results of eq (39). Thus, the stresses in any frame can be found by this transformation.

For example, suppose that the stresses are required with respect to the principal strain axes. In other words, what stress configuration is necessary to give the observed three principal strains? Following the treatment of Slade et al. [44], the required transformation matrix $T_{m\sigma}$, is given by:

17

$$T_{m\sigma}=\begin{vmatrix} l_{11}^2 & l_{21}^2 & l_{31}^2 & 2\,l_{21}l_{31} & 2\,l_{31}l_{11} & 2\,l_{11}l_{21} \\ l_{12}^2 & l_{22}^2 & l_{32}^2 & 2\,l_{22}l_{32} & 2\,l_{32}l_{12} & 2\,l_{12}l_{22} \\ l_{13}^2 & l_{23}^2 & l_{33}^2 & 2\,l_{23}l_{33} & 2\,l_{33}l_{13} & 2\,l_{13}l_{23} \\ l_{12}l_{13} & l_{22}l_{23} & l_{32}l_{33} & (l_{22}l_{33}+l_{32}l_{23}) & (l_{32}l_{13}+l_{12}l_{33}) & (l_{12}l_{23}+l_{22}l_{13}) \\ l_{13}l_{11} & l_{23}l_{21} & l_{33}l_{31} & (l_{23}l_{31}+l_{33}l_{21}) & (l_{33}l_{11}+l_{13}l_{31}) & (l_{13}l_{21}+l_{23}l_{11}) \\ l_{11}l_{12} & l_{21}l_{22} & l_{31}l_{32} & (l_{21}l_{32}+l_{31}l_{22}) & (l_{31}l_{12}+l_{11}l_{32}) & (l_{11}l_{22}+l_{21}l_{12}) \end{vmatrix} \tag{41}$$

The required result is:

$$\sigma_{PRIN}=T_{M\sigma}\sigma_{CUB} \tag{42}$$

where σ_{CUB} is obtained from eq (39). In this way, the stresses with respect to any frame can be found provided the axes of the frame can be written in explicit form.

The elastic energy stored in the crystal, W, is equivalent to the work done in straining the crystal [43]. Specifically:

$$W=\int\sigma'\delta\epsilon=\int\epsilon'C\delta\epsilon=\frac{1}{2}\,\epsilon'C\epsilon, \tag{43}$$

since $\epsilon'\epsilon=\epsilon^2$.

In explicit terms:

$$2W=(\epsilon_{11}\epsilon_{22}\epsilon_{33}\epsilon_{23}\epsilon_{31}\epsilon_{12})\begin{vmatrix} C_{11} & C_{12} & C_{12} & 0 & 0 & 0 \\ C_{12} & C_{11} & C_{12} & 0 & 0 & 0 \\ C_{12} & C_{12} & C_{11} & 0 & 0 & 0 \\ 0 & 0 & 0 & C_{44} & 0 & 0 \\ 0 & 0 & 0 & 0 & C_{44} & 0 \\ 0 & 0 & 0 & 0 & 0 & C_{44} \end{vmatrix}\begin{vmatrix} \epsilon_{11} \\ \epsilon_{22} \\ \epsilon_{33} \\ \epsilon_{23} \\ \epsilon_{31} \\ \epsilon_{12} \end{vmatrix} \tag{44a}$$

$$2W=\begin{vmatrix} C_{11}\epsilon_{11}+2C_{12}\epsilon_{22}\epsilon_{33} \\ C_{11}\epsilon_{22}+2C_{12}\epsilon_{11}\epsilon_{33} \\ C_{11}\epsilon_{33}+2C_{12}\epsilon_{11}\epsilon_{22} \\ C_{44}\epsilon_{23} \\ C_{44}\epsilon_{31} \\ C_{44}\epsilon_{12} \end{vmatrix}(\epsilon_{11}\epsilon_{22}\epsilon_{33}\epsilon_{23}\epsilon_{31}\epsilon_{12}) \tag{44b}$$

$$W=\frac{1}{2}C_{11}(\epsilon_{11}^2+\epsilon_{22}^2\epsilon_{33}^2)+C_{12}(\epsilon_{22}\epsilon_{33}+\epsilon_{11}\epsilon_{33}+\epsilon_{11}\epsilon_{22})+\frac{1}{2}C_{44}(\epsilon_{23}^2+\epsilon_{31}^2+\epsilon_{12}^2) \tag{44c}$$

The value of W calculated by this fashion takes no account of lattice point defects which result in random strains. Sharp Kossel lines indicate that random strains are small since such strains cause line broadening.

Finally, Slade et al. [44] have postulated that a purely geometrical measure of distortion of the irradiated crystal volume can be gotten from:

$$D=\frac{2}{11}\left[\frac{4I_1^2-11I_2-3I_3^{2/3}}{I_1^2-2I_2}\right] \tag{45}$$

where

$$\left.\begin{array}{l} I_1=S_1+S_2+S_3 \\ I_2=S_2S_3+S_3S_1+S_1S_2 \\ I_3=S_1S_2S_3 \end{array}\right\}\text{ Defined in eq (25)}$$

The value of D is called the distortion number and is independent of the frame. The distortion number is a measure of the anisotropy of deformation in that D is zero in the case of spherically symmetrical deformation while D is unity if the deformation is simple shear.

18

To sum up, the Kossel method yields lattice strains for each (hkl) plane of a family. From these can be calculated the Cauchy strains, the principal strains and their axes, the maximum shear strain in any (hkl) plane, the cubic stresses, the principal stresses and their axes, the total stored elastic energy and the distortion number. This information completely describes the stress-strain configuration of the crystal in the irradiated volume.

The reliability of this stress-strain analysis has been dealt with in only a cursory fashion. A few comments to the effect that the computed Cauchy strains would be more reliable if a great number of (hkl) planes were examined have been made [45]. An estimate of the uncertainty on the principal strains computed from the Cauchy strains has been made for a single strain condition in a tungsten crystal.

VI. Reliability Analysis

The standard error, s_d'' of the d values can be obtained as described previously. This error must be combined with the experimental error which comes primarily from uncertainties in the source-to-film distance, Z. A standard error on the d value from uncertainties in Z, can be obtained from the standard error on the Z distance, s_Z, and figure 6. Then since variances are additive:

$$s_d' \simeq \sqrt{(s_d'')^2 + (s_Z)^2} \qquad (46a)$$

Contributions from other errors such as the X, Y measurements and the X_0Y_0 position do not increase s_d' by more than about 10 percent. Hence, a good approximation is:

$$s_d \simeq 1.1 s_d' \simeq 1.1 \sqrt{(s_d'')^2 + (s_Z)^2} \qquad (46b)$$

Since the determination of the d values, and hence the S values, is based on repetitive measurements, the number of repetitions for a suitably narrow 95 percent confidence interval width is of interest. But, first we must decide what a "suitably narrow 95 percent confidence interval" is. While certain specialized techniques [29, 37] can give relative uncertainties in a d value of about 0.002 percent, a more usual value is 0.01 to 0.05 percent. We shall arbitrarily accept the 0.05 percent figure as

the maximum acceptable width of the 95 percent confidence interval for a d value to be used in the stress-strain analysis.

For Fe-3 Si, the {110} conics have a Bragg angle, θ, of about 30° when the diffracted wavelength, λ, is Fe-K$_{\alpha 1}$ ($\lambda = 1.936$Å). The value of s_Z for the {110} conics can be reduced to about 0.001. The value of s_e for the {110} conics was found to be 0.0016 (eleven determinations). Using eq (46), we get s_d equal to about 0.002; d is 2.024Å. In order to reduce the width of the 95 percent confidence interval to 0.05 percent, we need to make enough determinations to reduce the interval to 0.001Å. By going to a table of "t" values and applying the usual relation

$$W_{95\%} = \frac{(s_d)\,(t_{n-3})}{\sqrt{n}} = 0.001, \qquad (47)$$

where t_{n-3} is Student's t limited by 3 constraints (the U, V, W equations) and n the number of individual d measurements, we find n equal to 18. Therefore, even for a conic having θ equal to 30°, some 18 (X, Y) coordinate measurements are sufficient to reduce the uncertainty in d to about 0.05 percent. Other conics, with higher θ values will have smaller ranges of uncertainty. Thus, 18 coordinate measurements are sufficient for all conics in the Fe-3 Si case and in general for conics having $\theta \geqslant 30°$ to meet the $d \pm W_{95\%}$ criterion. The usual probable error often reported is $d \pm W_{50\%}$. For 18 determinations of the {110} conic d spacing. $W_{50\%} \simeq 0.0004$Å. Transferred to percentages $d_{110} \pm w_{50\%} = 0.02$ percent.

The error in the lattice strain, S_d, is arrived at using Gaussian error distribution.

$$\Delta S_d = \sqrt{(d_i \Delta d_f)^2 + (d_f \Delta d_i)^2}/d_i^2 \qquad (48)$$

Here $\Delta d_f = w_{f,\,95\%}$ and $\Delta d_i = w_{i,95\%}$. Now in the elastic or low strain region where the KISS method is valid, d_f will be nearly equal to d_i, and Δd_f will be nearly equal to Δd_i. So as a working approximation

$$\Delta S \simeq \sqrt{2}\Delta d_i/d_i \simeq \sqrt{2}\Delta d_f/d_f \qquad (49)$$

But as outlined above, $(\Delta d_f/d_f)_{max} = 0.05$ percent. Hence, the maximum width of 95 percent confidence interval is 0.07 percent. The probable error in this case will be 0.03 percent. It is worth repeating that

19

this is the worst case—that of a conic with a Bragg angle, θ, of 30°. For high θ conics, it is possible to reduce the value of $w_{95\%}$ for S_d to the neighborhood of ±0.015 percent.

The next step in the error analysis is to determine the uncertainties of the Cauchy strains. The Cauchy strains are computed by a least squares regressive analysis in a manner exactly analogous to the computation of the U, V, W and d values as outlined previously. By analogy to eq (19) we have for the case of the strains:

$$s_e = \Sigma\,[\,(h_i^2 + k_i^2 + l_i^2)\,S_{d_i} - h_i^2\langle\epsilon_{11}\rangle - k_1^2\langle\epsilon_{22}\rangle - l_i^2\langle\epsilon_{33}\rangle$$

$$-\,k_i l_i\,\langle\epsilon_{32}\rangle - l_i h_i\langle\epsilon_{13}\rangle - h_i k_i\langle\epsilon_{12}\rangle\,]^2/(n-6) \qquad (50)$$

Here n is the total number of (hkl) planes for which there have been obtained S_d values. Then by analogy

$$s'\langle\epsilon_{11}\rangle = s_e\,\sqrt{\Gamma^{11}} \qquad (51\text{A})$$

$$s'\langle\epsilon_{22}\rangle = s_e\,\sqrt{\Gamma^{22}}\ \text{ and so on to} \qquad (51\text{b})$$

$$s'\langle\epsilon_{12}\rangle = s_e\,\sqrt{\Gamma^{66}} \qquad (51\text{c})$$

where the Γ values come from the inversion of the second matrix of eq (24).

Thus, we have the standard error for each of the computed Cauchy strains. These values of $s'_{\langle\epsilon_{ij}\rangle}$ will decrease as the number of (hkl) planes, n, used to obtain the Cauchy strains increases since increase n reduces s_e in eq (50). For the Γ^{ii} values to decrease, a large spread in the Bragg angles of the (hkl) planes used is necessary. In other words, one must make an adequate sampling of all the planes [45]. As we have seen, there are large potential errors if low θ conics are used. On the other hand, line broadening is usually associated with conics having $\theta \geqslant 80°$ [46]. Therefore, a suitable range of (hkl) values is one yielding a range of $30° < \theta < 80°$. Variation of a few degrees at either end will probably not lead to serious problems.

The effect of lattice strain errors on computed $\langle\epsilon_{ij}\rangle$ values must be combined with the $s'_{\langle\epsilon_{ij}\rangle}$ values in order to obtain a final estimate of the uncertainties in the Cauchy strains. First, the effect of a systematic error in the lattice strain values may be considered. To observe the error propagation, a test case was run through the computer. The Cauchy strains and the $s'_{\langle\epsilon_{ij}\rangle}$ values were calcu-

lated from a published set of typical lattice strain data from a tungsten sample strained to about 0.2 percent [45]. Some 20 planes were used in the test. The range of θ was $40.2° \geqslant \theta \geqslant 65.8°$. Then the S values were varied by set amounts of $+0.0005$, -0.0002, -0.0005, -0.001. The values of $\langle\epsilon_{ij}\rangle$, $i \neq j$ did not change while the values of $\langle\epsilon_{ij}\rangle$ $i=j$ varied by exactly the amount of the systematic error. None of the $s_{\langle\epsilon_{ij}\rangle}$ values changed.

It is unlikely that a systematic error in the lattice strain values of significant magnitude will occur since the nature of the measurements and the computation of S tend to minimize this possibility. However, random errors of individual lattice strain values will almost certainly occur. The magnitude of these errors as a function of θ has already been discussed. In order to test the effect of the random errors, the following procedure was used: (For purposes of this test, a constant increment of $\Delta S_d = 0.0003$ representing an average value was used.) The computer was made to list tables of random digits; the sign and order of the ΔS_d values was determined by these random digits. Thus, from one table even digits meant a subtraction and vice-versa while another table determined the order of the (hkl) plane to which these signs were to be applied. Some four sets of random data suffering uncertainties of S_d were synthesized in this way. Next the $\langle\epsilon_{ij}\rangle$ and $s'_{\langle\epsilon_{ij}\rangle}$ values were computed for each of these four sets. The $s'_{\langle\epsilon_{ij}\rangle}$ did not vary significantly from their previous values. All of the $\langle\epsilon_{ij}\rangle$ values changed. The results are shown in table I.[4] As a test for randomness, all of the new $\langle\epsilon_{ij}\rangle$ were averaged. Agreement between this mean value and the original $\langle\epsilon_{ij}\rangle$ values was taken to indicate randomness. Table I shows that the agreement is very good except for $\langle\epsilon_{12}\rangle$. The range of $\langle\epsilon_{ij}\rangle$ values for the four cases and the standard error in $\langle\epsilon_{ij}\rangle$ was calculated. This final standard error s'_{RND}, and the $s'_{\langle\epsilon_{ij}\rangle}$ can be combined to give:

$$s\langle\epsilon_{ij}\rangle = \sqrt{(s'_{\langle\epsilon_{ij}\rangle})^2 + (s_{\text{RND}})^2}. \qquad (52)$$

Table I shows that $s_{\langle\epsilon_{ij}\rangle}$ is about $1.05\,s'_{\langle\epsilon_{ij}\rangle}$. Hence, the effect of uncertainties in S_d may be taken into account by asserting that

$$s_{\langle\epsilon_{ij}\rangle} \simeq 1.1\,s'_{\langle\epsilon_{ij}\rangle} \qquad (53)$$

Equation (53) thus represents a statement of the standard error of the calculated Cauchy strains

---

[4] All tables are at the end of this paper beginning on page 39.

which takes into account uncertainties from all contributing sources.

The width of the 95 percent confidence interval for the Cauchy strains is obtained from:

$$w_{\epsilon, 95\%} = \frac{t^{95\%}_{(n-6)} s_{\langle \epsilon_{ij} \rangle}}{\sqrt{n}} . \qquad (54)$$

In the case of table I, some twenty (hkl) planes were used. Hence,

$$w_{\epsilon, 95\%} = \frac{(2.145)}{\sqrt{20}} s_{\langle \epsilon_{ij} \rangle} = 0.48 s_{\langle \epsilon_{ij} \rangle} . \qquad (54b)$$

The probable error, $w_{\epsilon, 50\%}$, is $0.115\ s_{\langle \epsilon_{ij} \rangle}$. As a rule of thumb, for all of the work discussed here, the probable error will be about one-third of the 95 percent confidence interval width.

The effect of uncertainties in the Cauchy strains on the computed principal strains will now be considered. By randomly signing the $w_{\epsilon, 95\%}$ error on the Cauchy strains, six sets of principal strains were obtained from the data in table I. All random sets lay within the range of principal strains obtained when all six Cauchy strain uncertainties were either $+ W_{\epsilon, 95\%}$ or $- W_{\epsilon, 95\%}$. The mean of all six sets was equal to the principal strains computed from the original calculated Cauchy strains. Results are shown in table II.

Based on these results, it is reasonable to assert that a 95 percent confidence interval for the principal strains can be obtained by calculating three sets of principal strain values. First with the calculated $\langle \epsilon_{ij} \rangle$ values, then in turn with $\langle \epsilon_{ij} \rangle + W_{\epsilon, 95\%}$ and $\langle \epsilon_{ij} \rangle - W_{\epsilon, 95\%}$. The resultant range should be a close estimate of the width of the 95 percent confidence interval for each of the three principal strains.

For the case used as an example, table II shows that the 95 percent confidence interval is about ± 25 to 30 percent of the principal strain value for all three principal strains. These values appear to be typical for lightly strained Fe–3 Si as well as for the tungsten test case. There is no reason to believe that they will be much different for other materials. Hence, it is concluded that for lightly strained (elastic region or residual strains), the Kossel method, carefully applied, can generally give principal strain values having 95 percent confidence interval widths of ± 30 percent or probable errors of

about ± 10 percent relative to the computed principal strains.

With these results, the reliability of the stress calculations (eqs (39, 40)), can be obtained by substituting the principal strain limits into the appropriate relation. For our discussion, we will assume that the elastic constants are well known. In this way, the reliability of the entire stress-strain analysis is established.

As an overall generalization, all of the calculated results of the stress-strain analysis obtained by the Kossel method can be expected to have an approximate probable error of about ± 10 percent relative to the calculated value. It is difficult to see how this error can be reduced very much in the future in view of the stringent requirements for using many (hkl) planes having $30° < \theta < 80°$, and the difficulty in improving on the regressive analysis methods used to calculate the stress-strain parameters.

The magnitude of the uncertainty in the Kossel stress-strain analysis is about the same as that obtained using conventional x-ray stress-strain methods. However, other x-ray stress-strain measurements yield little more than an estimate of the residual stresses present in the irradiated volume.

The computed uncertainty is the primary reason that it is not presently advantageous to consider that the deformed material ceases to remain cubic. In reality, the material cannot remain cubic. But, it is impossible to say what form the material will take for a given deformation, nor whether that form is continuous throughout the entire body of deformed material. Under these conditions, any form capable of mathematical analysis is an approximation. The simplest form, cubic, is as reasonable to choose as any other. It is concluded that nothing is to be gained by using a lower symmetry for calculation of elastic stress-strain parameters than that present in the undeformed state.

VII. Equipment for the Study of Materials by the Kossel Method

In order to take the maximum advantage of the opportunities afforded by the use of the Kossel method, appropriate equipment is necessary. As with virtually all scientific equipment, this means that a maximum amount of accurate information is desired for a minimum of effort and expense. In the case of

21

the Kossel method, once the equipment is available the production of the required patterns becomes completely routine. Unfortunately, the choice and design of appropriate equipment was not obvious at the time this study was begun. However, the equipment finally adopted and used for the work described here meets all requirements for the rapid, meaningful preparation of Kossel patterns of both strained and unstrained materials. Since some of the concepts of the equipment were unique to Kossel studies at the time they were formulated, and since the hardware is still unique, both concepts and the resulting instrument will be described in some detail.

The first successful experimental demonstration of a divergent beam diffraction technique was made by Rutherford and Andrade in 1914. These workers used an external radium source of γ-rays and a cleaved rocksalt crystal as the target. From the photographically recorded diffraction pattern, they were able to determine the monochromatic radiation components of the source [47]. Several other workers devised successful methods of preparing divergent beam patterns in the years between 1920 and 1950 [48-52].

In addition to being cumbersome and complex, all divergent beam devices prior to 1951 suffered the handicap of relatively large sources of x radiation. This led to several problems: a large primary source causes the Kossel lines to be broadened and impairs the inherent precision of the method; in addition, exposure times are prohibitively long (24 h in some cases) and photographic contrast is poor. Furthermore, large single crystals are required to accommodate the large x-ray sources.

These problems were first removed by the use of the electron probe microanalyzer which provides a micrometer sized source of x rays, as well as an optical microscope for viewing the area undergoing irradiation. Power densities five to ten times greater than those obtainable with earlier equipment are available. The value of the electron probe microanalyzer as a source for Kossel patterns was recognized by its inventor, Castaing, as soon as his first instrument was completed. He presented Kossel patterns in his thesis which clearly demonstrated the superior characteristics of the microprobe in this area [53].

All present day Kossel instrumentation utilizes a focused electron beam to excite the required microsource of x radiation. While commercial Kossel camera attachments for electron probe microanalyzers represent the most readily available instrumentation, investigators have successfully prepared Kossel cameras for use in point-projection x-ray microscopes and in electron microscopes, possibly since all of these instruments provide convenient electron optics.

Experience gained from attempting to use an electron probe microanalyzer as the electron optical column and a small simple Kossel camera, indicated that the electron optical requirements for the vast majority of Kossel line based research are less stringent than those for electron probe microanalysis and electron or x-ray microscopy. A single electromagnetic lens combined with an inexpensive flat grid electron gun makes an entirely satisfactory electron column. A relatively inexpensive power supply can be used since gun voltage stability requirements are less demanding than for electron microanalysis or microscopy. The same is true for the single lens power supply needed. To complete the system (exclusive of the Kossel camera), a small vacuum system, suitable light optics, and a current meter whose range is 10 to 1000 nanoamperes are required. Finally, a modular design can be modified at will to incorporate improvements. Hence, the decision was made to design and build a separate Kossel Pattern Generator (KPG) suitable for operation in the transmission mode [54, 55].

An air camera offers the advantage of allowing multiple exposures without disturbing the vacuum conditions or the orientation of the specimen. With respect to increased exposure times involved with air path cameras, the softest radiation used to date in quantitative transmission Kossel work has been V $K\alpha$ at 2.5 Å. The decrease in incident intensity of V $K\alpha$ upon a film 10 cm distant in air is less than 30 percent. In practical terms this results in an exposure time increase of about 10 min. Most work has been done using radiation somewhat harder than this. For example, for Cu $K\alpha$ at 1.54 Å, a 10 cm air path reduces the intensity by less than 10 percent. Therefore, reduction in exposure time gained by using a vacuum path is usually on the order of 10-20 percent or, in terms of actual decrease in exposure time, about 2 to 4 min. The very close {110} $K\alpha_1$-$K\alpha_2$ doublet in Fe-3 wt.% Si is quite easily resolved in an 11 cm air path camera. This indicates that air scattering of the x rays is probably not a serious problem.

The entire system was designed so that it could be dismantled and repaired with a minimum of incon-

venience while still satisfying all of the design concepts listed in reference [54]. The camera is a separate module removable from the electron beam column by means of three bolts.

The stage allows translation of the specimen amounting to one-half inch in orthogonal directions. Each motion is spring loaded to minimize backlash and each is connected by means of vacuum shaft seals to a micrometer shaft. Thus, the coordinates of a given point on the specimen can be found and recorded so that the point can be found again later. The vertical motion of the stage which makes it possible to focus the optical microscope is controlled by a worm and wheel arrangement. The wheel has 230 teeth and advances a four lead thread five-eighths inch per revolution. This gives a rapid vertical motion but retains enough sensitivity to focus easily in the light microscope.

A two-axis goniometer was mounted on this mechanical stage and each tilt motion can be controlled from outside the vacuum system; an indicating dial is used to index the angle of each axis. The tilt is controlled by a worm and a worm-gear; each tilt mechanism is spring loaded to minimize the effects of backlash. A small worm-gear was used in view of space limitations. This limited the number of teeth and hence the angular sensitivity of the goniometer to a minimum readable motion of about 0.2°. The goniometer may be tilted $\pm 12°$ about each axis. At this angle the edge of the stage strikes the light optical objective lens.

The essential part of the goniometer design as well as of the vertical specimen motion is the linkage connecting the external control device to the actual moving part. Each linkage can move through an angle up to 15°, traverse a distance of 0.70 in, and rotate freely. This was accomplished by attaching small universal joints on the ends of standard sliding tubular linkage. In order to prevent galling of the sliding mechanism in vacuum, each part was lubricated with a suspension of MoS_2 in diffusion pump oil. These linkage components are shown in place in figure 13.

Finding and marking the pattern center is carried out as follows: A small aperture at the specimen plane is brought to the coordinate point of the beam. Light from the hot filament is allowed to strike the film; the high voltage is switched off during this operation. A small spot is impressed at the pattern center by this means.

The brass specimen holder accommodates a three-fourths inch diameter sample, sandwiched between brass disks.

A source foil for pseudo-Kossel studies could be placed on the top disk where it was not in thermal contact with the actual specimen. The entire assembly fit into an insulating ring; a lead wire connected to a vacuum electrical feedthrough. In this fashion, electron current from the specimen could be read on an appropriate electrometer.

For transmission studies, the specimen-to-film distance had little effect on the photographic contrast, which is controlled by the operating voltage, specimen thickness and crystal perfection. A specimen-to-film distance of about 11 cm was chosen as a compromise between exposure time, angular divergence to be recorded on the film and Kossel line distribution on the pattern. With this distance, a maximum divergence angle of 70° is recorded on the film.

Patterns were recorded on standard 5 × 7 in (12.7 cm × 17.8 cm) x-ray film or glass plates held in an ordinary plate-holder cassett which fit into an aluminum frame bolted onto the camera bottom. The film was exposed in air, by placing a polyester window 0.13 mm thick and diameter 1 7/8 in directly below the specimen (fig. 14). The window was positioned in a removable cap and sealed by O-rings inside and outside. Window failure was rare provided normal care was exercised. Complete details of the entire system were presented by Vieth and Yakowitz [54]. Pertinent design features are shown in figures 13-16.

A. Loading Device for the KPG

Since the KPG described above was to be used for studies of strained materials, a loading device was thought to be necessary. I believe that for Kossel strain studies to be meaningful, the constraints must actually be applied to the specimen while the Kossel pattern is recorded. (Naturally, residual strain studies are an exception.)

The effect of removing the constraints leaves residual macrostresses which may be different on one crystal face with respect to another. Thus, a residual strain gradient can be expected to be present throughout the crystal volume. For these reasons, a tensile loading device was built which was compatible with the specimen stage supports of the camera module of the KPG.

Because of the size limitations, small but accurate load cells were required. The load was needed to ± 0.5 percent of the maximum load rating of the cell which was to be 100 pounds (45.4 kg). A single load cell of the required size and required accuracy over the range 0 to 100 pounds (45.4 kg) was not feasible. Therefore, two resistance strain gaged load cells rated at 0 to 10 pounds (4.54 kg) and 0 to 100 pounds (45.4 kg) were decided upon. The cells were specially designed for this application by The Brewer Engineering Laboratories. The dimensions of the cells are shown in figure 17 and calibration data for each load cell are shown in figure 18. The loading mechanism consisted of a lever and fulcrum arrangement having a nominal mechanical advantage of 30 to 1. The type 303 stainless steel lever, 3 in (7.5 cm) long, was advanced by a worm gear and spring-loaded in order to minimize backlash. Loading from outside the vacuum chamber was accomplished using a commercial 4 in (10 cm) diameter micrometer thimble, connected to the worm gear on the strain device with two universal joints coupled with sliding linkage.

The stage was connected to the goniometric drives by means of bearings and appropriate gears. The entire loading device rested on the three orthogonal drives; X-Y motion was accomplished by driving a ball slide mechanism with a micrometer shaft and vertical motion was obtained by the worm and wheel arrangement. The assembled tensile loader mounted in the Kossel camera is shown in figure 19a while the complete loading device is shown schematically in figure 19b.

A specimen having a reduced section of 1 in (2.54 cm) by 3/8 in (0.95 cm) wide was used. With a thickness of 0.003 in (0.076 mm), the 100 pound (45.4 kg) load gave a stress of 133,000 psi (0.926 GN/m²). The specimens were shaped in a special jig, removed, cleaned, and electropolished to the desired thickness. Then, stainless steel end pads were spot welded to both heads of the specimen to prevent tearing of the specimen. The specimen was returned to the jig and the end holes spaced 3.491 ± 0.0025 cm apart drilled. The accuracy of macrostress determinations was limited chiefly by nonuniformity of the cross section, as well as bending stresses introduced by the tensile load mechanism. However, the microstresses of interest when a polycrystalline material was under study were not greatly affected by these two problems.

The specimen was pinned into place using hardened 0.1 in (2.5 mm) diameter pins and the read-out unit observed to make sure that no load was applied during specimen insertion. If the goniometric drives were used, some load would be applied as the stage tilts; the maximum load has been measured as 182 g or 0.4 pounds from this source at which is nominally zero load. With a 0.003 (0.076 mm) in thick specimen this amounts to about 500 psi (0.035 MN/m²). All orientation of the specimen was done before beginning strain experiments, and it was rare that the full range of the goniometer was needed to accomplish this. In any case, if any load was impressed by the goniometer, it was small and known. Tests under load indicate that no change occurred in the load as a function of the orthogonal motions.

The load read-out console was a standard commercial unit reading percentage of full capacity of the load cell. Electrical stability of the combination of load cell and read-out console was achieved in a few minutes. The minimum adjustment obtainable with the thimble arrangement permitted incremental changes of 0.2 percent of the maximum load. Again considering the 0.003 in (0.076 mm) thick specimen, this corresponds to stress changes of about 30 psi and 300 psi (207 N/m²) using the 10 pound and 100 pound (4.54 kg and 45.4 kg) load cells respectively.

Tests indicated that drift as a function of time was not a serious problem. Both load cells were tested at several loads for 10 minutes and at one load for 8 hours. Maximum drift was 0.03 pounds (14 g). Complete details of the loading device have been presented by Vieth and Yakowitz [55].

B. Measuring Device for Kossel Patterns

The measuring device required accurate X-Y coordinate readings over a range of about ±2.5 in by ±3.5 in (6.35 by 8.9 cm). Many varieties of commercial comparators can achieve these requirements. For this study, a comparator built by Zeiss was used. Using this comparator, the Kossel pattern was viewed in transmitted light through an appropriate optical system with magnification ranging up from 1.5 diameters. The appropriate magnification seemed to depend on the particular pattern but about 2 to 3 diameters was the usual value. The X-Y motion was accomplished on micrometer lead screws; the eyepiece contained a Vernier scale. The precision (reproducibility) was better than 5 micrometers (3 is claimed by the manufacturer). The

X-Y coordinate positions of sharp Kossel cibuconics could be measured with uncertainties no greater than 10 micrometers using this comparator. The contribution of such uncertainties to the computed *d* values was very small compared to the other uncertainties discussed previously.

VIII. Results of Electron Probe Microanalysis Investigation Seeking Local Chemical Variations in Fe-3 Si

No significant variation in Si content was found in tests of homogeneity. More than 100 separate analyses were carried out for Fe and Si simultaneously while traversing several grains in a systematic fashion, and the data are shown in tables III and IV. Special positions such as grain boundaries or triple points are noted. Clearly, within the ability of the electron microprobe to measure a variation, no significant variation of Si content exists as a function of position in the specimen. Complete analytical details have been presented elsewhere [56].

The results for Fe and Si may be summarized as follows:

1. The silicon content is 3.14 percent (105 determinations).

2. The standard error *s* is 0.086 percent for Si.

3. The observed range of Si content is 2.89 percent to 3.29 percent.

4. We may be 99 percent confident that the mean Si concentration lies between 3.12 and 3.16 percent.

5. The 99 percent tolerance interval, i.e., the interval in which 99 percent of all future points tested are predicted to lie is 2.91 to 3.37 percent Si.

6. The percent coefficient of variation for Si is 2.74 percent ($\%CV = 100s/C_{Si}$).

7. The iron content is 96.87 percent (106 determinations).

8. The standard error for Fe is $s = 1.16$ percent.

9. The observed range of Fe content is 94.4 to 99.4 percent.

10. We may be 99 percent confident that the mean Fe concentration lies between 96.6 and 97.2 percent.

11. The 99 percent tolerance interval for Fe is 93.8 to 100 percent.

12. The percent coefficient of variation for Fe is 1.20 percent.

The only reasonable conclusion indicated by these results is that internal strains in Fe-3 Si are not caused by concentration gradients.

Some 3600 separate tests of homogeneity were carried out using six statistically selected samples of Fe-3 Si. A conservative estimate of the coefficients of variation for both iron and silicon was ± 1 percent. Wet chemical analysis of the Fe-3 Si alloy gave 3.22 wt% silicon [56].

One other observation is perhaps interesting. Figure 4 shows the average Si content versus lattice parameter. For 3.14 percent Si, figure 4 gives $\bar{a} = 2.86267$ Å as the bulk lattice parameter for the alloy. Gielen et al. have reported $\bar{a} = 2.86268$ Å for this material [37]. Such close agreement is probably fortuitous, but it is certainly encouraging to have the results of independent methods agree well.

IX. Obtaining the Kossel Stress-Strain Analysis

A typical specimen is shown prior to insertion into the loading device in figure 20. The reduced section is 2.54 cm by 0.63 cm. This specimen was machined from a sheet supplied through the courtesy of H. C. Fiedler (General Electric Co.). The original sheet was about 100 μm thick. This specimen was electropolished from both sides simultaneously to a thickness of 60 ± 5 μm as determined by several micrometer readings. Polishing was carried out in 5 percent perchloric acid — 95 percent methanol solution cooled to about 23 °C and achieved at 30 volts and 3 amperes with a 304 stainless steel cathode. About ten minutes were required for polishing. The specimen was then etched in warm 5 percent HF yielding a fairly rough surface.

A grain aligned nearly parallel to the direction in which the load could be applied was chosen for study. This grain is shown enlarged in figure 21. Surface roughness is seen in more detail in figure 22 which was taken with a commercial scanning electron microscope. The etchant attacks the surface in a very nonuniform fashion, producing a terraced effect which is seen near a grain boundary. In a qualitative sense, such etching behavior is usually associated with variations of locked-in strain energy.

After attaching the end pads and drilling the holes for the pins in the loading device, the samples were annealed at 350 °C for 2 hours in order to remove any handling strains. Heating and cooling rates were very slow in order to insure uniform heating and cooling off the specimen. Rapidly cooled test sam-

ples were found to bend or crinkle. Correctly annealed specimens were straight to the eye and dead-soft. Specimens in this condition were deemed suitable for Kossel internal stress-strain (KISS) analysis.

A qualitative view of strain contours can be obtained by x-ray topographic methods as well [57]. Such methods give some indication as to the boundaries of strain distributions by viewing the defects responsible for causing the strains. The higher the defect density, the higher the strain. On the other hand, the Kossel internal stress-strain (KISS) analysis can map the strains on a nearly quantitative basis. The trade-off is that mapping a given grain by the KISS method takes two to three orders of magnitude more time and effort than does the topographic method. This situation is responsible for the fact that until now, no grain in a polycrystalline material had ever been mapped by the KISS method.

Another problem is the tremendous amount of data needed to describe a single point in the KISS analysis. More than 100 separate numbers are needed to completely describe the point. For these reasons the grain shown in figure 24 was mapped at only three stress levels: (1) unstrained, (2) slightly compressed in the elastic region, and (3) slightly pulled in-tension in the elastic region. The axis of tension or compression was nearly $[115] \leftrightarrow [115]$. A few points were also obtained near the yield stress as well. We shall call these stress levels I through IV respectively. Based on the applied load of 0.3 pound and a cross-section of $(0.63)(0.006) = 0.0038$ cm², the macrostress at level III (tension) was not less than 200 psi or more than 600 psi. Crude specimen guides were used for the compression test — some bending may have occurred but that is doubtful. The macrostress for level II (compression) was between 200 and 800 psi (0.14 MN/m² and 0.56 MN/m²). At level IV, the macrotensile stress was between 40,000 and 60,000 psi (27.6 MN/m² and 41.4 MN/m²).

The reference point for all of the work was taken to be at the geometric center of the grain in the unstrained state. Two patterns were taken a few micrometers apart at the grain center. One of these patterns is shown indexed in figure 8. The d spacings for each were obtained by measuring the X-Y coordinates at 18 points on each of the lines of the pattern.

The optimum thickness and voltage requirements are such that the product $U\mu X$ can be as high as 7.5 (see page 24). For a thickness of 60 μm in Fe-3 Si, the value of μX using FeKα radiation is $(571)(0.006)$ or

3.43. The ratio 7.5/3.43 gives $U = 2.19$ or an operating voltage of 15 kV. Therefore, all Kossel patterns in this work were prepared using an operating voltage of 15 kV.

Equation (11) was used to calculate the exposure time for the patterns. Two types of film were used, Kodak AA, a moderately coarse grained duplitized film, and Kodak M plates, a moderately fine grained single emulsion plate. The plates were used to improve resolution and to preclude the possibility of nonuniform film shrinkage during photographic processing. This was done even though Gielen et al. showed that the effects of nonuniform film shrinkage in AA film were negligible [37]. The values for E_0 in eq (11) are 1.6×10^8 photons/cm² and 1.4×10^9 photons/cm² for the film types AA and M respectively [34]. Other values for substitution in eq (11) were $r = 0.27$, $n_0 \simeq 1.5 \times 10^{-4}$ photons/electron at 15 kV, $X_f = 0$, $\mu_s X_s = 3.43$, $\eta = 35°$ and $Z = 10.526$ cm.

The results give $t_E i_s$ equal to 0.33 and 0.034 for types M and AA respectively. The value of i_s is typically 0.01 to 0.1 μA. Thus, exposure times of a few minutes to half-hour were employed to obtain the patterns for this study.

But before accurate "d" spacings could be computed it was necessary to measure the source-to-film distance, Z, as accurately as possible. Therefore, the Fe-3 Si specimen described by Gielen et al. [37] was placed into the Kossel pattern generator. The area they used to determine the lattice parameter as 2.86268 Å was located by means of the electron beam contamination mark. The specimen was oriented so that the (220) conic (fig. 8) was made a circle. In gnomonic projection the diameter, L, of the (220) conic is then

$$L = 2Z \tan(90 - \theta)_{220} \qquad (55a)$$

Applying Bragg's Law and the identity $\sin\gamma/\cos\gamma \equiv \tan\gamma$ we get

$$Z = L[\lambda/\sqrt{2(a^2 - \lambda^2)}], \qquad (55b)$$

γ being the wavelength of Fe-K$\alpha_1 = 1.936042$ Å. For each pattern, nine measurements of L were averaged to get the final value. The experiment was repeated 43 times over the course of several weeks and each plate processed shortly after exposure. Temperature variations inside the Kossel camera were very small.

The results give $Z = 10.5261$ ($s = 0.0180$) cm. The half-width of a 95 percent confidence interval is $w_{95} = 0.0055$ cm. Reference to figure 11 shows the uncer-

tainty due to Z will be 0.001 for $\theta = 30°$ and less than 0.0001 for $\theta > 55°$. In all of the subsequent work, Z was taken as 10.5261 cm.

Equations 16-19 were programmed in the BASIC language for processing on a General Electric 265 digital computer in the time-sharing mode. A typical printout for one conic is shown as table V. The input data consist of the 234 (13×18) X,Y coordinate measurements, X_0Y_0 position, Z value, (hkl) indexes and wavelength used. One X_0Y_0 measurement is taken after each conic is completed and the results averaged to give the X_0Y_0 value actually used. The "d" values obtained from the reference patterns were averaged and are listed in table VI. *All* "d" values obtained subsequently were referred to these "d" values in order to obtain the $(\Delta d/d)$ data for the stress-strain analysis. Thus, it must be understood that all the stress-strain data refer to the center of the grain in the so-called unstrained condition, i.e., as the customer for Fe-3 Si sheet would obtain the material.

The justification for this procedure is that table VI shows the d spacings for planes within a given family to vary. Hence, the unstrained crystal is *not* really unstrained despite process annealing and careful handling. However, on an absolute basis, the strain at the point chosen for reference is small as indicated by the relatively small variations in the d spacings and the sharpness and resolution of the pattern shown in figure 8. The lattice parameter at the reference point is 2.86154 Å. The average lattice parameter of the material is 2.86268 Å. The average lattice parameter of the material is 2.86268 Å so that $\Delta a/a = (2.86154\text{-}2.86268)/2.86268$ is -0.0004 or -0.04 percent.

In order to observe variations of the lattice parameter, a, as a function of position within the grain, a program using weighted least squares fit of the d spacing data was prepared. The logic is as follows:

a' is the apparent a value for a given conic

X is the Nelson-Riley factor $= 0.5 \left[\dfrac{\cos^2 \theta}{\sin \theta} + \dfrac{\cos^2 \theta}{\theta} \right]$

σ is the standard error for d for a given conic.

Each of these parameters is computed by the program giving "d" spacings illustrated in table V. Then:

$$w_i \equiv (1/\sigma_i)^2 / \Sigma (1/\sigma_i)^2 \qquad (56a)$$

$$\bar{a}' = \Sigma a_i w_i / \Sigma w_i \qquad (56b)$$

$$\bar{X} = \Sigma X_i w_i / \Sigma w_i \qquad (56c)$$

$$b = \Sigma w_i a' (X_i - \bar{X}) / \Sigma w_i (X_i - \bar{X})^2 \qquad (56d)$$

$$a = \bar{a}' - b\bar{X}. \qquad (56e)$$

This procedure yields the statistically most valid estimate of the lattice parameter, a. The lattice parameter at the reference point was found as 2.86154 Å by this method. Lattice parameter data were only computed for the so-called unstrained condition. Cubic lattice parameters ought not to be reported for material deliberately placed under load.

Next the equations in the section on stress-strain analysis were programmed for the computer. All programs were written in BASIC for the time-sharing mode. The stress-strain programs are modular so that each desired property can be gotten in a logical form. The program library is as follows:

MODFIT — Yields strain data from pattern, i.e., $(\Delta d/d)$. Inputs: X,Y,Z coordinates from film.

STANLY — Yields average lattice strains ϵ_{11}, ϵ_{22}, ϵ_{33}, ϵ_{13}, ϵ_{31}, ϵ_{12} from Miller indexes and $(\Delta d/d)$ from MODFIT. These strains are in the cubic frame. Also yields estimate of the errors on each strain.

PRNSTR — Yields principal strains S_1, S_2, S_3 from data of STANLY.

STEROR — Yields error estimate of the principal strains.

PRAXES — Yields principal strain axes direction cosines from data of STANLY and PRNSTR. A cubic to principal frame transformation is implied.

UNDEFD — Yields direction cosines of principal strains before deformation. Input from STANLY.

DANGLE — Yields angle between principal strain axes before and after deformation.

STRESS — Yields stresses σ_{11}, σ_{22}, σ_{33}, σ_{23}, σ_{31}, σ_{12} in the cubic and principal frames. Inputs from PRAXES and STANLY and external matrix of elastic constants.

STRAPP — Yields principal stresses, P_1, P_2, P_3.

MAXSHR — Yields maximum shear strain in (hkl) planes. Inputs from PRAXES and PRNSTR.

DISNUM — Yields geometric distortion number from invariants of strain tensor. Input from PRNSTR.

STELEN — Yields total stored elastic energy.

SHELEN — Yields shear stored elastic energy.

CUTRAN — Transformation from principal to cubic frame.

27

Figures 23-25 show the location of each pattern within the grain for stress levels I-III. These locations constitute the points from which the maps in the results section were obtained. The number and location of points at each level were adequate to map the stress-strain and energy contours reasonably accurately for levels I-III — certainly within the accuracy implied by the limitations of the KISS method itself.

In summary, the KISS data were obtained at four stress levels, three of which could be mapped. Each pattern required about 250 individual X,Y coordinate measurements, on which the entire KISS analysis was based. Each step in the stress-strain analysis was programmed for digital computer in the BASIC language. Thus, results from each step could be tabulated and compared directly. The center of the "unstrained" grain was used as a reference point for the stress-strain contour mapping.

X. Results of the Kossel Internal Stress-Strain Analysis

The d spacing values for the as-received material are shown in table VI. The lattice parameter, a_0, computed by the weighted least-squares program is also included. Gaps in the table occur where it was not possible to obtain 18 valid coordinate measurements for the conic in question. In the case of (112) and $(11\bar{2})$ types, often not enough of the conic was present on the film to permit valid sampling. In the case of other conics, contrast was occasionally so poor that proper measurement was impossible.

Table VI shows that the lattice parameter varies as a function of position within the grain. Variations of lattice parameter within a grain of a polycrystalline sheet have also been observed in several other cubic materials [58]. The average lattice parameter for points in the grain is 2.8627 Å which is in good agreement with the lattice parameter reported for the bulk [37]. However, the two points in adjacent grains are somewhat lower than this value. Note also that the highest value of the lattice parameter occurs at a grain boundary location. The variation of the lattice parameter within the grain is shown in figure 26. The lattice parameter is, on the average, a bit lower on the side nearest the point where three grains meet (left side of fig. 26). A straight line path from the center of the grain to any point on the boundary almost always entails a change of at least 0.0005 Å or

about 0.02 percent in the lattice parameter. Beyond this, knowledge of the lattice parameter alone does not provide much useful information.

Values of $\Delta d/d_0$ for all four stress levels are given in table VII. Gaps occur for the same reasons that were enumerated for the d spacing values in table VI. These $\Delta d/d_0$ data were used to derive the average Cauchy strains with the aid of eq (24). Table VIII gives the computed Cauchy strains and their standard errors as calculated from eq (51).

The data in table VIII were used to compute the principal strains which are listed in table IX. The standard errors associated with the Cauchy strains were also used in an effort to estimate the maximum credible error on the principal strains in table IX.

This estimate was made by differentiating eq (27) and inserting the standard errors on the Cauchy strains for the $d\epsilon$ terms. This procedure maximizes the effect of each standard error in table VIII and also assumes these errors to have a Gaussian distribution. The orthogonality of the principal strains was crudely taken into account by merely dividing the final result by a factor of three in order to obtain an estimate of the maximum error for each principal strain. The reasoning is roughly analogous to that used to show the volume coefficient of expansion in three times the linear expansion coefficient [59]. Despite its crudity, this method very nearly reproduced all of the maximum credible error data on principal strains in tungsten compressed 0.2 percent reported by Newman, Glass and Weissman [60]. Therefore, the values reported in table IX are probably reasonable estimates of the maximum credible error associated with an individual computation of a principal strain.

Table IX shows that for very small principal strains, the maximum credible error often equals or even exceeds the computed strain value. From this, one concludes that the KISS method can record the presence of very small strains but that apparently their magnitude cannot be measured with high accuracy. Aside from this, there is little in table IX to refute the reliability analysis results discussed previously. Accordingly, the principal strain values in table IX will be taken as satisfactorily reliable estimates of the true values.

The entire exercise of computing maximum credible errors was undertaken as a final precaution in accepting the computed principal strain data. This precaution was necessary because all of the subsequent results in the KISS analysis depend directly

28

or indirectly on the magnitude of the principal strains and/or on the values of the cubic elastic constants C_{11}, C_{12} and C_{44}. For purposes of calculation, the elastic constants of iron were used. These values are $C_{11} = 237$ GN/m²; $C_{12} = 141$ GN/m²; $C_{44} = 116$ GN/m² [61]. (One giganewton per square meter is 145,038 psi.)

Tables X-XVII include the results of the entire KISS analysis for the four stress levels investigated. The stress-strain configuration for a single position at one stress level requires more than 100 numbers for a complete description. Obviously, this requirement is cumbersome and unwieldy but, worse, it is difficult to get a clear picture of the situation from the numbers alone.

Note that table XVII also includes that portion of stored elastic energy assigned to shear called W_S. This value can be obtained from an equation derived in detail by Slade et al. [44]. This equation is given as:

$$W_S = 0.5(S_1 - S_3)^2 \{ C_{44} - 0.25(C_{12} + 2C_{44} - C_{11})$$

$$[(l_{11}^2 - l_{13}^2)^2 + (l_{21}^2 + l_{23}^2) + (l_{31}^2 + l_{33}^2)^2] \} \quad (57)$$

Slade et al. [44] showed that the total stored elastic energy could be partitioned into two energy terms $W = [W_N + W_{NS}] + W_S$. The composite term, $W_N + W_{NS}$, represents a composite of energy terms deriving from normal strains (W_N) and a mixture of normal plus shearing strains (W_{NS}). These latter two terms cannot be unambiguously separated but, as indicated above, W_S can be. Hence, we may obtain the ratio of the shear stored energy to the total stored energy, W_S/W. Of course, the composite term is just $W - W_S$.

Most of the results in tables X-XVII were plotted as area maps (figs. 27-39) of the grain shown in figure 21. These maps reveal the existence and extent of a variable strain distribution (VSD) within the grain on at least a semiquantitative basis. The maps represent the first plot of variable strain distribution in an opaque polycrystalline materials on any basis beyond the qualitative views of dislocation clusters obtained by x-ray topographic methods.

The maps in figures 27-39 were prepared by connecting each point in figures 23-25 using the data in tables IX-XVII and then using linear interpolation to get from one point to the next. All indicated boundaries were then linked to prepare the final map.

Attempts to obtain Kossel patterns directly at a grain boundary met with failure. Traces of two grains were always present. Figure 40 shows a typical result where the displacement of the 110 poles of the two grains permits an estimate of the misorientation at the boundary. Typical values are 1 to 3 degrees of arc. This grain boundary mismatch can lead to high stresses at the boundary, and it indicates that the texture differs locally from the desired (110) [001].

The maps in figures 27-38 clearly show the existence of VSD at all stress levels investigated including the so-called unstrained condition. The maps show a more random distribution of the VSD for the as-received material than for the compressed or stretched situation. Although it is oversimplifying matters, the VSD appears to be "squeezed" in the compression case and to be "lined up" in the direction of the applied load in the tensile case.

First, note the similarity between the principal strain maps figures 27-29 and the lattice parameter for the as-received material. While not greatly surprising, there is clear evidence that the lattice parameter is entirely related to the local strain conditions in the textured Fe-3 Si sheet. The bulk lattice parameter of 2.8627 Å is apparently the "equilibrium" done in conventional determinations of a_0 values.

The principal strain maps for the compressive and tensile cases show rearrangement of the VSD and an increase in the size of regions with higher absolute principal strains. Certain small areas of high strain have been removed, e.g., the area at the right of figure 27a, and are incorporated into these larger regions. Figure 27c shows the existence of a highly strained region within the grain core. It is probably the existence and propagation of such regions which cause the degradation of electrical properties observed when the nominal elastic tension is increased beyond 500 psi.

The principal stresses associated with the principal strains are shown in figures 30-32. Note that the maximum principal stress associated with the highly strained region in the core is more than 2 GN/m² or more than 250,000 psi. In the as-received condition, a somewhat smaller region of similar maximum principal stress was present (fig. 30a).

Local regions in the Fe-3 Si polycrystalline aggregate are under stresses of more than a quarter million psi in the as-received material and larger regions of high stress exist in the loaded sheet. There are alternate regions of tensile and compressive stress. A merit figure consisting of the algebraic sum of $P_1 + P_2 + P_3$ from table XIII was calculated in an

attempt to delineate these alternate regions and the result shown in the maps of figure 33.

The original grain appears to be in compression throughout most of the left side of figure 33. Tension is present at the center and right center, then compression and finally there is the small region of very high tension at the extreme right. In the case of the compressive load, all but a small portion of the grain is in compression. For the tensile load, most of the grain is in tension, but two areas near the boundary on the left side of the grain are in compression.

All of these observations tend to indicate that neighboring grains press into the grain of interest, approximately along the lines shown in figure 34 during processing to the as-received sheet. Even under tensile load, there is a compressive strain resulting from a tendency for the neighboring grains to "squeeze" the grain in a direction roughly perpendicular to the loading direction (see fig. 32c). This grain exhibits shear strain. A number of regions in the grain have nearly as principal strains S, O, $-S$ as listed in table IX. In addition, several other regions have one nearly zero principal strain. When the S, O, $-S$ configuration exists, the region is in simple shear. Furthermore, the ratio of the shear stored elastic energy to the total stored elastic energy is very high throughout the grain as shown in figures 35-37. This situation obtains for all stress levels investigated.

Slade et al. [44] have shown that typical conditions for the existence of a plane of nearly zero normal stress occur when $S_2 = 0$, $S_1/S_3 = -\rho^2$. Using the positive sign, the axes of this plane referred to the principal strain can be represented as a matrix, B, such that [44]

$$B = \begin{bmatrix} \dfrac{-\rho}{(1+\rho^2)^{1/2}} & 0 & \dfrac{1}{(1+\rho^2)^{1/2}} \\ 0 & 1 & 0 \\ \dfrac{1}{(1+\rho^2)^{1/2}} & 0 & \dfrac{\rho}{(1+\rho^2)^{1/2}} \end{bmatrix} \qquad (58)$$

If we call the matrix representing the principal strain axes (table X) A, then $B_C = A^{-1}B$ where B_C represents the axes of matrix B in the cubic frame.

Examination of table IX reveals that more than two-thirds of the patterns studied yielded principal strains such that $S_2 \simeq 0$ and S_1 and S_3 of opposite sign. The B_C matrix was calculated for each of these patterns. The results are listed as table XVIII. Furthermore, the poles of these planes of nearly zero

normal stress were plotted on $\langle 110 \rangle$ stereographic projections (fig. 41). The poles of the approximate great circles on which the points lie are nearly of the type $\{351\}$. Apparently, the direction along which planes with minimum normal stresses and maximum shearing strains lie is approximately of the type $[351]$. The magnitude of the maximum shear strain in these planes is given by $2(-S_1S_3)^{1/2}$ according to Slade et al. [44]. This value is the maximum shear strain in any plane.

Table XIV shows that for stresses in the principal strain frame, the shearing stresses, σ_{23}, σ_{31}, σ_{12}, are in most cases lower in magnitude than the normal stresses. Slade et al. have shown that in such a case, the principal strain axes and the principal stress axes nearly coincide [44].

Examination of table X shows that the principal axes of strain after deformation often lie within about $20°$ of $\langle 110 \rangle$ or $\langle 100 \rangle$ type poles. This circumstance may result from mechanical anisotropy in the oriented sheet.

There exists a set of three axes subject to maximum strains with respect to strains of linear elements in all other directions [62]. The angle between these axes (table XI) and the principal strain axes is shown in table XII. In many cases, there is little difference in direction but a change in sense as represented by rotations of nearly $180°$. Many of the other rotations are nearly 30 or $60°$. The cases where $\theta_i \simeq 180°$ or $0°$, $\theta_j \simeq 0$ and $\theta_k \simeq 30°$ or $60°$ occur with significant frequency among those patterns for which a shear plane can be deduced. As we shall see later, this type of rotation of the axes is consistent with stresses induced by the response of the Fe-3 Si to mechanical anisotropy. To a first approximation, the line of action or resultant stress due to mechanical anisotropy can be predicted to lie 30 to $60°$ from $\langle 110 \rangle$ or $\langle 001 \rangle$ type poles (see sec. XII).

The total stored elastic energy tends to follow the principal strain and principal stress configurations as shown in figures 27-32 and 35. The average stored elastic energy in the grain does not vary greatly from that in the as-received state when the low compressive or tensile macrostresses used in this study are applied. In all probability, these stresses are not enough to seriously degrade the magnetic properties [3,4] or to significantly alter the magnetic domain pattern [9].

A large portion of the total stored elastic energy is shear energy as shown in figures 36 and 37. This imbalance probably results from the propensity of the

Fe-3 Si sheet to shear in response to stresses induced on cooling from 1200 °C by the mechanical anisotropy of the oriented grains.

The distortion number is also large in most instances (fig. 38). The ratio W_s/W is related to the distortion number [44]. Note that, in many cases, the distortion number and W_s/W are nearly equal (table XVII and fig. 37).

The maximum shear strains in potential slip planes as well as in {100} type planes are listed in table XVI. The high locked-in shear strains tend to indicate that slip as a general stress-relief mechanism has not occurred. Usually, one or two values of the maximum shear strain are low compared to the others. In fact, there appears to be, roughly, a set of nearly equal low values, a set of intermediate values and a set of high shear strains at each point. In addition, the maximum shear strain in {100} types is often less than in several potential slip planes. The "three levels" of locked-in shear strain follow roughly the predictions obtained by computing the resolved shear stress RSS factors for potential slip systems which, for instance, show that (101) $[1\bar{1}\bar{1}]$, $(10\bar{1})$ [111] and $(01\bar{1})$ [111] have nearly equal RSS factors. On the other hand, (110) $[1\bar{1}\bar{1}]$ and $(1\bar{1}0)$ [111] types have low RSS factors.

Attempts to correlate maximum shear strain data with position in the grain and applied load met with frustration. There appears to be a more or less random response to the applied load. General slip is inoperable and twinning does not occur either. One might guess that some local "critical resolved shear stress" caused one or two potential slip planes to give up their strain energy but not the others. The behavior of the {100} types remains something of a mystery. The variation of the maximum shear strain in (112) sheds no real light on the problem (fig. 39). Perhaps when slip does become operable under mechanical deformation, it follows the "trends" in table XVI. Such behavior may indicate why slip in Fe-3 Si is relatively poorly understood [63,64,65].

The only conclusions, then, that can be drawn from the maximum shear strain data are that: (1) general slip is inoperable; (2) some shear strain relief occurs in some planes apparently in response to local stresses set up by the stress-strain subregions; and (3) the three-level nature of the maximum shear strains contributes to raising the distortion number [44].

In summary, the experimental results show that there is a variable strain distribution in the as-received sheet and that these subregions are altered by external loading. There appears to be a strong tendency for the Fe-3 Si to accommodate internal stresses by some sort of shear mechanism; a large portion of the stored elastic energy is shear energy. The VSD is not caused by local variations in iron or silicon content. Now the results can be considered in the context of the metallurgy of the Goss oriented Fe-3 Si sheet.

XI. Metallurgical Aspects Pertaining to the KISS Results

The Fe-3 Si sheet which the user receives is clearly not strain free. Figures 27-39 show that there is a variable strain distribution (VSD). Apparently, the net effect of this VSD in the entire as-received material results in a residual compressive stress in the sheet [4]. Furthermore, the silicon and iron distribution is entirely uniform. Thus, major element compositional variations play no role in causing the VSD.

The VSD observed almost certainly must have been created no earlier than the texture anneal (see fig. 3) but, beyond this, it is impossible to state exactly how and at what point in the history of the material the VSD was formed. However, each possible contributing factor to VSD formation can be considered in the light of the results shown in this study.

The (110) [001] grains grow by the process of secondary recrystallization. Secondary recrystallization is the selective grain growth of only a few grains, as distinguished from uniform growth, when the new set of grains formed on primary recrystallization is subjected to further annealing. The texture after primary recrystallization in Fe-3 Si is extremely complex [66]. However, the primary texture always contains some (100) [001] components [67]. Strangely, the final Goss texture does not seem to depend strongly on the amount of (100) [001] in the primary texture [67] but only on the fact that some (110) [001] grains are indeed present.

Primary recrystallization occurs to relieve the cold rolling strains set up throughout the metal. In the case of Fe-3 Si, primary recrystallization is carried out at about 800 °C. Hu [68] has shown that the primary texture probably grows by subgrain coalescence in Fe-3 Si [68]. The removal of the subgrains lowers the free energy of the system. Some (110) [001] grains form because these grains or-

dinarily have the lowest surface free energy of all grains [67]. The primary texture has been described in detail but the exact relationship of the primary texture to the Goss texture is still not completely understood [67]. The rate of grain boundary migration for a primary (110) [001] grain at 800 °C is between 0.005 and 0.01 μm per second [69]. At a rate of 0.005 μm/sec, a circular grain would increase its diameter 1 μm every 100 seconds. Thus, after a two-hour anneal we would expect the (110) [001] grains in the primary texture to be between 50 and 100 μm in diameter.

Such (110) [001] primaries grow rapidly during the secondary recrystallization step (the texture anneal) at 1200 °C. The grain boundary migration rate is 18 μm/sec [67]. This growth rate falls by about 5 percent for each degree of misorientation of the grain from a true (110) [001] [70]. The rate of grain growth is determined by the grain boundary mobility, M, times a driving force, P [67]. The driving force term depends on surface tension differences between grains, the sheet thickness, the actual grain size and the surface energy of each grain [67]. Typical numerical values at 1200 °C for (110) [001] grain growth are $M = 2.5 \times 10^{-8}$ cm^4/erg sec and $P = 7.2 \times 10^4$ erg/cm$^3 = 7.2 \times 10^3$ N/m$^2 \approx$ one pound per square inch [67]. (Note that the foregoing is 1 pound per square inch of grain boundary.)

Under vacuum conditions or an oxygen free atmosphere, the (110) [001] grains have the greatest driving force of all grains in the array [71]. Nevertheless, it is commercial practice to add a dispersed second phase such as MnS or silicon nitride in order to restrain normal grain growth. The ability of the inclusions to perform this function depends on their size and distribution. MnS has been added by heating the primary matrix to 1325 °C to dissolve the inclusions and then cooling at 130 °C/min. This treatment led to small well-dispersed inclusions in the matrix [72]. After the final texture anneal, these inclusions were distributed in the grain boundaries of the Fe-3 Si sheet [102]. In commercial practice, some of the inclusions would be removed by reaction with a coating on the Fe-3 Si sheet (see fig. 3).

The stress field around these leftover inclusions may be approximated by assuming the Fe-3 Si is an elastically isotropic medium near the inclusion. The stress field around a spherical inclusion can then be expressed as follows [73]:

$$\sigma_{11} = \frac{2G(a')^3(1-k^3)(1+\mu)}{9(1-\mu)}\left[\frac{1}{r^3} - \frac{3X^2}{r^5}\right] \quad (59)$$

where G is the bulk shear modulus ≈ 70 GN/m^2 for Fe-3 Si

a' is the radius of the inclusion ≈ 1 μm in Fe-3 Si [72]

μ is Poisson's ratio ≈ 0.29 in Fe

k is a/a', a being the spherical "hole" into which the inclusion is forced; k is always less than 1

r is $(x^2 + y^2 + z^2)^{1/2}$ where x, y, and z are the coordinates of a point in the medium. For simplicity, the center of coordinates is at the center of the inclusion.

With the appropriate substitutions, eq (59) reduces to

$$\sigma_{11} \approx 56\,(1-k^3)/X^3 \quad (\sigma \text{ in GN/m}^2) \quad (60)$$

if a point on the X-axis is chosen for examination. The stresses indicated in eq (60) serve to retard normal growth. These stresses must also tend to act as a drag on the growth of the desired (110) [001] grains as well. In fact, when the texture is almost all (110) [001] grains, the impurity stresses in the grain boundaries probably tend to halt the growth of these grains prematurely (or at least to slow growth drastically, which for all practical purposes is the same thing). Such an occurrence could account for the relatively large spread of orientations about a true (110) [001] found in the final sheet stock.

There is strong evidence that the closer a grain is to exactly (110) [001], the more it is favored for growth [67, 70]. Thus, perfectly oriented (110) [001] grains will grow at the expense of slightly misoriented (110) [001] grains. But the impurities tend to retard all grain growth and so a comparatively large number of slightly misoriented grains can result. After removal of the impurities and during the slow cool from 1200 °C, some grain growth favoring orientations very close to (110) [001] occurs—the effect of this is probably to get rid of the grains with the most misorientation and to reduce the size of other misoriented grains with respect to those very near (110) [001]. Nevertheless, the impurities almost certainly cause a greater orientation spread around (110) [001] than would be expected in the absence of impurities. The spread around (110) [001] in material of the type studied here is about ±15° [74].

Any impurities not removed from the Fe-3 Si sheet can act as stress concentration points at the (110)

32

[001] grain boundaries. Indeed, failure of the sheet under mechanical deformation is almost always initiated at these leftover inclusions [75]. The difference in thermal expansion characteristics of these leftover inclusions and the metal may also serve to concentrate stresses along grain boundaries when the sheet is cooled.

An approximate calculation of these impurity induced cool-down stresses can be carried out as follows: Assume the inclusion is spherical and compute the volume change difference on cooling from 1200 °C between the inclusion and a like-sized sphere of the metal. A MnS inclusion will have a thermal coefficient of expansion, α_T, equal to about half of α_T for the metal [76]. For Fe-3 Si, $\alpha_T = 1.2 \times 10^{-5}/°C$ [61]. Then for a 1-micrometer radius sphere cooled 1200 °C, the new metal radius would be 0.9856 μm but the actual inclusion radius is 0.9956 μm. The value of (1-k^3) in eq (59) is then $(0.9956^3 - 0.9856^3)$ or 0.021. Thus, the relation for the cooling stresses near the inclusion becomes $\sigma \approx 1.2/X^3$ with σ in GN/m^2 and X, the linear distance from the inclusion, in μm. This relation gives σ of 1.2 GN/m² (175,000 psi) for $X = 1$ μm and 1.2×10^{-3} $^{GN/m^2}$ (180 psi) for $X = 10.0$ μm from the inclusion, respectively.

On the other hand, Si_3N_4 has α_T of about $0.2 \times 10^{-5}/°C$ [76]. Thus, the use of Si_3N_4 inclusions of the same size as MnS inclusions would result in higher grain boundary stresses. All other things being equal, MnS is then the better inclusion of the two to use since it will cause lower grain boundary stresses.

The effect of misfit grains may be considered using the same reasoning. The final sheet contains typically 90 percent of (110) [001] grains and about 10 percent misfit grains. These misfits are almost entirely small grains having an orientation near to (100) [001]. Such grains form because the difference in driving force for secondary recrystallization is nearly equal for (110) [001] and (100) [001] types. Occasionally, local energy imbalances or a very poorly oriented (110) [001] grain make token growth of the (100) [001] energetically favorable. Cursory examination of several regions in the Fe-3 Si sheet from which the specimen in figure 20 was taken indicates that, roughly, the diameter of the (110) [001] grain is about five times the diameter of the misfit grain.

Thus, we may consider the misfit as analogous to very large inclusion in the (110) [001] array. The equation representing the stresses caused by the misfit is eq (69) [77]. Hence, we conclude that the

misfit causes high stresses at the boundary between it and its (110) [001] neighbors. The effect is probably negligible a few hundred micrometers away from the boundary.

Up to this point, stresses and other consequences introduced by the metallurgical procedures used to make Fe-3 Si sheet have been discussed. Now, the effects of the mechanical anisotropy of Fe-3 Si must be considered. These effects can assume their greatest importance during the cooling from 1200 °C.

The mechanical anisotropy is caused by differences in Young's modulus, Y, and the shear modulus, G, as a function of direction: $Y_{[110]}$ is 216.5 GN/m² while $Y_{[100]}$ is 131 GN/m². In turn, $G_{[110]}$ is 66.2 GN/m² while $G_{[100]}$ is 111.7 GN/m² [61]. If the Fe-3 Si were not oriented in a special fashion, the effects of the mechanical anisotropy would be averaged out over the great multiplicity of grain orientations. But after secondary recrystallization, virtually the entire sheet has a rolling plane direction of [$\bar{1}$10]; the rolling direction [001] is perpendicular to [$\bar{1}$10]. Therefore, the effects of mechanical anisotropy in the sheet can assume maximum possible importance.

Consider the Goss oriented sheet in figure 1. The effect of the difference in Young's modulus as a function of direction will be that shrinkage on cooldown from 1200 °C will occur more easily along the sheet, [001], than across the sheet, [$\bar{1}$10]. Thus, there can be a tendency for the sheet to bend around the [$\bar{1}$10] direction or axis.

Now the product $\alpha_T \Delta T$ on cooling Fe-3 Si from 1200 to 25 °C is 0.014. The maximum possible differential cooling stress will be given by:

$$(Y_{[100]} - Y_{[110]}) \alpha_T \Delta T = \sigma_{c,max} = 1.21 \text{ GN/m}^2 \approx 175,00 \text{ psi}$$

(61)

Equation (61) assumed equal shrinkage along [$\bar{1}$10] compared to [001]. Because of constraints placed on the grain by neighboring grains and because of stress relief due to plastic deformation and especially shear, we would not expect a 1.2 GN/m² stress to be present throughout the grain. But the results of the KISS analysis clearly indicate regions within the as-received material where such stress levels do indeed obtain. Shear may occur in response to the effect of the stresses set up by the Young's modulus differences. Recall that $G_{[110]}$ is 66.2 GN/m² and $G_{[110]}$ is 111.7 GN/m². Thus, there is a tendency for the differences in Y values to force a spherical grain into an

33

ellipsoid constrained by its neighbors which is opposed by a tendency to shear along some path to relieve the stresses set up by such a process. This shear mechanism is favored because $G_{[110]}/G_{[100]} = 0.59$ but $Y_{[110]}/Y_{[100]} = 1.65$.

The results of this study indeed show that Goss oriented Fe-3 Si has a strong tendency to endure shear. The poles of the planes of nearly zero normal stress and maximum shear strain are plotted in figure 41. The pole of these planes is also indicated. The directions in which nearly zero normal strains occur should be nearly perpendicular to the $\langle 351 \rangle$ direction. This direction lies in a plane common with $\overline{1}15$ and 110. The $\overline{1}15$ is the sheet orientation for this particular grain.

Apparently, the mechanical anisotropy of the oriented sheet causes shear to occur in order to relieve stresses encountered on cooling from 1200 °C to room temperature. Such a mechanism would explain the high ratio of shear energy to total stored energy in the grain in the as-received condition. The high values of the maximum shear strains in potential slip system of types $\{110\}$ [111] and $\{112\}$ [111] indicate that slip may be imminent and may occur locally to relieve very high stresses. But general slip has not relieved the shear stress. Perhaps this is because the estimated cooling stress is below the macroyield point for the Fe-3 Si so that plastic deformation can only occur locally to relieve regions of very high stress, i.e., near a leftover impurity or a misfit grain.

The sheet may actually bend somewhat in response to the mechanical anisotropy. The thermal flattening step (see fig. 3) is meant to remove bending so that the sheets can be inserted into transformer cores without high stresses. In this process, the Fe-3 Si sheets are stretched in tension at some temperature around 200 to 300 °C. This temperature is low enough so that major alterations of the texture will not occur [68]. Bending is eliminated by a process akin to "tensile creep." This process effectively puts back some of the bending stresses into the sheet. These stresses are far less than if the sheet had merely been cold flattened in the transformer core.

The final stress relief anneal tends to remove some of these stresses and to reintroduce cooling stresses again initiating some bending. The net result is some bending stress plus a shear stress in the final sheet.

The thermal flattening process almost certainly introduces subgrains into each major grain. This comes about partly because the low angle boundaries and random dislocations remaining after the texture anneal can coalesce [78]. The subgrains probably represent incipient recrystallization within the (110) [001] grains. They form to reduce the stresses just discussed.

The size and shape of subgrains in a single crystal of Fe-3 Si have been observed by the anomalous transmission of x rays [79]. Perhaps it is not unreasonable to assume that the final VSD is delineated by the subgrain boundaries formed in the thermal flattening step. The stress-relief anneal following thermal flattening probably causes a bit of subgrain boundary growth and some smoothing of the VSD. From the foregoing, I surmise that the as-received material has a VSD proportional to the size of the subgrains formed in the thermal flattening process.

Often (table X) the principal strain axes are near the directions [100] and [110]. Furthermore, the principal stress axes nearly coincide with the principal strain axes. This behavior is possibly a consequence of the two-dimensional nature of the stress field.

In many cases (table XII), the principal strain axes differ only little from the undeformed fiber on which the principal strains acted. According to Varga [62], the undeformed fibers represent a set of three directions in space such that linear elements placed along them in the undeformed state will be subject to maximum strains with respect to strains of linear elements in all other directions. Perhaps when the Fe-3 Si sheet is strained, the maximum stresses and strains act along the [001] and [110] directions in order to maintain the stored energy at its lowest possible value. Certainly these directions are favored for texture growth in order to reduce stored energy. So, by analogy, it may well be that the maximum stresses and strains are forced onto these directions for the same reason. The frequent 30 or 60° rotation (table XIV) would be consistent with a shear path caused by plastic mechanical anisotropy.

Apparently, mechanical deformation by slip does not occur easily in order to relieve the locked-in stresses. Maximum shear strain data in potential slip planes show a great deal of variability (table XV). Furthermore, the maximum shear strain in some nonpotential slip planes, $\{100\}$, is often less than in $\{110\}$ and $\{112\}$ types. Ocasionally, there is a precipitous drop in one or two potential slip planes after deformation. Probably, local slip has occurred

to relieve stress-strain concentrations such as that occurring at the extreme right of figure 30a. The variability in the maximum shear strain data accounts for the high values of the distortion number found [44]. (See table XVII and fig. 38.)

Slip behavior in Fe-3 Si is unusual in any case. Slip bands almost always tend to propagate from a grain boundary and often do not extend very far into a grain [64]. In order to propagate a slip band, almost all of the potential slip planes must act to rid themselves of their shear strain—not one or two. Some external load is needed to accomplish this. A guess would be that slip lines in the grain in this study would propagate first from the grain boundary at the extreme right of figure 27a in order to relieve the very high stresses at that point.

There are many small regions in the grain studied where one or more than one principal stress exceeds the macroyield stress (0.5 GN/m², 70,000 psi) in Fe-3 Si. These are the sites at which stress relief should be initiated on mechanical deformation or annealing. The existence of such regions is not overly surprising. Stresses of 1.45 GN/m² (211,000 psi) have been reported in CuAu crystals [44]. The average stress in the grain was taken as $\Sigma(P_i + P_j + P_k)/n$ where n is the number of determinations within the grain. The result for the as-received crystal was $\bar{P} = -0.083$ GN/m² or $-11,800$ psi, i.e., a compressive stress well below the macroyield stress. For the applied tensile stress of about 500 psi, P was $+0.124$ GN/m² or slightly less than $+18,000$ psi.

Still, the grain must somehow accommodate even small local regions of very high stress. Subgrain boundaries probably form, in order to achieve this accommodation, during the thermal flattening and subsequent steps. Apparently, this local form of atomic rearrangement is enough to accommodate the highly stressed regions with only a minimum of true local plastic deformation. One can conjecture that the one or two potential slip planes with low shear strain may have given up shear energy which contributed to the formation of subgrain boundaries, which then can inhibit further slip on other potential slip systems.

The small applied loads in the study caused rearrangement of the VSD as shown by figures 27-39. The effect of compression is to move the VSD about and to raise the absolute value of the internal strains. Such a procedure cannot be expected to improve the electrical properties of the material but rather to degrade these properties.

The application of a small tensile load tends to line up the VSD in the loading direction. It also tends to smooth out very large strain differences as shown in figures 27-39. This behavior may explain, at least partially, why the electrical properties tend to improve slightly after the application of small tensile loads.

Increasing the tensile stress would probably just increase the magnitude of the strains in the VSD without very much further alteration of their position. In such a case, the magnetic properties would again degrade with increasing load.

Annealing up to 300 °C does no significant good for the electrical properties [4] (see fig. 2). This fact is a further indication that the VSD may move a bit but is not appreciably altered by elevating the temperature. The application of loads at elevated temperatures also does not improve the situation [75].

The core loss for Fe-3 Si material of exactly the type supplied by Dr. Fiedler for this study has been reported as about 10 watts/pound at an induction, B, of 18,000 gauss by the manufacturer [74]. However, Goss oriented Fe-3 Si made in the laboratory using only surface energy to grow the (110) [001] and with no grain boundary impurities such as MnS or Si_3N_4 showed a core loss of about 6 watts per pound at B of 18,000 gauss [74]. This improvement can probably be attributed to less orientation spread around a true (110) [001] and to an overall reduction of the internal stresses in the material occasioned by the absence of the inclusions and the production of fewer misfit grains. Then, the only stresses left would be those due to mechanical anisotropy. These stresses probably cannot be removed owing to their nature. As a guess, core loss can probably be cut by a factor of 2 to 3 by improved processing but not more than this. The main reason for the improvement is that orientation is better and internal stresses are reduced.

The results of this study can be used in an attempt to explain a few of the observations concerning the degradation of electrical properties:

(1) Higher losses at grain boundaries (fig. 2) can result from very high stress concentrations near the boundary (fig. 27a), from grain misorientation across the boundary (fig. 30) and from impurity or misfit stresses at the boundary.

(2) Losses at misaligned (100) [001], grains (fig. 2) can be contributed to by the increased stress at (110) [001] and (100) [001] grains caused by cooling stresses. Of course, the easy magnetization

35

directions change abruptly at such grains which could also contribute to the degradation.

(3) Observations that magnetic domains rearrange upon the application of tensile stresses of a few hundred to several thousand psi have been made [9-11]. Here the VSD rearrange as indicated by figures 27-39 and the domains follow. The so-called transition zone in which a Bitter pattern disappears and then reforms may be a hysteresis in the colloid used to create the pattern. There is no reason to believe that the domains will "disappear" during VSD rearrangement. On increasing loads, beyond a few thousand psi, the magnetic domain pattern does not change drastically [9]. This observation reinforces the notion that an increase in tensile stress merely increases the magnitude of strains in the VSD without altering the position of the VSD drastically.

(4) Compressive stresses can be introduced during cooling from 1200 °C after the texture anneal. Such an occurrence would explain the observation that many magnetic property curves are skewed toward the tensile side [4].

XII. References

[1] Goss, N. P., Trans. ASM **23**, 511 (1935).
[2] Assmus, F., Detert, K., and Ibe, G., Z. Metallk **48**, 344 (1959).
[3] Brailsford, F., and Abu-Eid, Z., Proc. Inst. Elect. Engrs. **110**, 751 (1963).
[4] Brown, D., Holt, C., and Thompson, J. E., Proc. Inst. Elect. Engrs. **112**, 183 (1965).
[5] Boon, C. R., and Thompson, J. E., Proc. Inst. Elect. Engrs. **112**, 2147 (1965).
[6] Imura, T., Weissman, S., and Slade, J. J., Acta Cryst. **8**, 786 (1962).
[7] Stewart, K. H., Proc. Camb. Phil. Soc. **45**, 296 (1949).
[8] Boon, C. R., Holt, C., and Thompson, J. E., Brit. J. Appl. Phys. **14**, 708 (1963).
[9] Dykstra, L. J., and Martuis, U. M., Revs. Mod. Phys. **25**, 146 (1953).
[10] Shur, Ya. S., et al., Phys. Met. and Metallog. (U.S.S.R.) **6(3)**, 158 (1958).
[11] Kirenskii, L. V., Savchenko, M. K., and Rodichev, A. M., Bull. Acad. Sci. U.S.S.R. Phys. Ser. **22**, 1171 (1958).
[12] Morrill, W., Metal Progress **78(3)**, 84 (1960).
[13] Baer, G., Ganz, D., and Thomas, H., J. Appl. Phys. **31**, 235S (1960).
[14] Mullins, W. W., Acta Met. **6**, 414 (1958).
[15] May, J. E., and Turnbull, D., Trans. AIME **212**, 769 (1958).
[16] Sharpe, R. S., Appl. Mater. Res. **4**, 74 (1965).
[17] James, R. W., The optical principles of the diffraction of x-rays, in The Crystalline State, L. Bragg, ed., Vol. II (Bell, London, 1950).
[18] Maier, W., Ann. Physik **40(5)**, 85 (1941).
[19] Lonsdale, K., Phil. Trans. Roy. Soc. London, Ser. **A240**, 219 (1947).
[20] Ellis, T., and Weissmann, S., A.F. Matls. Lab. Technol. Documentary Rept. ML-TDR-64-220 (1964).
[21] Warren, B. E., MIT Physics Dept. course entitled X-ray Diffraction.
[22] Peace, A. G., and Pringle, G. E., Phil. Mag. **53**, 1227 (1952).
[23] Yakowitz, H., J. Appl. Phys. **37**, 4455 (1966).
[24] James, R. W., King, G., and Horrocks, H., Proc. Roy. Soc. (London) **A153**, 230 (1935).
[25] Frazer, J. Z., and Arrhenius, G., in Optique des Rayons X et Microanalyse (R. Castaing, P. Deschamps, and J. Philibert, eds.), p. 516. Editions Tecniq, Paris, 1966.
[26] Potts, H. R., and Pearson, G. L., J. Appl. Phys. **37**, 2098 (1966).
[27] Witt, F., private communication (1966).
[28] Morris, W. G., S. M. Thesis, MIT (1963).
[29] Hanneman, R. E., Ogilvie, R. E., and Modrzejewski, A., J. Appl. Phys. **33**, 1429 (1932).
[30] Potts, H. R., Stanford Electron. Lab. Rept. SU-SEL-64-075 (1964).
[31] Kramers, H. A., Phil. Mag. **(6)46**, 836 (1923).
[32] Stainer, H. M., U.S. Bur. Mines Inform. Circ. 8166 (1963).
[33] Ellis, T., Nanni, L. F., Shrier, A., Weissmann, S., Padawer, G. E., and Hosokawa, N., J. Appl. Phys. **35**, 3364 (1965).
[34] Yakowitz, H., and Vieth, D. L., J. Res. Natl. Bur. Stand. **C69**, 213 (1965).
[35] Warren, B. E., Progr. Metal. Phys. **8**, 147 (1959).
[36] Kossel, W., Ann Physik **26**, 533 (1936).
[37] Gielen, P., Yakowitz, H., Ganow, D., and Ogilvie, R. E., J. Appl. Phys. **36**, 773 (1965).
[38] Mackay, K. J. H., in Optique des Rayons X et Microanalyse (R. Castaing, P. Deschamps, and J. Philibert, eds.), p. 544, Hermann, Paris, 1966.
[39] Morris, W. G., Gen. Elect. Res. Develop. Ctr. Rept. 66-C-217, 1966 (J. Appl. Phys. **39**, 1813 (1968)).
[40] Hald, A., Statistical Theory with Engineering Applications, Wiley (New York) 1962, Chapter 20.
[41] Bearden, J. A., Henins, A., Marzolf, J. G., Sauder, W. C., and Thomsen, J. S., Phys. Rev. **135**, A899 (1964). (See also Bearden, J. A., U.S. AEC Rept. NYO 10586 (1964).)
[42] Ku, H. H., private communication (1969).
[43] Novozhilov, V. V., Theory of Elasticity, Israel Program for Scientific Translations, available from U.S. Dept. Com. as OTS 61-11401.
[44] Slade, J. J., Jr., Weissmann, S., Nakajima, K., and Hirabayashi, M., J. Appl. Phys. **35**, 3373 (1965).
[45] Weissmann, S., et al., U.S.A.F. Materials Lab. Technol. Documentary Rept. ML-IDR-64-220 Parts I-IV (1964-1968).
[46] Cullity, B. D., Elements of X-ray Diffraction, Addison-Wesley, Reading, Massachusetts. (1956).
[47] Rutherford, E., and Andrade, E. N. da C., Phil. Mag. **(6)28**, 263 (1914).
[48] Seemann, H., Ann. Phys. **53**, 461 (1917).
[49] Gerlach, W., Physik, Zeitschr. **22**, 557 (1921).
[50] Linnik, W., Nature (London) **124**, 946 (1929).
[51] Kossel, W., Ergebn. exakt. Naturw. **16**, 295 (1937).
[52] Borrmann, G., Ann. Phys. **27**, 669 (1936).
[53] Castaing, R., Thesis to University of Paris (1951).
[54] Vieth, D. L., and Yakowitz, H., J. Res. Nat. Bur. Stand. (U.S.), **71C** (Eng. and instr.), 313 (1967).
[55] Vieth, D. L., and Yakowitz, H., Rev. Sci. Instr. **39**, 1929 (1968).
[56] Yakowitz, H., Fiori, C. E., and Michaelis, R. E., Nat. Bur. Stand. (U.S.), Spec. Publ. 260-22, 30 pages (Feb. 1971).
[57] Lang, A. R., Advances in X-ray Analysis **10**, 91 (1967).
[58] Ullrich, H. J., Acta Cryst **19**, Suppl. A235 (1966).
[59] Sears, F. W., and Zemansky, M. W., University Physics (2nd ed.) Addison-Wesley, Cambridge, Mass. (1955), p. 264.
[60] Newman, B., Glass, H., and Weissmann, S., A.F. Materials Lab. Technol. Documentary Rept. ML-TDR-64-220 (part IV), 1967.

[61] Moore, G. A., and Shives, T. R., in Metals Handbook (Vol. I), American Society for Metals (1961), p. 1206.

[62] Varga, O. H., Stress-Strain Behavior of Elastic Materials (Inter-science, New York, 1966).

[63] Suits, J. C., and Chalmers, B., Acta Met. **9**, 854 (1961).

[64] Worthington, P. J., and Smith, E., Acta. Met. **12**, 1277 (1964).

[65] Worthington, P. J., Acta. Met. **14**, 1015 (1966).

[66] Dunn, C. G., and McHargue, J. Appl. Phys. **31**, 1767 (1960).

[67] Dunn, C. G., and Walter, J. F., in Recrystallization, Grain Growth and Textures (H. Margolin, ed.) ASM (1966), p. 461.

[68] Hu, H., in Recovery and Recrystallization of Metals (*L.* Himmel, ed.), Gordon and Breach (New York) 1963, p. 311.

[69] Gordon, P., in Energetics in Metallurgical Phenomena (Vol. I) (W. M. Mueller, ed.) Gordon and Breach (New York) 1965, p. 205.

[70] Vobrob'yev, G. M., and Shmyrev, I. P., Fiz. Metall. i. Metallovedne **22** (2) 314 (1966).

[71] Walter, J. L., and Dunn, C. G., Trans. Met. Soc. AIME **218**, 1033 (1960).

[72] Fiedler, H. C., Trans. Met. Soc. AIME **230**, 95 (1964).

[73] DeWit, R., Private Communication (1970).

[74] Walter, J. R., J. Appl. Phys. **36**, 1213 (1965).

[75] Gell, M., and Worthington, P. J., Acta Met. **14**, 1265 (1966).

[76] Kirby, R. K., Private Communication (1970).

[77] Hirth, J. P., and Lothe, J., Theory of Dislocations, McGraw-Hill (New York) 1968, p. 53.

[78] Aust, K. T., and Dunn, C. G., J. Metals **9**, 472 (1957).

[79] Roessler, B., Kramer, J. J., and Kurijama, M., Phys. Stat. Sol. **11**, 117 (1965).

XIII. Tables

TABLE I. *Reliability of Cauchy strains using data from 20 planes of a tungsten crystal compressed 0.2 percent* [16]

Cauchy strain (values in %)	No as- sumed error	$s'_{(\epsilon)}$ (eq. 45)	RND 1*	RND 2*	RND 3*	RND 4*	Mean of RND (1-4)	Range of RND (1-4)	s_{RND}	$s_{(\epsilon_{ij})} = [(s'\ \epsilon)^2 + s^2_{RND}]^{1/2}$	$\dfrac{(t_{14})s(\epsilon_{ij})}{\sqrt{20}}$ $(=0.48s\,\epsilon_{ij})$	Probable error $(=0.155s(\epsilon_{ij}))$
$\langle \epsilon_{11} \rangle$	0.077	0.059	0.096	0.050	0.073	0.090	0.077	0.046	0.023	0.063	0.030	0.010
$\langle \epsilon_{22} \rangle$	−0.137	.074	−0.154	−0.116	−0.120	−0.166	−0.139	.050	.025	.078	.037	.012
$\langle \epsilon_{33} \rangle$	− .053	.054	− .042	.065	.060	.037	.051	.028	.014	.056	.027	.009
$\langle \epsilon_{23} \rangle$	.105	.098	.092	.121	.068	.086	.092	.053	.027	.102	.041	.016
$\langle \epsilon_{31} \rangle$	0.044	.073	0.046	0.037	0.053	0.044	0.045	.016	.008	.073	.035	.011
$\langle \epsilon_{12} \rangle$	.0026	.105	.015	.057	−0.016	.057	.028	.073	.037	.111	.053	.017

*All strain, S, values incremented by ± 0.03. A random numbers scheme was used to assign positive or negative error values in the best of 20 S values. Range of $|S|$ is 0.001 to 0.189 percent. Range of θ: $65.8° \leqslant \theta \leqslant 40.2°$. Thus, ΔS of 0.03 percent represents a reasonable value as indicated by eq (43).

TABLE II. *Reliability of principal strains in a tungsten crystal trained 0.2 percent* [16]

	$\langle \epsilon_{ij} \rangle \pm 0$	$\langle \epsilon_{ij} \rangle + w^{95}_{\langle \epsilon \rangle}$	$\langle \epsilon_{ij} \rangle - w^{95}_{\langle \epsilon \rangle}$
S_1	−0.031	−0.039	−0.019
S_2	0.081	0.116	0.052
S_3	−0.163	−0.223	−0.113

	$\langle \epsilon_{ij} \rangle + w^{50}_{\langle \epsilon \rangle}$	$\langle \epsilon_{ij} \rangle - w^{50}_{\langle \epsilon \rangle}$	Laced $w^{95}_{\langle \epsilon \rangle}$ +−+−+−	Laced $w^{95}_{\langle \epsilon \rangle}$ −+−+−+
S_1	−0.034	−0.028	−0.018	−0.045
S_2	0.092	0.070	0.069	0.093
S_3	−0.182	−0.145	−0.178	−0.148

TABLE III. *Microprobe data for Fe–3 Si analysis*

Fe (counts)	C_{Fe}	Si (counts)	C_{Si}	$t(s)$	Fe (counts)	C_{Fe}	Si (counts)	C_{Si}	$t(s)$
216115	0.992	22927	0.0326	41.3	206256	.953	22513	.0320	41.3
212275	.977	....		41.3	212228	.976	22291	.0317	41.8
215074	.988	22788	.0324	41.2	207371	.957	22228	.0316	41.8
216234	.992	22703	.0322	41.3	206702	.955	22755	.0324	41.5
210210	.968	21499	.0305	41.0	210226	.969	21935	.0312	41.6
211997	.976	22713	.0322	41.2	209137	.964	22447	.0319	41.7
211372	.973	21416	.0304	41.3	213573	.982	22980	.0327	42.2
210084	.968	22515	.0320	41.5	205611	.950	21324	.0303	42.5
206382	.953	22744	.0323	41.6	207108	.956	22437	.0319	42.8
212985	.979	21219	.0301	41.9	210081	.968	22636	.0322	43.1
209716	.966	21384	.0304	42.2	211739	.975	22530	.0320	43.5
206348	.953	20508	.0291	42.4	211386	.973	21050	.0299	40.4
209755	.967	21035	.0299	40.8	205842	.951	21854	.0311	41.2
209723	.967	21354	.0303	41.0	212230	.976	22166	.0315	41.6
208201	.960	22198	.0315	41.4	209202	.964	21529	.0306	41.8
208285	.961	21998	.0313	41.6	204468	.946	20684	.0294	42.3
214115	.984	23095	.0328	41.8	216706	.994	21713	.0309	43.6
211937	.975	21199	.0301	42.0	210313	.969	22259	.0316	39.9
208628	.962	22202	.0315	42.1	209086	.964	22201	.0316	40.0
213955	.983	22759	.0324	42.4	216765	.994	22258	.0316	40.1
211260	.973	22561	.0321	42.6	212540	.978	21598	.0307	40.2
212213	.976	22157	.0315	43.0	213605	.982	22128	.0315	40.7
211931	.975	22619	.0321	41.3	206780	.955	22565	.0321	40.7
211982	.975	22703	.0323	41.5	215698	.990	22067	.0314	40.9
211443	.973	22629	.0322	41.7	209428	.965	22134	.0315	40.4
210691	.970	22665	.0322	41.9	209135	.964	22313	.0303	40.2
210072	.968	22543	.0321	42.2	207478	.958	21688	.0308	40.7
210686	.970	22496	.0320	42.4	206134	.952	21521	.0306	40.0
209810	.967	22413	.0318	42.8	206947	.955	21504	.0306	40.3
209473	.966	22320	.0317	43.1	205625	.950	21805	.0310	40.8
214518	.986	21982	.0312	40.0	207452	.957	21897	.0311	41.8
209599	.966	21988	.0312	40.3	209614	.966	21857	.0311	41.4
210564	.970	22995	.0327	40.5	209987	.968	21291	.0303	42.1
210121	.968	22322	.0317	41.4	207547	.958	21370	.0304	41.9
212068	.976	22409	.0319	41.4	209005	.964	21806	.0310	42.6
213989	.983	22778	.0324	41.4	205929	.951	21153	.0301	41.4
211504	.974	22381	.0318	42.2	21466	.985	22334	.0317	41.6
213177	.980	22595	.0321	42.2	204166	.944	21175	.0301	41.3
212522	.978	22688	.0323	42.3	206124	.952	22352	.0318	41.8
21104	.972	20960	.0298	43.3	205783	.951	22565	.0321	41.6
216309	.993	22781	.0324	40.9	212188	.976	22314	.0317	42.3
210884	.971	21209	.0301	40.7	210666	.970	23116	.0329	42.4
210161	.968	20329	.0289	40.7	208025	.960	23113	.0329	42.5
212217	.976	21842	.0310	41.4	207776	.959	22548	.0321	....
210831	.971	22471	.0319	39.7	206087	.952	21957	.0312	40.0
207499	.958	22415	.0319	39.7	213234	.980	21872	.0311	40.2
209512	.966	21673	.0308	40.2	212612	.978	22612	.0321	41.1
210735	.971	22027	.0313	40.5	205595	.950	21337	.0313	41.1
208406	.961	22323	.0317	40.9	215739	.990	22150	.0315	41.2
207524	.958	22517	.0320	42.2	208509	.962	21884	.0311	41.6
209406	.965	21767	.0309	42.1	209185	.964	22186	.0315	41.4
213762	.983	22054	.0313	41.6	208968	.964	22319	.0317	41.5
212558	.978	22530	.0320	41.4	209528	.966	21798	.0310	42.1

TABLE IV.   *Results for standards used in microprobe analysis*

Pure Si (counts)	t(s)	
756108	42.8	$\tau = 2.3\mu$ s
757647	44.8	
755798	43.7	

Si on Al (counts)	Si BKG (counts)	Si pure (corrected counts)
16198	10748	776189
9390		
6656		

Pure Fe (counts)		Fe pure (corrected counts)
218640		219009
220612		
215942		

Fe on Ni (counts)		
1919		
1931		

41

TABLE V

RESULTS FOR FE-3SI SAMPLE ZX-1

[HKL]= 2   1   1   PCT.STRAIN= 9.44531 E-2
LAMBDA= 1.93597 A   Z= 10.53 CM.
DATA PTS.= 11   D= 1.16979 A

D= 1.16979 PLUS OR MINUS SIGMA= 2.72958 E-4   A
MEAN VALUE OF D= 1.16979 A

STD. DEV. OF FIT FOR U,V,W= 2.78012 E-3
A SHOULD=0;MIN. A= 6.18327 E-5

U=-.578516 PLUS OR MINUS SIGMA= 2.09551 E-3
V= .315788 PLUS OR MINUS SIGMA= 1.03469 E-3
W= 1.01292 PLUS OR MINUS SIGMA= 8.95227 E-5

DIRECTION COSINES ARE:
L1=-.478715   L2= .261311   L3= .838182
[L1↑2+L2↑2+L3↑2]= 1.

SIN THETA= .827487   THETA= 55.8415 DEGREES

42

TABLE VI. *Lattice spacing, d, and lattice parameter, a_0, in Fe-3 Si*

Pattern / Line	220	211	12$\bar{1}$	121	21$\bar{1}$	11$\bar{2}$	112	200	020
Reference	1.01205	1.16487	1.15868	1.16998	1.16410	1.15568	1.16403	1.42904	1.43168
U- 0	1.01177	1.16562	1.16859	1.16676	1.16511	....	1.16731	....	1.43028
U- 1	1.01168	1.1664	1.16654	1.16662	1.16822	....	1.1703	1.42719	1.43018
U- 2	1.01196	1.16812	1.16396	1.16609	1.16852	....	1.16398	1.42685	1.43161
U- 3	1.0110	....	1.1688	1.16503	....	1.1544	1.19541	1.43078	1.4287
U- 4	1.01195	1.16656	1.16608	1.1684	1.16443	....	1.17575	1.42393	1.43149
U- 5	1.01177	1.16753	1.16693	1.16986	1.16402	....	1.1663	1.42642	1.43152
U- 6	1.01212	1.16088	....	1.16641	1.16585	1.15829	....	1.42657	1.42404
U- 7	1.01193	1.1669	1.1658	....	1.1641	1.16086	1.16904	1.4238	1.43377
U- 8	1.01187	1.16806	....	1.16669	1.16777	1.16588	1.1719	1.42453	1.42657
U- 9	1.01174	1.1683	1.16808	1.16713	1.16533	1.17717	1.17774	....	1.42745
U-10	1.01194	1.16758	....	1.16789	1.16433	....	1.16732	1.43271	1.42196
U-11	1.01186	1.16665	....	1.1678	1.16757	....	1.16397	1.43008	1.42793
U-12	1.01201	1.16645	1.16716	1.16834	1.16639	1.1632	1.15934	1.42546	1.43077
U-13	1.01186	1.1673	1.16446	1.16621	1.16748	....	....	1.42944	1.43106
U-14	1.0112	1.16308	1.1603	1.17406	1.15817	....	1.15653	1.41712	1.43605
U-15	1.01174	1.16618	1.16686	1.16629	1.16889	1.1667	1.16734	1.42569	1.41928

d and a_0 in Å

Pattern / Line	10$\bar{1}$	011	01$\bar{1}$	101	a_0
Reference	2.00269	2.01062	2.02063	2.0102	2.86154
U- 0	2.00429	2.0113	2.02321	2.00757	2.86221
U- 1	2.01691	2.01603	2.02007	2.01356	2.86223
U- 2	2.0171	2.01362	2.02055	2.01429	2.86221
U- 3	2.00658	2.01111	2.02172	....	2.86273
U- 4	2.011	2.02248	2.02434	2.01561	2.86457
U- 5	2.01076	2.01553	2.00058	2.02162	2.86246
U- 6	....	2.00538	2.02131	2.00546	2.86251
U- 7	2.01006	2.01698	2.02216	2.01521	2.86077
U- 8	2.01417	2.02043	....	2.02177	2.86194
U- 9	2.01065	....	2.01792	2.01975	2.86923
U-10	2.01575	....	....	....	2.86199
U-11	2.02032	2.02055	2.0227	2.01715	2.86081
U-12	....	2.02132	....	2.0162	2.86154
U-13	2.01046	2.01107	2.01304	2.01524	2.86258
U-14	....	....	2.00407	2.01341	2.85825
U-15	2.01268	2.02641	2.02045	2.00976	2.86016

TABLE VII. *Lattice strains in Fe-3 Si (strains in percent)*

Pattern / Line	U-0	U-1	U-2	U-3	U-4	U-5	U-6	U-7	U-8
220	−0.028	−0.037	−0.0089	−0.104	−0.0099	−0.034	0.007	−0.012	−0.018
211	0.0644	0.131	0.279	....	0.145	−.099	−0.343	0.174	0.274
$12\bar{1}$	−0.0081	−0.183	−0.404	0.010	−0.223	−.150	....	−0.246	....
121	−.275	−.287	−.332	−0.423	−.135	0.101	−.305	....	−0.281
$21\bar{1}$	0.087	0.354	0.380	....	0.0283	−0.399	0.150	0	0.315
$11\bar{2}$	....	....	....	−.111	....	....	.226	0.448	−0.240
112	−0.117	.139	−0.403	−.397	.605	−.204	−0.231	0.0305	0.275
200	....	−0.129	−.153	0.122	−0.358	−.344	−.166	−0.367	−0.316
020	−.098	−.105	−.0041	−0.208	−.0133	0.0125	−.535	0.146	−0.357
$10\bar{1}$	0.080	0.710	0.720	0.194	0.420	−0.665	....	0.368	0.573
011	.034	.269	.149	.0244	.590	−.430	−.261	0.316	0.488
$01\bar{1}$	.128	−0.028	.004	.0539	.184	....	0.034	0.0751	....
101	−0.131	0.167	.203	....	.269	−.129	−0.236	0.249	0.576

	U-9	U-10	U-11	U-12	U-13	U-14	U-15
220	−0.031	−0.011	−0.019	0.004	−0.019	−0.084	−0.0036
211	0.294	0.233	0.153	.136	0.209	−.154	−.214
$12\bar{1}$	−0.052	....	....	−0.130	−0.362	−.717	−.156
121	−.244	−0.179	−0.076	−.140	−.322	0.349	−.205
$21\bar{1}$	0.106	0.0198	−.095	0.197	0.290	−0.509	0.018
$11\bar{2}$	.726	....	....	....	....	−0.170	
112	.775	−0.117	−.403	.056	....	0.0735	....
200	....	0.257	0.073	−0.251	.028	−0.834	−.234
020	−0.295	−0.679	−0.262	−.064	−0.043	0.305	−.866
$10\bar{1}$	0.397	0.652	−.193	....	0.388	....	−.570
011	....	....	−.181	0.532	.022	....	0.108
$01\bar{1}$	−0.134	....	−.075	....	−0.376	−0.820	−0.186
101	0.475	....	−.349	.298	0.251	0.160	−.715

	C-1	C-2	C-3	C-4	C-5	C-6	C-7
220	−0.043	−0.038	−0.015	−0.017	−0.093	−0.028	−0.042
211	0.0009	0.159	0.149	0.132	−.0009	0.102	0.0944
$12\bar{1}$	−0.689	−0.249	−0.300	−0.204	−.220	−0.200	−0.302
121	−.320	−.280	−.195	−.215	−.312	−.262	−.347
$21\bar{1}$	0.351	0.264	0.326	0.155	0.457	0.067	·0.316
$11\bar{2}$	−0.078	−0.361	.216	.081	....	.020	−0.111
112	....	....	−0.273	....			
200	−.0434	−.041	0.088	.034	−0.332	−0.219	−.078
020	−.177	−.648	−0.396	−0.203	−.566	−.131	−.281
$10\bar{1}$	0.373	0.0664	0.153	....	....	0.529	0.391
011	.735	....	−0.243	0.635	−.402	.737	.659
$01\bar{1}$	−0.500	−0.738	−.486	−0.816	0.301	−0.405	−0.440
101	0.262	−.159	0.448	....	−0.564	....	0.166

TABLE VII. *Lattice strains in Fe-3 Si (strains in percent)* — Continued

	C–8	C–9	C–10	C–11	C–12	C–13
220	−0.021	−0.020	−0.018	−0.011	−0.030	−0.047
211	0.0807	0.151	0.147	0.194	0.091	0.051
12$\bar{1}$	−0.205	−0.216	−0.288	−0.152	−0.353	−0.262
121	−.213	−.220	−.138	−.258	−.319	−.337
21$\bar{1}$	0.293	0.295	0.275	0.294	0.313	0.115
11$\bar{2}$	−0.093	.142	.119	.185	.019	.483
112	....	−0.418	.281	....	−0.324	....
200	−.0112	0.0119	−0.332	−0.023	−.148	−0.0896
020	−.457	−0.263	−.268	−.182	−.452	−.368
10$\bar{1}$	0.164	....		0.320	0.425	0.692
011	.482	0.756	....	−0.278	....	.306
01$\bar{1}$	−0.334	−0.501	−.191	−.094	−0.357	−0.419
101	0.395	....	0.464	....	0.456	0.0925

	T–1	T–2	T–3	T–4	T–5	T–6	T–7
220	−0.026	−0.039	−0.030	−0.051	−0.021	−0.054	−0.065
211	0.122	0.191	0.132	0.124	0.202	−.065	0.118
12$\bar{1}$	−0.261	−0.264	−0.248	−0.279	−0.362	−.241	−0.264
121	−.203	−.260	−.283	−.220	−.203	−0.329	−.354
21$\bar{1}$	0.179	0.120	0.109	0.263	0.229	0.113	0.157
11$\bar{2}$	−0.155	−0.199	.407	−0.415	−0.349	....	
112	....	0.432	....				
200	....	−0.342	....		0.196	.027	−0.072
020	−.205	−.325	−0.805	−0.434	−0.191	−0.527	−.562
10$\bar{1}$	0.516	0.610	0.368	0.514	0.750	0.343	0.635
011	.377	.173	.319	.159	.045	.139	.239
01$\bar{1}$	−0.0965	−0.092	−0.148	−0.229	−0.448	−0.554	−0.113
101	0.205	0.271	0.199	0.054	0.534	0.263	0.202

	T–8	T–9	T–10	Y–1	Y–2	Y–3
220	−0.049	−0.024	−0.0198	−0.024	−0.038	−0.038
211	0.091	0.239	0.110	0.209	0.101	0.102
12$\bar{1}$	−0.456	.287	−0.201	−0.252	−0.329	−0.232
21$\bar{1}$	0.101	.176	....	0.226	0.206	0.276
11$\bar{2}$	.019	−0.017	−.033	.330	.0671	.080
112	−0.324	0.125	−.397	−0.683	−0.508	....
200	−.148	....	0.371	....	−.105	.052
020	−.452	−0.198	.058	−.380	−.368	−0.413
10$\bar{1}$	0.520	0.583	.266	0.680	0.809	0.432
011	−0.181	.375	.41	.372	.462	.527
01$\bar{1}$	....	−0.176	−0.414	−0.143	−0.110	−0.343
101	0.071	0.515	0.616	0.280	....	0.204

Table VIII. *Cauchy strains and their standard errors (all values in percent)*

	U–0	U–1	U–2	U–4	U–5	U–7	U–8	U–9	U–10
$\langle\epsilon\rangle_{11}$	0.2479	0.1250	0.3540	−0.1860	−0.3601	−0.1144	0.1108	0.0742	0.3237
s_{11}	.1388	+0.1930	.3023	0.1960	0.05055	0.2487	.3112	.2891	−0.2014
$\langle\epsilon\rangle_{22}$	−0.1111	−0.3512	−0.3400	−0.2937	.0262	−0.0884	−0.5925	−0.4825	−0.7012
s_{22}	0.08871	0.1973	0.3091	0.1960	.0513	0.2621	0.3465	0.1901	0.2242
$\langle\epsilon\rangle_{33}$	−0.02725	.3826	−0.3786	.9194	−0.5638	.3926	.1313	1.079	−0.3875
s_{33}	0.1049	.2522	0.3950	.2478	0.0675	.2144	.2729	0.1534	0.3487
$\langle\epsilon\rangle_{23}$	−0.2943	−0.0410	.2965	.1792	.0666	.1540	.5576	−0.1942	.8700
s_{23}	0.1520	0.4021	.6298	.3697	.1063	.5348	.7729	0.3429	.8490
$\langle\epsilon\rangle_{31}$	.0141	−0.3241	−0.4303	−0.0562	.4722	−0.1951	−0.1346	.2477	−0.3196
s_{31}	.1520	0.3536	0.5539	0.3697	.0987	0.4741	0.6513	.3336	0.5191
	.093	.917	.777	.152	4.78	.412	.207	.743	.616
$\langle\epsilon\rangle_{12}$	−0.2225	.1269	.03742	.2443	0.2780	.1042	.4442	.2215	.3025
s_{12}	0.2262	.3880	.6078	.3885	.1016	.4906	.6210	.4834	.3836

	U–11	U–12	U–13	U–14	U–15	C–1	C–2	C–3	C–4
$\langle\epsilon\rangle_{11}$	0.1186	0.012	0.3315	−0.5731	−0.3799	0.2835	0.1195	0.2831	0.1636
s_{11}	.1276	.2095	.2247	0.2529	0.1588	.2640	.1356	.1616	.2022
$\langle\epsilon\rangle_{22}$	−0.1912	−0.2196	−0.3468	.084	.6761	−0.4788	−0.6894	−0.5107	−0.3112
s_{22}	0.1290	0.2095	0.2247	.2536	.1588	0.2640	0.1375	0.1616	0.1965
$\langle\epsilon\rangle_{33}$	0.6150	.2796	.0354	−0.5032	−0.3101	.053	−0.4579	−0.014	−0.045
s_{33}	0.1686	.2891	.04706	0.3411	0.2008	.3339	0.1810	0.1419	0.2645
$\langle\epsilon\rangle_{23}$	.052	.1294	.2192	.014	.1455	.9512	.1605	.1124	.5210
s_{23}	.3044	.4475	.4097	.5307	.2996	.4981	.2852	.2992	.4062
$\langle\epsilon\rangle_{31}$	.1821	−0.2022	−0.2299	.041	−0.3479	−0.8013	−0.1855	−0.4646	−0.4368
s_{31}	.2340	0.4475	0.4097	.05656	0.2996	0.4981	0.2648	0.2992	0.4423
$\langle\epsilon\rangle_{12}$	.1129	.2063	−0.0798	.2003	1.047	−0.9986	−0.6634	.2240	.1083
s_{12}	.2438	.4203	0.4318	.5107	0.3148	0.5234	0.2725	0.3232	.3994

	C–5	C–6	C–7	C–8	C–9	C–11	C–12	C–13	T–4
$\langle\epsilon\rangle_{11}$	−0.1483	−0.0580	0.2070	0.1488	0.2195	0.1814	0.1487	0.1183	0.5139
s_{11}	0.2261	0.2625	.2097	.1593	.2530	.1439	.1902	.1509	.0915
$\langle\epsilon\rangle_{11}$	−0.7497	−0.1413	−0.4319	−0.4680	−0.3338	−0.3834	−0.6138	−0.5172	−0.3858
s_{22}	0.2261	0.2589	0.2097	0.1593	0.2443	0.1420	0.1939	0.1509	0.0585
$\langle\epsilon\rangle_{33}$	.4878	.7588	−0.027	.028	.1428	.1698	−0.1484	.5712	−0.059
s_{33}	.5191	.3456	0.2651	.2014	.2200	.1895	0.1694	0.1908	0.0692
$\langle\epsilon\rangle_{23}$	.0355	−0.04119	.4407	.3123	.4176	.1114	.020	.2185	.3401
s_{23}	.4309	0.5055	.3956	.3005	.5037	.2772	.3811	.2847	.1002
$\langle\epsilon\rangle_{31}$	−0.7075	−0.1690	−0.4862	−0.2866	−0.8418	−0.1099	−0.3416	−0.4279	−0.3808
s_{31}	0.4546	0.5446	0.3956	0.3005	0.5309	0.2986	0.3708	0.2847	0.1002
$\langle\epsilon\rangle_{12}$	.7670	.1992	.1122	.2961	.1312	.2027	.4133	.1112	−0.2421
s_{12}	.4365	.5201	.4156	.3157	.5016	.2852	.3850	.2992	.1492

	T-5	T-7	T-9	T-10	Y-1	U-3	C-10	T-1	T-2
$\langle\epsilon\rangle_{11}$	0.462	0.175	0.774	0.365	0.746	0.143	−0.053	0.653	−0.050
s_{11}	.178	.206	.188	.074	.478	.140	0.197	.162	0.219
$\langle\epsilon\rangle_{22}$	−0.301	−0.304	−0.209	.132	−0.243	−0.152	−0.492	−0.145	−0.504
s_{22}	0.178	0.206	0.119	.075	0.308	0.123	0.197	0.103	0.219
$\langle\epsilon\rangle_{33}$	−0.217	.301	.123	−0.242	.179	−0.284	.338	−0.108	.263
s_{33}	0.225	.432	.094	.098	.251	0.106	.175	0.122	.192
$\langle\epsilon\rangle_{23}$	.453	.096	.197	.659	−0.141	−0.312	.283	.315	.328
s_{23}	.336	.376	.234	.178	0.525	0.287	.414	.177	.405
$\langle\epsilon\rangle_{31}$	−0.181	−0.220	−0.038	−0.100	−0.558	−0.255	−0.135	−0.250	.126
s_{31}	0.336	0.376	0.206	0.136	0.525	0.345	0.414	0.177	.405
$\langle\epsilon\rangle_{12}$	−0.218	−0.125	−0.753	−0.521	−0.571	−0.227	.502	−0.619	.425
s_{12}	0.353	0.397	0.305	0.142	0.790	0.243	.400	0.264	.438

	T-3	T-6	T-8	Y-2	Y-3	U-6
$\langle\epsilon\rangle_{11}$	−0.100	0.056	0.079	0.146	0.202	−0.246
s_{11}	0.171	.120	.173	.237	.123	0.134
$\langle\epsilon\rangle_{22}$	−0.821	−0.556	−0.626	−0.411	−0.506	−0.460
s_{22}	0.110	0.120	0.176	0.233	0.123	0.183
$\langle\epsilon\rangle_{33}$	.642	.125	−0.155	−0.206	.238	.015
s_{33}	.130	.252	0.154	0.207	.155	.127
$\langle\epsilon\rangle_{23}$	.118	.172	.240	.192	.513	−0.235
s_{23}	.188	.219	.346	.454	.231	0.224
$\langle\epsilon\rangle_{31}$	−0.113	−0.350	−0.296	−0.707	−0.462	−0.520
s_{31}	0.188	0.219	0.337	0.467	0.231	0.262
$\langle\epsilon\rangle_{12}$	.740	.282	.357	.190	.164	.622
s_{12}	.279	.231	.351	.473	.243	.281

Pattern	S_1	Maximum credible error on S_1	S_2	Maximum credible error on S_2	S_3	Maximum credible error on S_3
U– 0	0.288	0.066	0.059	0.045	−0.237	0.040
U– 1	.461	.119	0.058	.078	0.362	.085
U– 2	.413	.106	−0.233	.313	−0.544	.302
U– 3	.195	.065	−.051	.083	−.437	.085
U– 4	.926	.157	0.215	.087	−.330	.111
U– 5	.090	.007	−0.266	.047	−.722	.061
U– 6	.278	.034	−.282	.082	−.687	.094
U– 7	.420	.122	−.048	.077	−.182	.229
U– 8	.227	.404	0.172	.420	−.750	.083
U– 9	1.10	.135	.085	.080	−.513	.093
U–10	0.362	.147	−0.086	.156	−1.04	.187
U–11	.140	.035	−.200	.078	−0.627	.129
U–12	.260	.123	0.021	.100	−.280	.106
U–13	.378	.172	.018	.141	−.376	.157
U–14	.562	.079	−0.678	.311	−.977	.392
U–15	.043	.102	−.304	.094	−1.11	.178
C– 1	.685	.136	−.040	.153	−0.787	.152
C– 2	.243	.040	−.433	.151	−.838	.200
C– 3	.419	.060	−.106	.071	−.542	.097
C– 4	.319	.121	0.012	.133	−.513	.120
C– 5	.661	.130	−0.113	.120	−.958	.190
C– 6	.132	.113	−.045	.157	−.211	.196
C– 7	.366	.099	−.058	.113	−.560	.133
C– 8	.246	.101	0.023	.091	−.561	.093
C– 9	.501	.101	−0.165	.164	−.593	.185
C–10	.364	.116	0.061	.099	−.631	.093
C–11	.251	.151	.121	.118	−.405	.065
C–12	.266	.059	−0.208	.106	−.672	.151
C–13	.662	.085	0.048	.056	−.537	.069
T– 1	.776	.064	−0.077	.062	−.317	.079
T– 2	.329	.098	−.013	.086	−.608	.114
T– 3	.647	.076	0.054	.063	−.981	.070
T– 4	.607	.034	−0.021	.027	−.452	.034
T– 5	.500	.083	−.066	.083	−.490	.109
T– 6	.270	.072	−.037	.056	−.608	.102
T– 7	.372	.204	0.113	.129	−.314	.100
T– 8	.183	.053	−0.214	.105	−.671	.153
T– 9	.905	.088	0.136	.039	−.353	.042
T–10	.599	.257	.099	.112	−.445	.150
Y– 1	.883	.158	−0.137	.166	−.422	.225
Y– 2	.366	.121	−.287	.118	−.550	.152
Y– 3	.471	.133	0.076	.084	−.614	.141

TABLE X. *Direction cosines of principal strain axes after deformation*

Pattern	l_{1i}	l_{2i}	l_{3i}	Pattern	l_{1i}	l_{2i}	l_{3i}
U–0	0.931	−0.323	0.172	U–8	0.135	0.352	0.926
	.320	0.491	−0.810		.956	.199	−0.215
	.177	0.809	0.560		.260	−0.915	0.309
U–1	.436	0.011	−0.900	U–9	.114	−.053	.992
	.888	0.160	0.432		.973	0.207	−0.101
	.149	−0.987	0.060		−0.200	.977	0.075
U–2	−0.963	0.029	0.267	U–10	0.983	.071	−0.168
	−.937	0.058	0.344		.095	.590	0.802
	0.200	−0.587	0.784		.156	−0.804	.574
U–3	−0.956	0.232	0.180	U–11	.977	0.176	.124
	0.085	0.805	−0.587		−0.179	.984	.022
	.280	0.546	0.790		0.118	.044	−0.992
U–4	−0.027	0.071	0.997	U–12	−0.345	.052	0.937
	0.972	0.235	0.009		0.850	.442	.288
	.981	0.194	0.017		.400	−0.895	.197
U–5	.376	0.909	0.182	U–13	−0.933	0.104	.346
	.736	−0.412	0.537		0.360	.232	.903
	−0.563	0.068	0.824		.011	.967	−0.255
U–6	0.578	0.360	−0.733	U–14	.083	.830	0.551
	.543	0.501	0.674		−0.992	.015	.126
	.610	−0.787	0.094		0.097	−0.557	.825
U–7	−0.166	0.131	0.977	U–15	.790	0.547	−0.276
	0.890	0.429	0.156		.102	.327	0.940
	.908	0.267	0.323		.604	−0.770	.202
C–1	−0.691	0.295	0.660	C–8	.855	0.065	−0.515
	0.702	0.491	0.516		.453	.391	0.801
	.172	−0.820	0.546		.253	−0.918	.305
C–2	.941	0.327	−0.087	C–9	−0.823	0.076	.563
	−0.093	0.088	0.958		0.408	.769	.492
	0.338	−0.901	0.272		.395	−0.635	.664
C–3	.877	0.077	−0.475	C–10	−0.074	0.141	.987
	.445	0.243	0.862		0.910	.415	.011
	.182	−0.967	0.178		.408	−0.899	.160
C–4	−0.780	0.183	−0.599	C–11	.755	0.176	−0.632
	0.541	0.583	0.606		.635	.042	0.771
	.244	−0.793	0.559		−0.163	.984	.080
C–5	.441	0.109	−0.891	C–12	0.906	.209	−0.369
	.765	0.473	0.437		.332	.191	0.924
	.469	−0.874	0.125		.263	−0.959	.104
C–6	.497	0.244	−0.833	C–13	−0.359	0.069	.931
	.640	0.545	0.541		0.925	.158	.345
	.586	−0.802	0.115		.122	−0.985	.121
C–7	−0.822	0.097	0.562				
	0.531	0.488	0.692				
	.207	−0.867	0.453				
T–1	−0.920	0.342	0.191	T–9	−0.944	0.325	0.064
	0.333	0.429	0.840		0.118	.151	.981
	.205	0.836	−0.508		.309	.934	−0.181
T–2	.296	0.256	0.920	T–10	−0.740	.611	0.283
	.894	0.265	0.362		0.662	.586	.467
	.337	−0.930	0.150		.120	.533	−0.838
T–3	−0.063	0.024	0.998				
	0.919	0.392	0.049				
	.390	−0.920	0.047				

Pattern	l_{1i}	l_{2i}	l_{3i}	Pattern	l_{1i}	l_{2i}	l_{3i}
T–4	−0.924	0.171	0.341	Y–1	−0.946	.225	0.234
	0.378	0.285	0.881		0.042	−0.629	.776
	.053	0.943	−0.328		.322	0.744	.586
T–5	−0.967	0.182	0.180	Y–2	.853	.040	−0.521
	0.254	0.606	0.754		.335	.723	0.604
	.028	0.774	−0.632		.401	−0.689	.603
T–6	.645	0.030	−0.764	Y–3	−0.615	0.151	.774
	.723	0.299	0.623		0.766	.347	.541
	.247	−0.954	0.171		.186	−0.926	.329
T–7	−0.510	0.108	0.853				
	0.852	−0.068	0.518				
	.114	0.992	−0.057				
T–8	.898	0.198	−0.393				
	.366	0.161	0.917				
	.245	−0.967	0.072				

TABLE XI. *Direction cosines of undeformed fibers*

Pattern	k_{1i}	k_{2i}	k_{3i}	Pattern	k_{1i}	k_{2i}	k_{3i}
U– 0	0.589	−0.386	0.709	U– 8	0.066	0.328	0.942
	.320	0.487	−0.812		.622	.415	.664
	.207	.879	0.429		.243	−0.800	−0.549
U– 1	−0.344	−0.0028	.939	U– 9	.073	−.041	0.996
	−.891	−.159	−0.424		.977	0.201	−0.067
	−.223	−.558	−.799		.021	.704	−.710
U– 2	−.824	0.081	0.560	U–10	−0.765	.140	0.629
	−.906	−0.128	−0.405		−.096	−0.588	−0.803
	0.120	−.933	0.339		0.078	−.894	−.442
U– 3	−0.908	0.109	.405	U–11	.959	0.176	0.223
	0.082	.803	−0.590		.333	−0.364	−0.870
	−0.330	.711	0.621		−0.156	−.070	0.985
U– 4	−.018	.053	.998	U–12	−.307	0.058	0.950
	−.295	.092	.951		−.851	−0.442	−0.285
	−.067	.118	.991		0.314	−.929	−.196
U– 5	0.387	.896	.218	U–13	−.712	0.130	.690
	−0.656	.435	−0.617		−.361	−0.232	−0.903
	−.934	.249	0.255		−.128	−.912	−.391
U– 6	−.540	−0.333	.772	U–14	.068	0.746	0.663
	−.595	−.519	−0.613		.380	.731	−0.567
	−.324	−.472	−.820		.615	.562	−.553
U– 7	−.145	0.114	0.983	U–15	−0.789	−0.545	0.285
	−.407	.325	.854		−.144	−.342	−0.929
	−.260	.206	.943		0.021	−.319	−.947

TABLE XI. *Direction cosines of undeformed fibers*—Continued

Pattern	k_{1i}	k_{2i}	k_{3i}	Pattern	k_{1i}	k_{2i}	k_{3i}
C– 1	−.524	.289	.801	C– 8	−0.752	−0.011	0.659
	−.704	−0.489	−0.515		−.454	−.391	−0.801
	−.061	−.998	−.009		0.113	−.876	−.469
C– 2	−.831	−.245	0.500	C– 9	−0.707	0.104	0.700
	−.021	−.242	−0.970		−.443	−0.740	−0.506
	0.032	−.323	−.946		0.279	−.919	0.279
C– 3	−0.731	−.043	0.682	C–10	−0.839	−.257	.480
	−.451	−.241	−0.860		0.272	−.611	−0.743
	−.182	−.567	−.804		−0.070	0.133	0.989
C– 4	−.683	0.215	0.698	C–11	−.588	−0.156	.794
	−.611	−0.558	−0.562		−.672	−.053	−0.739
	0.183	−.958	0.219		−.189	0.474	−.860
C– 5	−0.349	−.072	.934	C–12	−.833	−0.182	0.522
	−.774	−.473	−0.422		−.350	−.190	−0.917
	−.287	−.494	−.821		−.176	−.273	−.946
C– 6	−.475	−.230	0.850	C–13	−.265	0.065	0.962
	−.645	−.546	−0.534		−.927	−0.157	−0.341
	0.276	−.806	−.523		−.211	−.697	−.685
C– 7	−0.710	0.130	0.692				
	−.534	−0.486	−0.692				
	0.036	−.990	−.138				
T– 1	−0.403	0.217	0.889	T– 8	−.859	−0.185	0.477
	−.332	−0.422	−0.843		−.390	−.163	−0.906
	−.306	−.944	0.126		−.200	−.205	−.958
T– 2	0.251	0.233	.939	T– 9	−.096	0.088	0.991
	.894	.266	−0.361		−.118	−0.148	−0.982
	.408	−0.488	−.771		−.302	−.831	−.467
T– 3	−0.049	0.024	0.998	T–10	−.428	0.541	0.725
	−.922	−0.388	.003		−.665	−0.573	−0.479
	0.014	−.165	−0.986		−.174	−.622	0.764
T– 4	−0.609	0.175	0.774				
	−.378	−0.285	−0.881				
	−.204	−.918	−.340				
T– 5	−.596	0.256	0.761	Y– 1	−.490	0.052	.871
	−.255	−0.603	−0.756		−.052	.612	−0.789
	−.099	−.964	0.245		0.278	.956	0.097
T– 6	−.578	−.013	.816	Y– 2	−0.778	−0.016	.628
	−.725	−.299	−0.621		−.434	−.626	−0.648
	−.104	−.616	−.781		0.055	−.982	−.179
T– 7	−.398	0.092	0.913	Y– 3	−0.485	0.166	0.859
	−.873	.074	−0.483		−.773	−0.343	−0.534
	−.276	−0.537	−.797		0.013	−.953	−.304

TABLE XII. *Angle between undeformed fibers and principal strain axes (θ in degrees)*

Pattern	θ_1	θ_2	θ_3	Pattern	θ_1	θ_2	θ_3
U– 0	37.4	0.65	8.7	T– 1	52.1	179.6	156.3
U– 1	174.3	179.8	61.9	T– 2	3.15	0.69	61.6
U– 2	18.9	45.4	33.1	T– 3	0.79	177.1	83.6
U– 3	15.0	0.37	13.9	T– 4	31.1	179.7	139.9
U– 4	1.3	104.9	91.5	T– 5	40.6	179.7	154.8
U– 5	2.3	173.4	41.2	T– 6	165.4	179.7	64.7
U– 6	176.7	174.0	5.5	T– 7	7.4	177.7	121.2
U– 7	1.4	95.1	82.9	T– 8	174.6	178.5	85.4
U– 8	4.3	57.7	51.3	T– 9	79.5	179.9	141.7
U– 9	2.5	2.0	50.9	T–10	31.6	179	172.7
U–10	148	179.5	61.5				
U–11	5.8	116.0	177.3	Y– 1	47.3	150.4	31.0
U–12	2.3	179.6	23.3	Y– 2	172.4	171.6	53.7
U–13	23.6	73.6	141.6	Y– 3	9.0	179.6	38.4
U–14	8.1	115.9	135.2				
U–15	179.3	177.3	86.2				
C– 1	12.5	179.8	36.6				
C– 2	154.8	172.5	87.5				
C– 3	165.3	68.2	179.6				
C– 4	8.1	175	22.1				
C– 5	173.8	179.1	78.8				
C– 6	178.4	179.5	41.5				
C– 7	10.0	179.5	36.5				
C– 8	169.4	179.6	46.4				
C– 9	10.4	177.3	28.5				
C–10	0.59	149.9	57.2				
C–11	166.6	177.1	64.6				
C–12	170.1	178.7	83.3				
C–13	5.7	179.7	54.7				

TABLE XIII. *Principal stresses* (GN/m^2)

Pattern	P_1	P_2	P_3	ΣP_i
U- 0	0.554	0.206	-0.246	0.513
U- 1	.867	.252	$-.387$	.732
U- 2	.736	.463	$-.722$	.477
U- 3	-0.385	-0.973	-1.07	-2.43
U- 4	2.96	2.05	1.88	6.89
U- 5	-0.807	-1.35	-2.04	-4.20
U- 6	$-.303$	-1.16	-1.77	-3.23
U- 7	1.32	0.960	0.756	3.04
U- 8	-0.022	-0.106	-1.51	-1.64
U- 9	2.38	0.834	-0.076	3.14
U-10	-0.253	-0.936	-2.39	-3.58
U-11	$-.509$	-1.03	-1.68	-3.22
U-12	0.398	0.032	-0.425	0.005
U-13	.598	.048	$-.552$	.094
U-14	-0.187	-1.92	-2.53	-4.64
U-15	-1.37	-1.90	-3.12	-6.39
C- 1	0.894	-0.211	-1.35	-0.666
C- 2	-0.710	-1.74	-2.36	-4.81
C- 3	0.397	-0.402	-1.07	-1.07
C- 4	.294	$-.173$	-0.973	-0.851
C- 5	.575	$-.604$	-1.89	-1.92
C- 6	.071	$-.198$	-0.452	-0.578
C- 7	.293	$-.354$	-1.12	-1.18
C- 8	.069	$-.271$	-1.16	-1.36
C- 9	.493	$-.522$	-1.17	-1.20
C-10	.337	$-.123$	-1.18	-0.966
C-11	.348	0.151	-0.650	$-.151$
C-12	-0.240	-0.962	-1.67	-2.87
C-13	1.19	0.254	-0.638	0.806
T- 1	1.58	.284	$-.081$	1.79
T- 2	0.195	-0.326	-1.23	-1.36
T- 3	.692	$-.211$	-1.79	-1.31
T- 4	1.06	0.109	-0.547	0.627
T- 5	0.702	-0.159	$-.805$	-0.262
T- 6	1.59	$-.451$	-1.32	$-.185$
T- 7	0.749	0.354	-0.296	0.806
T- 8	-0.460	-1.06	-1.76	-3.28
T- 9	2.10	0.930	0.186	3.22
T-10	1.18	.419	-0.410	1.19
Y- 1	1.68	.132	$-.303$	1.51
Y- 2	0.062	-0.933	-1.33	-2.21
Y- 3	.648	0.045	-1.01	-0.314

TABLE XIV. *Stresses in principal strain axes frame* (GN/m^2)

Pattern	σ_{11}	σ_{22}	σ_{33}	σ_{23}	σ_{31}	σ_{12}
U- 0	0.3183	0.5471	−0.2963	−0.0916	+0.02412	−0.1295
U- 1	.1349	.8363	−.1595	0.0160	−0.1109	0.1374
U- 2	.03475	−1.320	0.07104	.1282	0.05607	.1929
U- 3	−0.361	−0.908	−0.989	˙038	.064	.177
U- 4	2.052	1.413	1.427	1.419	.000674	.00635
U- 5	−1.402	−0.9912	−2.266	0.00900	.1371	.2239
U- 6	−0.176	−1.94	−1.35	−0.163	0.270	−0.069
U- 7	0.7371	0.1669	0.2275	.1917	−0.0217	.0605
U- 8	−.2085	−0.230	−1.587	−.3157	−0.1724	0.0725
U- 9	2.0496	0.3697	1.060	0.1634	0.1287	−−0.1410
U-10	−0.6115	−0.6447	−2.714	−0.1731	.2171	−.0723
U-11	−1.189	−.7770	−1.603	−.1195	−0.00358	0.0751
U-12	0.0820	0.3440	−0.4203	−.0690	−.1356	−0.0732
U-13	−0.00323	.5136	−.4064	0.0578	0.1151	0.1479
U-14	0.04022	−3.229	−1.960	−0.00220	−0.0179	.3705
U-15	−2.155	−1.195	−3.74	−.1648	−.1194	.09669
C- 1	−0.3472	1.230	−1.621	−.1380	−0.3287	.2569
C- 2	−.9234	−2.606	−1.819	0.02537	0.1188	−0.3429
C- 3	0.3569	−0.9435	−0.6018	−0.1937	−0.1381	−.1131
C- 4	−0.1661	0.3686	−1.190	0.001664	−.2168	0.1839
C- 5	−.6224	.4803	−1.987	.01792	−.3853	.3790
C- 6	0.0919	−0.5147	−0.2190	−0.0608	0.09721	−0.00461
C- 7	−0.4126	0.3220	−1.218	0.007658	−0.2680	0.1652
C- 8	−.3251	.005791	−1.191	−0.0754	−.2611	−0.04648
C- 9	0.6620	−1.516	−0.4800	0.2060	0.1806	0.1477
C-10	.7899	−0.007786	0.02517	.1211	.2624	.04582
C-11	.0004632	0.3204	−0.4880	.1322	.03306	−0.001875
C-12	−0.3506	−1.667	−1.166	−0.1515	−0.0961	−.2230
C-13	1.088	−0.3353	0.1413	−.1601	−.1885	−.1281
T- 1	1.386	0.6972	.4915	0.1193	−.2191	−.1820
T- 2	1.208	.3539	−0.08226	.3055	0.3802	0.1465
T- 3	−1.365	−0.009197	−3.593	.07854	−1.158	.02039
T- 4	1.014	−.3955	0.07711	.1293	0.2675	.1206
T- 5	0.5160	−.8528	.04669	.04692	.2397	.04141
T- 6	−0.5273	−.7875	−1.074	.1493	.3650	−0.5744
T- 7	0.2247	0.7521	−0.08257	.07775	−0.03871	−.08021
T- 8	−0.2477	−1.348	−.9885	.4373	0.2618	−.56014
T- 9	2.162	0.2932	1.116	.03132	.1212	0.3953
T-10	0.3819	1.437	−0.5002	−0.09249	−0.2242	.2227
Y- 1	1.627	1.437	−.5002	−.05741	0.03738	.3976
Y- 2	−0.3838	0.2410	−.6901	0.1324	−0.6692	.3976
Y- 3	0.4599	.9239	−.5365	.4948	−.2062	−0.2723

54

TABLE XV. *Stresses in cubic axes frame (GN/m²)*

Pattern	σ_{11}	σ_{22}	σ_{33}	σ_{23}	σ_{31}	σ_{12}
U– 0	0.3927	0.0480	0.1284	− 0.3413	0.01632	− 0.2581
U– 1	.3405	− 0.1166	.5878	0.0476	− 0.3760	0.1472
U– 2	− 0.1742	−.8405	− 0.8775	.3439	−.4991	.04341
U– 3	−.180	−.611	−.804	.099	0.401	.111
U– 4	1.323	0.8625	2.027	.2079	− 0.06523	.2833
U– 5	− 1.611	− 1.241	− 1.807	.07724	0.5477	.3225
U– 6	− 1.17	− 1.30	− 1.00	− 0.263	− 0.582	.696
U– 7	0.1577	0.1827	0.6445	0.1786	−.2263	.1209
U– 8	− 0.3877	− 1.063	.3680	− 0.6468	−.1561	.5153
U– 9	1.017	0.4821	1.981	−.2253	0.2873	.2569
U–10	− 0.7669	− 1.752	− 1.451	1.009	− 0.3707	.3509
U–11	−.8557	− 1.153	− 1.560	0.0604	0.2112	.1310
U–12	0.002742	− 0.2092	0.2124	.1501	− 0.2346	.2393
U–13	.3465	−.3047	.06221	.2543	−.2668	− 0.0926
U–14	− 1.949	− 1.318	− 1.882	1.636	0.04706	0.2323
U–15	− 2.291	− 2.575	− 2.224	0.1688	− 0.4036	1.215
C– 1	0.07142	− 0.6604	− 0.1499	1.103	−.9295	− 0.0994
C– 2	− 1.334	− 2.111	− 1.889	0.1862	−.2152	0.7695
C– 3	− 0.05111	− 0.8132	− 0.3242	.1304	−.5389	.2598
C– 4	−.1150	−.5709	−.3157	.6091	−.5067	.1256
C– 5	−.7208	− 1.298	−.1101	.03892	−.8207	.8897
C– 6	−.2302	− 0.3100	−.1015	− 0.04778	−.1960	.2311
C– 7	−.1569	−.7702	−.3818	0.5112	−.5640	.1301
C– 8	−.2676	−.8597	−.3834	.3623	−.3325	.3435
C– 9	−.1518	−.6830	−.4996	.4844	−.9765	.1522
C–10	1.103	0.2951	−.1274	.3925	0.3278	− 0.1571
C–11	0.1287	− 0.4135	0.1176	− 0.1292	− 0.1275	0.2351
C–12	− 0.7223	− 1.454	− 1.008	0.0230	−.3963	.4794
C–13	0.3565	− 0.2536	0.7913	.2535	−.4964	.1290
T– 1	1.069	1.526	.7764	− 0.1253	0.3653	− 0.2899
T– 2	1.208	0.3539	− 0.08226	0.3055	0.3802	0.1465
T– 3	− 0.9430	.6184	− 1.876	.7452	0.1373	− 0.1306
T– 4	0.6823	− 0.1814	0.1946	.3945	− 0.4417	−.2808
T– 5	.3652	−.3680	− 0.2873	.5250	− 0.2100	−.2525
T– 6	− 0.5940	−.5858	− 1.173	.1452	0.1993	−.4060
T– 7	0.4112	−.04851	0.5315	.1112	− 0.2553	−.1445
T– 8	− 0.3666	−.4549	− 1.132	− 0.1797	0.002816	−.3436
T– 9	1.713	0.7693	1.088	0.2289	− 0.0440	−.8739
T–10	0.7087	0.4845	0.1256	.7641	− 0.1159	−.6045
Y– 1	1.172	.2233	.2845	− 0.1638	− 0.6475	−.6626
Y– 2	− 0.2026	− 0.1324	− 0.6666	−.2387	0.2224	−.8202
Y– 3	1.002	0.6153	−.06408	0.2756	0.5955	−.5355

TABLE XVI. *Absolute value of maximum shear strain in selected (kk1) planes (all values in percent)*

Pattern / Line	U–0	U–1	U–2	U–4	U–5	U–7	U–8	U–9	U–10
110	0.4101	0.5164	0.4604	0.1698	0.5426	0.2090	0.7642	0.5578	1.096
101	.4575	.2838	.8015	.8967	.3175	.4310	.7085	1.005	1.093
011	.1695	.7469	.0858	.2291	.7934	.2904	.7564	1.596	0.3137
10$\bar{1}$	.2799	.2647	.9449	.9220	.2525	.3548	.0826	1.047	.8169
1$\bar{1}$0	.4201	.5418	.9808	.0956	.4812	.0788	.8567	0.6385	1.326
01$\bar{1}$	.1871	.8002	.4369	.1783	.6058	.0866	.8313	1.561	0.5403
211	.5208	.2086	.4114	.7079	.3726	.3722	.0850	0.9447	.4492
12$\bar{1}$	.2597	.7451	.8497	.3898	.7077	.2065	.9078	1.130	1.266
121	.2212	.4678	.0489	.4958	.2862	.3305	.8491	1.172	0.7611
21$\bar{1}$	.2742	.5375	.9083	.6783	.7737	.3781	.5079	0.6964	1.099
11$\bar{2}$	.05913	.5933	1.221	.7076	.5934	.2629	.8407	1.119	1.294
112	.3937	.4784	0.1620	.7703	.6322	.4948	.0424	1.235	0.4698
220	.4101	.5164	.4604	.1698	.5426	.2090	.7642	0.5578	1.096
200	.2229	.3482	.5714	.2243	.5478	.2536	.4641	.3325	0.441
020	.3690	.1334	.0622	.0353	.2859	.0545	.7129	.2946	.9210
002	.2946	.3267	.5812	.0241	.4768	.1884	.5733	.3147	.9272

Pattern / Line	U–6	U–11	U–12	U–13	U–14	U–15	U–3	C–1	C–2
110	0.576	0.3517	0.2262	0.6769	1.219	0.3288	0.4988	0.7697	0.7903
101	.378	.7424	.3231	.3130	1.141	.8464	.5725	.6539	.7833
011	.481	.4725	.4390	.4401	0.6113	.6153	.3654	.8224	.4100
10$\bar{1}$	.660	.7350	.2256	.3626	.8586	.6417	.4311	.7684	.7349
1$\bar{1}$0	.295	.3230	.3223	.7505	1.171	.4578	.2986	1.455	.8595
01$\bar{1}$	.937	.4266	.5256	.3968	0.5983	1.052	.1325	0.7340	.6426
211	.391	.4472	.0636	.4478	1.149	.6078	.6087	.2521	.5079
12$\bar{1}$	.776	.5399	.4296	.5932	1.259	.9458	.2277	.9762	1.074
121	.384	.4642	.3057	.4253	0.7626	.6442	.3412	.6381	0.8440
21$\bar{1}$	.457	.6757	.2533	.6593	.5565	.2465	.2757	1.109	.6073
11$\bar{2}$	.314	.5536	.3737	.6548	.4115	.5662	.3209	1.468	.8432
112	.236	.7016	.2386	.1538	1.354	.2662	.2050	0.5902	.5204
220	.576	.3517	.2262	.6767	1.219	.3288	.4988	.7696	.7903
200	.812	.2144	.2896	.2432	0.2044	1.104	.3417	.8059	.6996
020	.665	.1243	.2435	.2332	1.425	1.057	.3863	.9552	.6830
002	.571	.1894	.2402	.3181	1.411	0.3770	.4035	1.244	.2452

Pattern / Line	C–3	C–4	C–5	C–6	C–7	C–8	C–9	C–11	C–12
110	0.8319	0.4705	0.7675	0.1703	0.6400	0.6170	0.6295	0.5862	0.7958
101	.3708	.5024	.8514	.1745	.4556	.4467	.5308	.6559	.4267
011	.5370	.3545	1.238	.2182	.4834	.4963	.5377	.5571	.4682
10$\bar{1}$	.2953	.3626	0.8206	.2164	.3299	.1211	.4151	.2224	.4071
1$\bar{1}$0	.8925	.8299	.7978	.1227	.9152	.7481	1.049	.5649	.8042
01$\bar{1}$	.7046	.4685	1.618	.3391	.5854	.6449	0.7141	.5958	.7082
211	.5224	.2138	0.1444	.8794	.3127	.2043	.6048	.3328	.5019
12$\bar{1}$	.9313	.6572	1.377	.2783	.7879	.7793	.8599	.6556	.9333
121	.5267	.3224	0.7242	.1166	.3968	.5364	.9420	.5312	.6552
21$\bar{1}$	.5887	.5432	.7641	.1691	.6564	.4546	.6560	.3031	.4015
11$\bar{2}$	.7957	.8301	.8559	.1238	.9041	.7031	1.074	.3426	.6766
112	.1004	.2895	.6852	.1239	.1706	.3310	0.4099	.3897	.2350
220	.8319	.4705	.7675	.1703	.6397	.6170	.6295	.5862	.7958
200	.5158	.4312	1.044	.2612	.4988	.4120	.8520	.2306	.5362
020	.2506	.5457	0.7678	.2034	.4548	.4304	.4377	.2314	.4138
002	.4780	.6977	.7084	.1740	.6562	.4238	.9397	.1565	.3422

TABLE XVI. *Absolute value of maximum shear strain in selected (kkl) planes (all values in percent)*—Continued

	C–13	T–4	T–5	T–7	T–9	T–10	Y–1	
110	0.6428	0.8997	0.7876	0.4871	0.9897	0.4592	1.105	
101	.5091	.5130	.6997	.1269	.7608	.6150	1.053	
011	1.111	.5893	.2942	.6514	.6506	.5767	0.8014	
10$\bar{1}$	0.4952	.6535	.8288	.2002	.9360	1.032	.9735	
1$\bar{1}$0	.7825	1.035	.8854	.5285	.9974	0.5848	1.0313	
01$\bar{1}$	1.153	0.4039	.8791	.6079	.6051	.4780	0.6428	
211	0.3227	.6658	.5654	.3569	1.055	.2339	1.235	
12$\bar{1}$	.9918	.7390	.6211	.5695	0.4175	.5228	0.6689	
121	.7610	.4541	.3698	.4470	.5017	.3403	.2928	
21$\bar{1}$	.8140	.9838	.9447	.5799	1.219	.8190	1.085	
11$\bar{2}$	.9688	.9370	.8149	.5917	0.7440	.5792	0.8656	
112	.7238	.1237	.2536	.4420	.4630	.4619	.3311	
220	.6528	.8997	.7876	.4871	.9897	.4592	1.105	
200	.4419	.4509	.2832	.2532	.7542	.5320	0.7985	
020	.2452	.4174	.5023	.1572	.7788	.8399	.5884	
002	.4804	.5108	.4875	.2401	.2009	.6662	.5760	
	C–10	T–1	T–2	T–3	T–6	T–8	Y–2	Y–3
110	0.4524	0.7816	0.5563	0.7210	0.6243	0.7348	0.6651	0.7087
101	.6793	.7736	.6177	.9593	.3281	.3454	.4430	.4804
011	.8706	.6152	.8611	1.529	.6830	.4731	.4191	.7730
10$\bar{1}$	.4198	.9939	.3210	0.8630	.1042	.3429	.3513	.2494
1$\bar{1}$0	.5295	.8766	.4762	.7394	.7142	.7357	.8447	.9879
01$\bar{1}$	.9447	.2633	.7964	1.583	.8145	.6599	.6668	.8655
211	.2266	.8090	.3478	0.4126	.1927	.4397	.6087	.1599
12$\bar{1}$	.7493	.3802	.5961	1.231	.8303	.8498	.8112	.8994
121	.7278	.2247	.8226	1.181	.5518	.6042	.2327	.6648
21$\bar{1}$	.2675	1.087	.1957	0.5071	.4716	.3740	.5175	.7282
11$\bar{2}$	.6203	0.7770	.5629	.8841	.6784	.5928	.8855	1.017
112	.3051	.1367	.2497	.7456	.2683	.2349	.2010	0.3180
220	.4524	.7816	.5563	.7210	.6243	.7348	.6651	.7087
200	.5196	.6670	.4432	.7487	.4491	.4641	.7321	.4898
020	.5764	.6940	.5365	.7494	.3298	.3574	.2700	.5390
002	.3134	.4020	.3513	.1634	.3899	.2962	.7325	.6902

TABLE XVII. *Stored elastic energy and distortion numbers*

Pattern	Total stored elastic energy, W (MN/m²)	Shear stored elastic energy, W_s (MN/m¹)	$W_{s/W}$	Distortion number
U– 0	123.3	109.3	0.886	0.880
U– 1	225.5	205.4	.911	.910
U– 2	437.4	344.4	.787	.784
U– 3	244.3	156.3	.640	.837
U– 4	983.3	402.4	.409	.735
U– 5	960.0	257.1	.268	.573
U– 6	880.3	457.7	.520	.669
U– 7	151.5	126.1	.832	.892
U– 8	574.5	376.6	.656	.867
U– 9	107.6	683.0	.635	.868
U–10	132.2	676.6	.512	.824
U–11	567.4	159.1	.280	.634
U–12	104.4	102.7	.984	.951
U–13	173.6	174.1	1.0	.964
U–14	215.5	126.0	0.585	.675
U–15	236.9	731.6	.309	.589
C– 1	106.6	104.9	.984	.956
C– 2	137.1	460.9	.336	.583
C– 3	362.3	309.1	.853	.876
C– 4	364.0	324.1	.890	.967
C– 5	114.5	997.7	.871	.897
C– 6	65.3	52.1	.797	.836
C– 7	412.3	357.5	.867	.898
C– 8	330.9	247.4	.748	.907
C– 9	655.1	603.8	.922	.855
C–10	405.7	313.8	.773	.919
C–11	139.0	152.0	1.0	.878
C–12	634.4	308.3	0.486	.711
C–13	453.7	425.8	.939	.939
T– 1	627.9	482.0	.768	.889
T– 2	392.7	313.0	.797	.930
T– 3	914.8	761.4	.832	.943
T– 4	396.1	370.9	.936	.961
T– 5	336.4	347.3	1.0	.928
T– 6	390.8	281.8	0.721	.873
T– 7	165.7	150.4	.908	.845
T– 8	675.1	251.8	.373	.675
T– 9	100.2	589.6	.588	.796
T–10	560.9	506.8	.904	.883
Y–1	765.9	709.2	.926	.894
Y–2	600.4	407.5	.679	.726
Y–3	464.9	472.0	1.0	.927

58

TABLE XVIII. *Direction cosines of plane of maximum shear strain taken with respect to cubic axes*

Pattern	l_i	l_j	l_k	Pattern	l_i	l_j	l_k
U– 0	−0.117	0.180	0.977	T– 1	.955	−0.057	0.291
U– 1	− .566	−0.774	−0.284	T– 2	−0.520	− .765	.381
U– 2	0.085	− .366	0.926	T– 3	− .468	− .884	−0.008
U– 3	.085	− .366	.926	T– 3	− .468	− .884	− .008
U– 7	.628	0.126	−0.730	T– 5	0.866	0.297	0.403
U– 9	.455	.161	− .876	T– 6	−0.465	−0.778	−0.424
U–10	−0.002	−0.917	− .399	T– 7	− .551	0.720	− .421
U–12	− .333	− .940	− .070	T– 9	0.863	−0.195	0.466
U–13	− .248	0.518	− .819	T–10	−0.424	− .096	−0.901
				T– 4	0.947	0.057	0.317
C– 1	− .396	−0.918	− .004				
C– 3	− .365	0.102	0.925	Y– 1	.802	−0.543	.249
C– 4	− .274	−0.948	−0.130	Y– 3	−0.453	− .871	−0.190
C– 5	− .289	− .922	− .256				
C– 6	0.008	0.147	0.989				
C– 7	−0.282	−0.925	−0.254				
C– 8	− .238	− .833	− .499				
C– 9	0.882	0.465	− .081				
C–10	−0.478	−0.874	0.088				
C–13	0.886	0.054	−0.460				
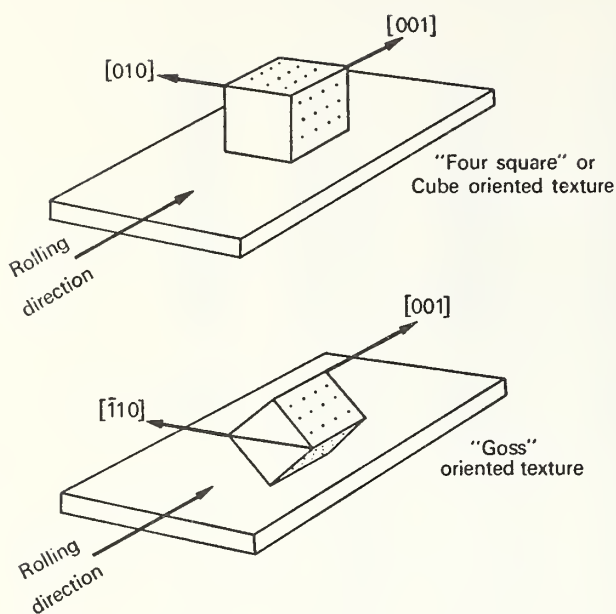
FIGURE 1. *Schematic representation of orientation relations in Goss and cube textures in Fe-3 Si.*
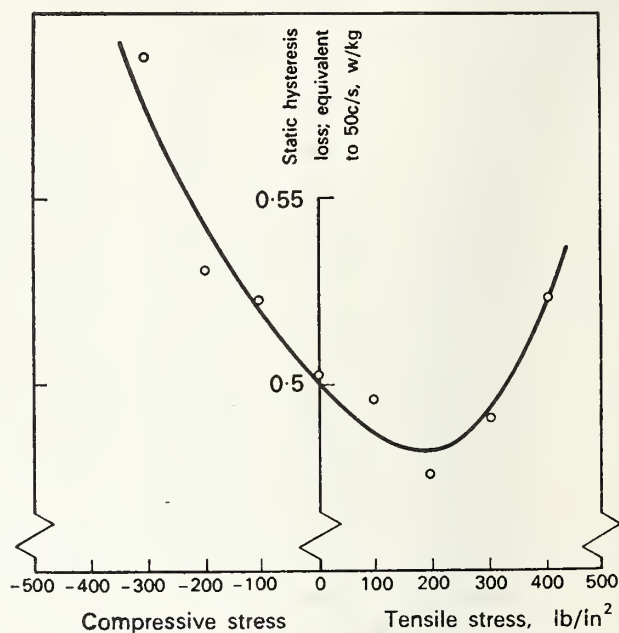
FIGURE 2b. *Static hysteresis loss versus macrostress. Induction 15,000 gauss (After Ref. [4]).*
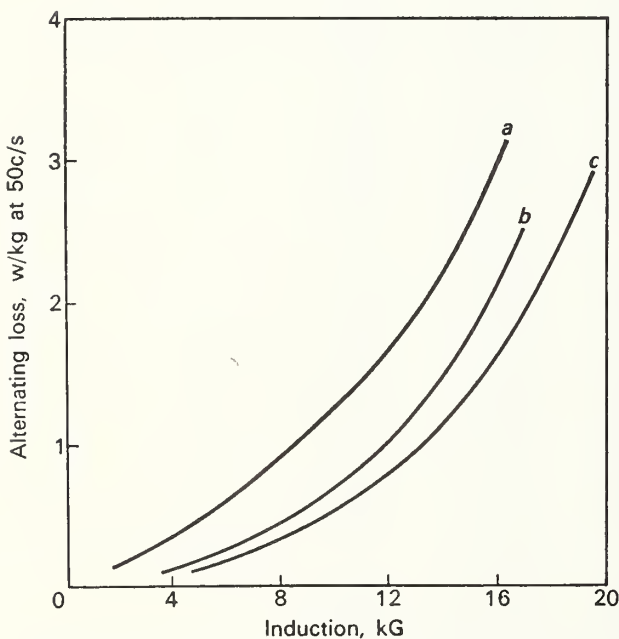
FIGURE 2a. *Alternating power loss versus induction in Goss Fe-3 Si (a) at grain boundary; (b) at a misaligned grain and (c) average in the sheet (After Ref. [5]).*
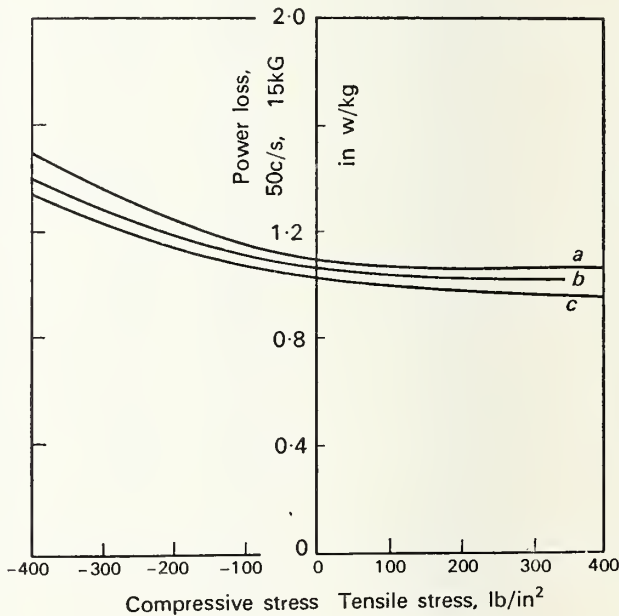
FIGURE 2c. *Variation of total power loss versus macrostress. Induction 15,000 gauss. (a) 20 °C; (b) 200 °C; (c) 300 °C. (After Ref. [4]).*

60

INGOT: 3% Si, 0.15% Mn, 0.03% C, 0.03% S

↓

NOT ROLL TO 0.08 TO 0.1 INCN TNICKNESS

↓

PICKLE ANO OESCALE

↓

COLO ROLL

↓

PROCESS ANNEAL at 900° C

↓

COLO ROLL: FINAL PASS GIVES ABOUT 60% REOUCTION

↓

STRIP 12-13 MILS THICK

↓

PRIMARY RECRYSTALLIZATION OECARBURIZATION att 800° C (WET N_2)

↓

COAT WITN M_g (OH)$_2$ (INSULATES ANO PREVENTS RUST

↓

8ATCH ANNEAL at 1200° C IN VACUUM ———— SOAK at 1200° C TWO HOURS TO

SECONOARY RECRYSTALLIZATION GIVES [110] 001   OESULFURIZE

TEXTURE   ↓

                                               COOL at 25° C PER HOUR

                                                      ↓

THERMAL FLATTENING (TENSILE STRESS APPLIEO ———— COAT WITN PNOSPHATE

AT ABOUT 350° C)

↓

COILS FOR SNIPMENT ———— CUT TO FINAL SIZE

↓   ↓

STRESS RELIEF ANNEAL (UNIFORM HEAT ANO COOL TO MINIMIZE TNERMAL STRESSES)

↓

USE

FIGURE 3. *Flow diagram for the preparation of Goss textured Fe-3 Si sheet.*
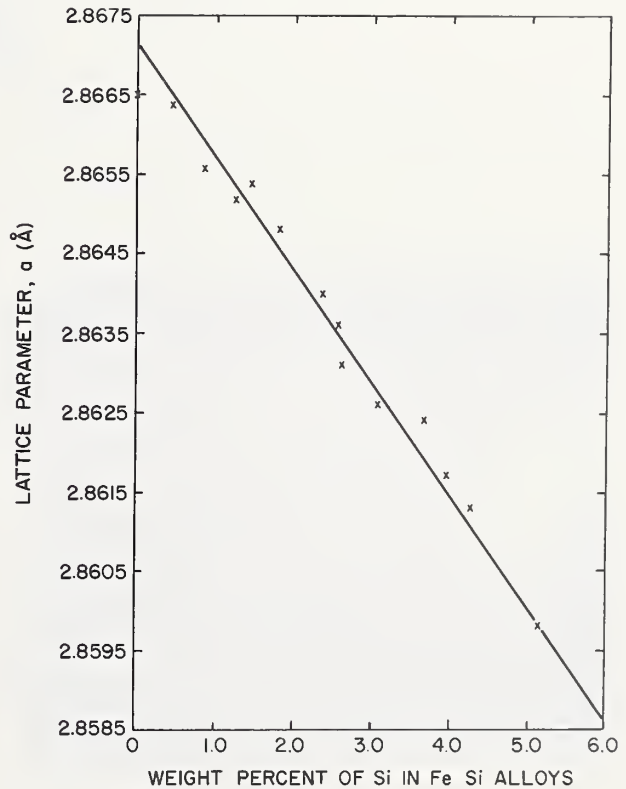
FIGURE 4. *Lattice parameter, a, in Fe-Si alloys versus weight percentage of silicon. Line is least squares fit to data shown:* $a = 2.86719 - 0.144224 \ C_{Si}$.

61
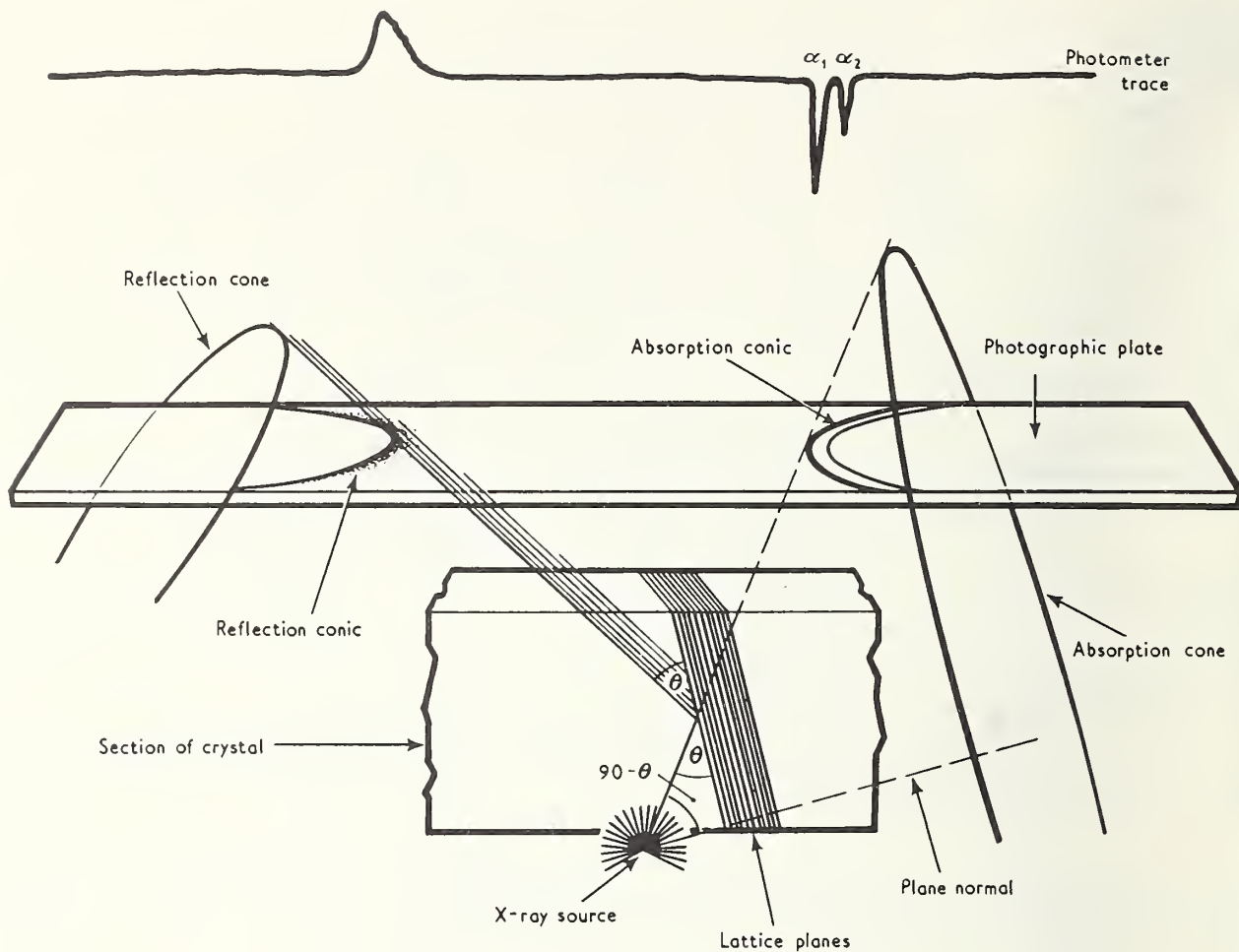
FIGURE 5. *Formation of Kossel conics.*
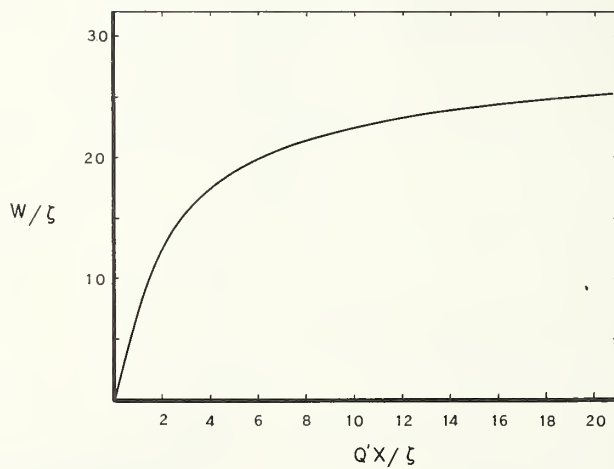
FIGURE 6. *Integrated reflection in transmission: Darwin solution for a Gaussian mosaic spread, ξ. (After Ref. [22].*.

62

FIGURE 7. *Gnomonic projections of points m, z, n into m', z', n' respectively.*

FIGURE 8a. *Stereographic projection of conics from an iron target diffracting Fe-Kα₁ radiation. ⟨110⟩ pole at center.*

FIGURE 8b. *Indexed pattern from Fe-3 Si sheet. Pattern taken at geometric center of grain shown in figure 24.*

63
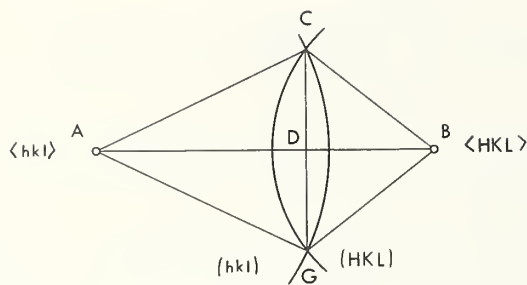
$$\cos^2 CD = \cos^2 \gamma = \cos^2 AC + \left[\frac{\cos BC - (\cos AB)(\cos AC)}{\sin AB} \right]^2$$

$$\cos(90-\theta)_{HKL} = \frac{\lambda (H^2 + K^2 + L^2)^{1/2}}{2a} = \frac{\lambda H_0}{2a} = \cos BC$$

$$\cos(90-\theta)_{hkl} = \frac{\lambda_1 (h^2 + k^2 + l^2)^{1/2}}{2a} = \frac{\lambda_1 h_0}{2a} = \cos AC$$

$$\cos AB = \frac{Hh + Kk + Ll}{H_0 h_0} = \cos \beta$$

$$a = f \sec \gamma$$

FIGURE 9. *Lens method for cubic lattice parameter determination. The value of "f" depends only on the wavelength and indices of the participating conics (After Ref. [37]).*
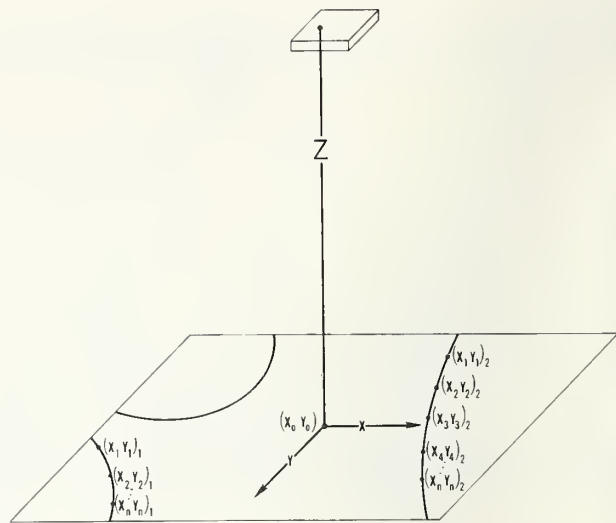
FIGURE 10. *Schematic of coordinate system for the RACE method.*

Effect of Error in Determining Z on the d Values in Fe-3Si
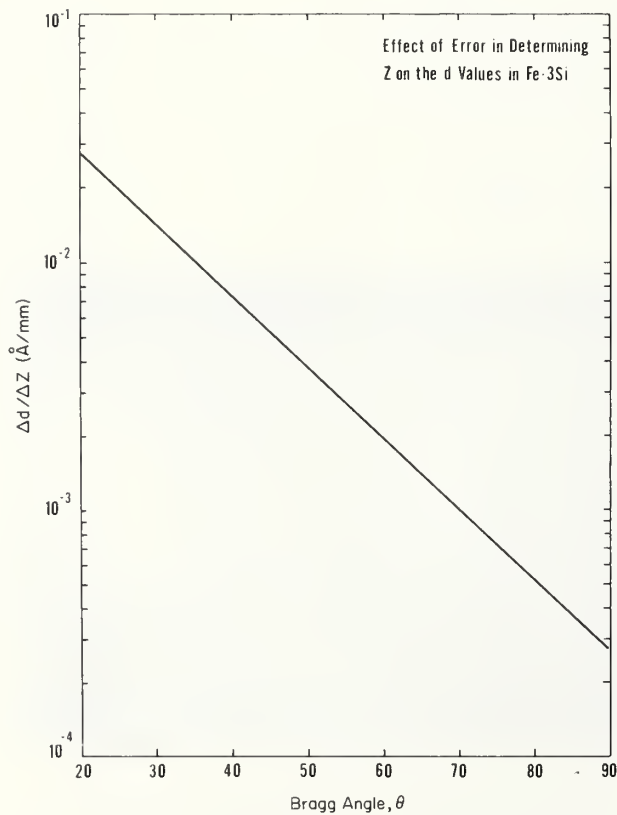
FIGURE 11a. *Effect of error in Z on the d spacing values in Fe-3 Si.*

Effect of Radial Error (Δr) in Locating Pattern Center
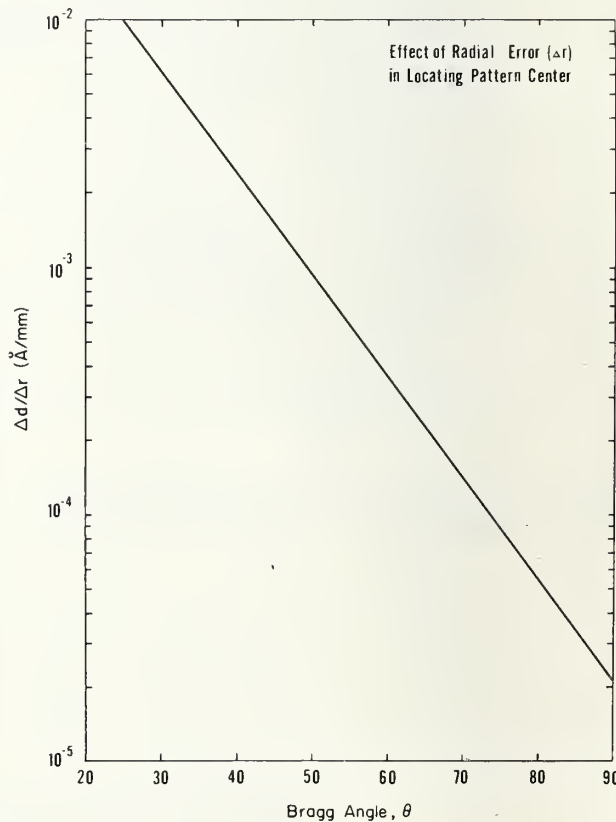
FIGURE 11b. *Effect of a radial error, Δr, in determining the pattern center on the d spacing values in Fe-3 Si.*
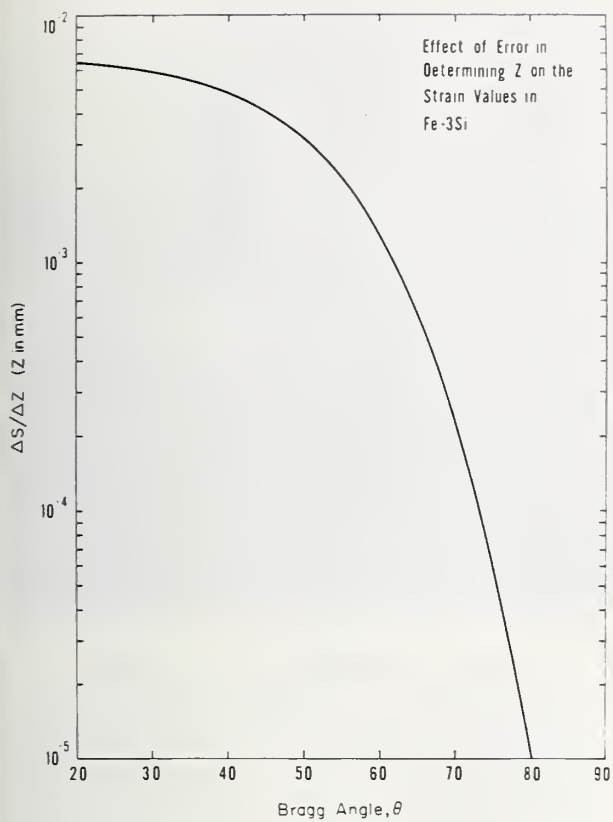
FIGURE 12. *Effect of error in Z on $\Delta d/d_0$ values in Fe-3 Si.*

FIGURE 14. *Kossel camera module, bottom view.*
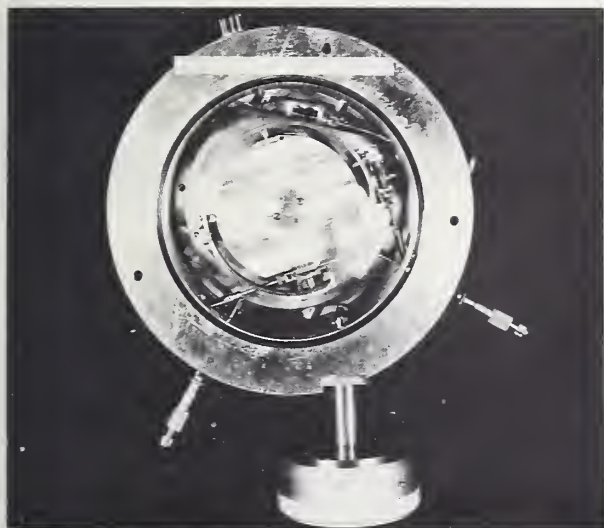
FIGURE 13. *Kossel camera module. Note linkages for X, Y, Z and goniometric drives.*
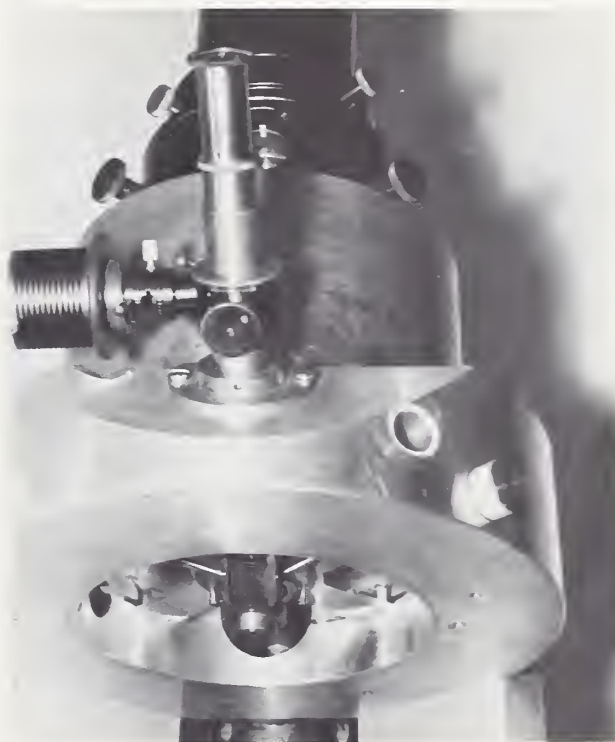
FIGURE 15. *Light optical system for Kossel pattern generator.*

65
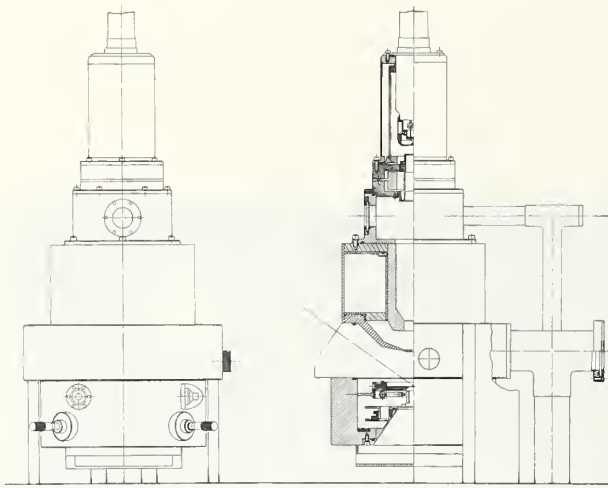
FIGURE 16a. *Schematic cross-section of Kossel pattern generator.*
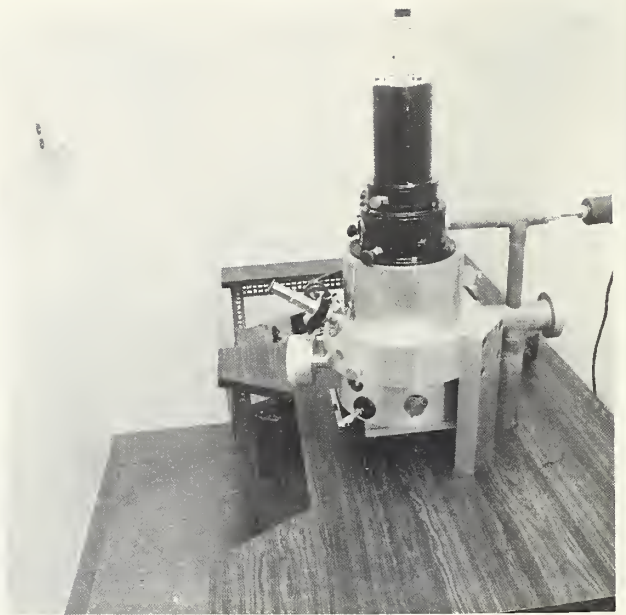
FIGURE 16b. *Assembled Kossel pattern generator.*
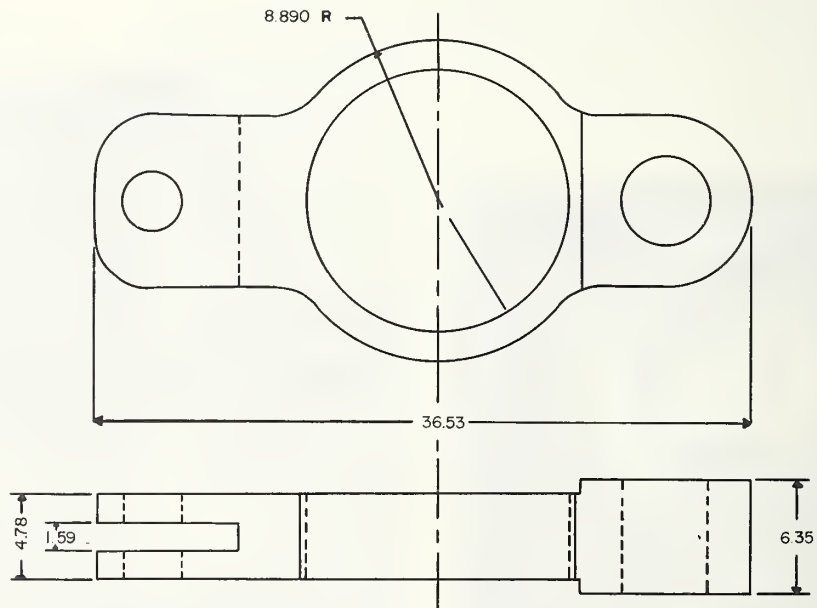
FIGURE 17. *Load cell for Kossel camera module. Dimensions in millimeters.*

66
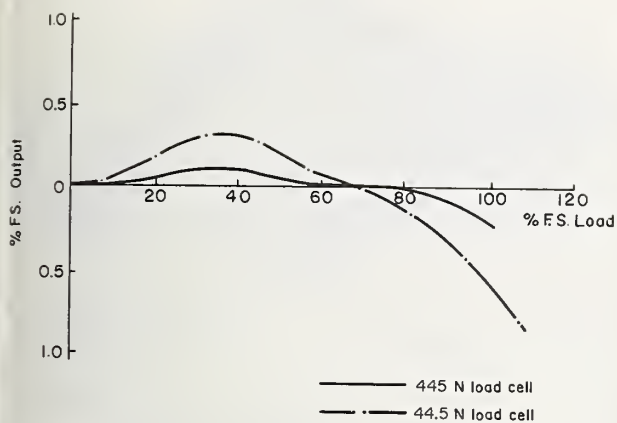
FIGURE 18. *Calibration curves for load cells.*

— 445 N load cell
—·—·— 44.5 N load cell

FIGURE 19a. *Loading device mounted in Kossel camera. Readout unit is at rear.*

SECTION A-A
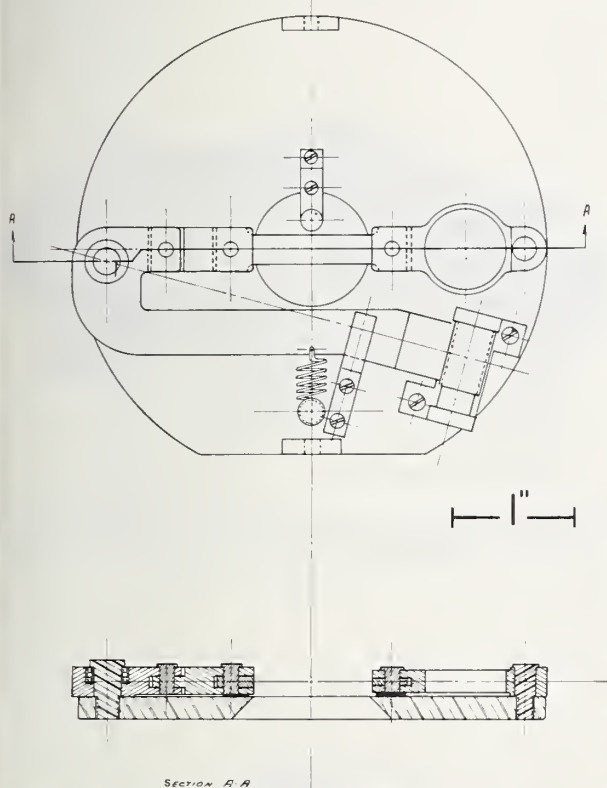
FIGURE 19b. *Schematic of loading device.*
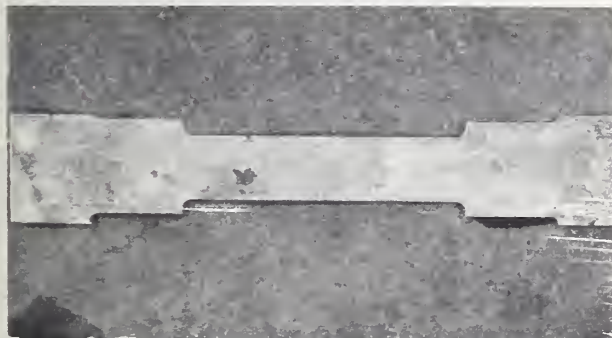
FIGURE 20. *Typical specimen of Fe-3 Si sheet prior to insertion into the loading device. ×2.*
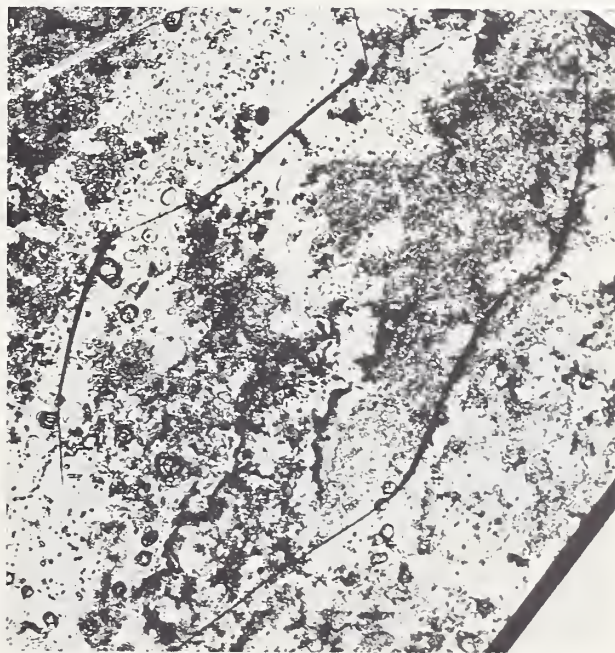
FIGURE 21. *Enlarged view of typical grain in Fe-3 Si sheet. Note surface roughness. ×100.*

67

FIGURE 22. *Scanning electron microscope photograph near grain boundary in Fe-3 Si sheet. Note terraced effect. ×2600 (40° tilt, 20 kV).*
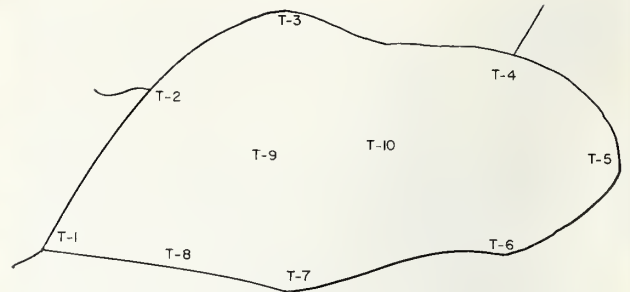
FIGURE 25. *Key to Kossel pattern locations in low tensile load (Load III).*
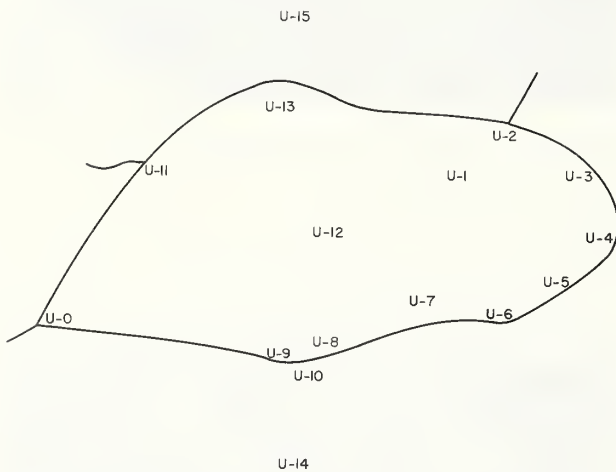
FIGURE 23. *Key to Kossel pattern locations in unstrained condition (Level I).*

LATTICE PARAMETER, Å

○ 2.86075-2.86124   2.86225-2.86274   2.86375-2.86424
2.86125-2.86174   2.86275-2.86324   2.86425-2.86475
2.86175-2.86224   2.86325-2.86374
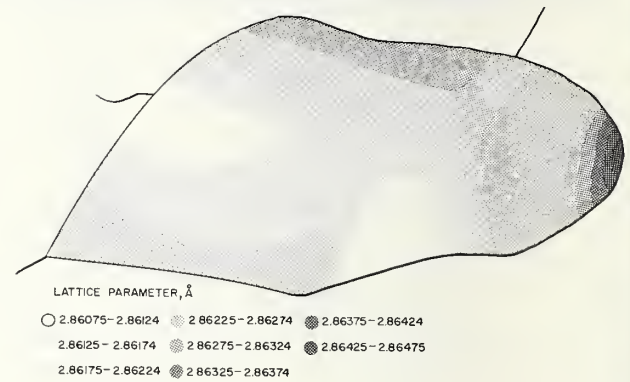
FIGURE 26. *Variation of lattice parameter as a function of position in grain, Level I.*
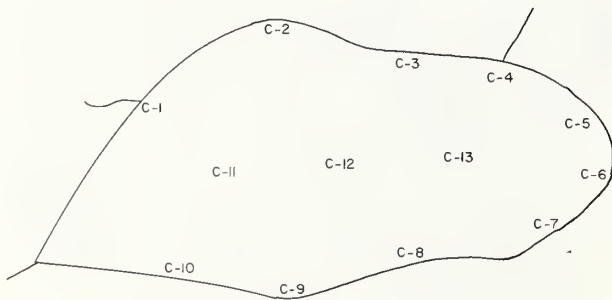
FIGURE 24. *Key to Kossel pattern locations in compressed condition (Level II).*

% STRAIN
○ 0.2 >   0.5-0.6
   0.2-0.3   0.6-0.7
   0.3-0.4   0.7-0.8
   0.4-0.5 ● >0.8
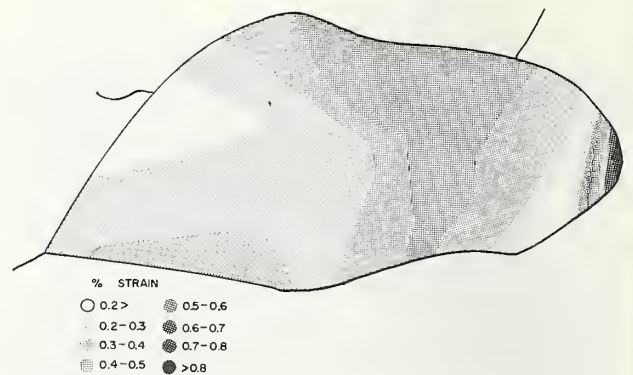
FIGURE 27a. *Maximum principal strain as a function of position in grain, Level I.*

68

% STRAIN

○ 0.2   ░ 0.4-0.5
0.2-0.3   ▒ 0.5-0.6
0.3-0.4   ● 0.6-0.7
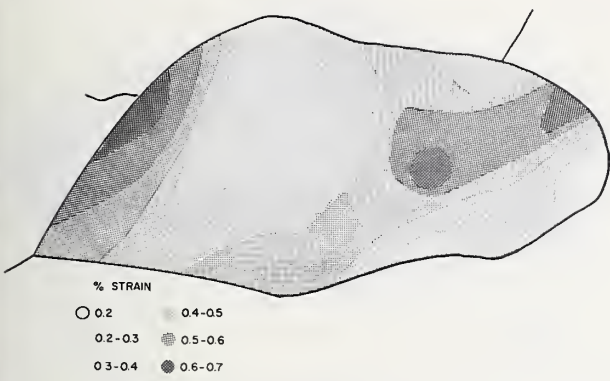
FIGURE 27b. *Maximum principal strain as a function of position in grain, Level II.*

% STRAIN

○ -0.45→-0.3   ░ -0.1→0
-0.3→-0.2   ▒ 0→0.1
-0.2→-0.1   ● 0.1→0.2
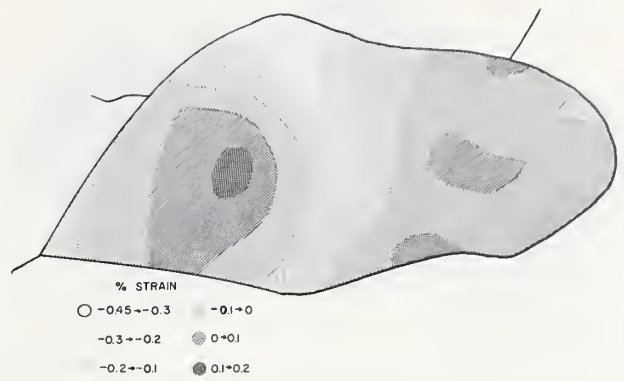
FIGURE 28b. *Intermediate principal strain as a function of position in grain, Level II.*

% STRAIN

○ 0.2>   ▒ 0.5-0.6
0.2-0.3   ● 0.6-0.7
0.3-0.4   ● 0.7-0.8
░ 0.4-0.5   ● >0.8
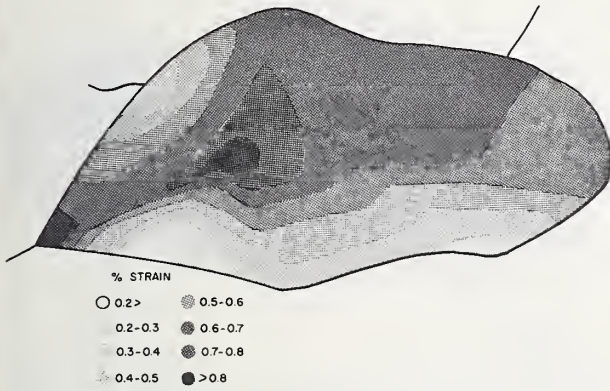
FIGURE 27c. *Maximum principal strain as a function of position in grain, Level III.*

% STRAIN

-.3,-.2   ▒ 0.1→0.2
-.2,-.1
▒ -.1→0
▒ 0→0.1
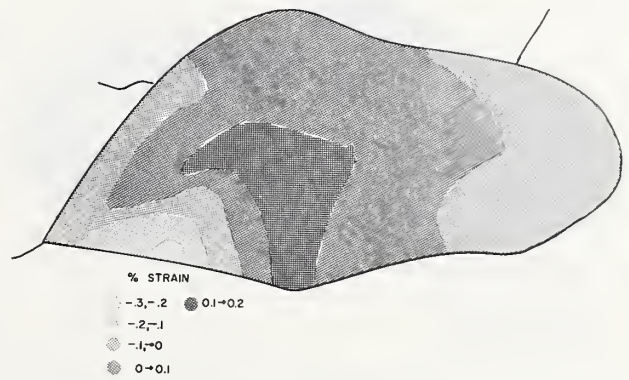
FIGURE 28c. *Intermediate principal strain as a function of position in grain, Level III.*

% STRAIN

○ -4→-3   ▒ 0→1
-3→-2   ▒ 0.1→0.2
-.2→-.1   ▒ 0.2→0.3
░ -.1→0
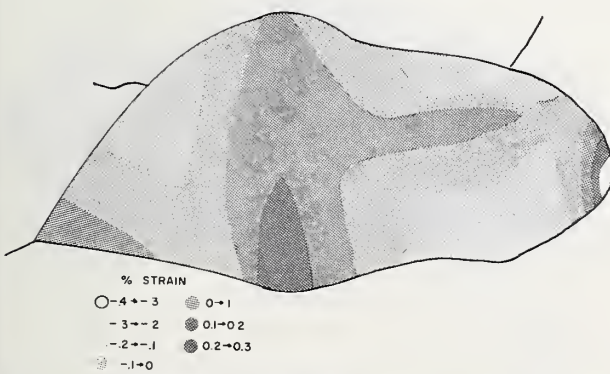
FIGURE 28a. *Intermediate principal strain as a function of position in grain, Level I.*

% STRAIN (ALL SIGNS NEGATIVE)

○ 0.2>   ▒ 0.5-0.6
0.2-0.3   ● 0.6-0.7
0.3-0.4   ● 0.7-0.8
░ 0.4-0.5
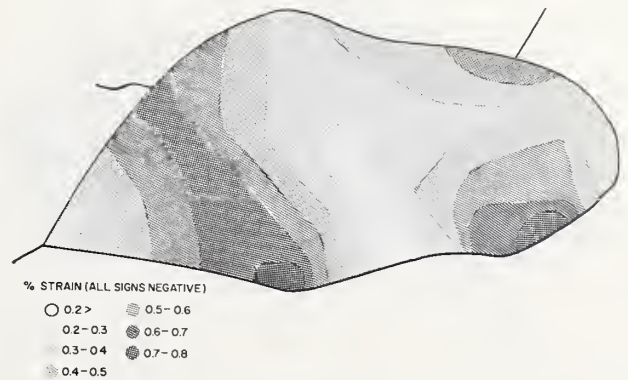
FIGURE 29a. *Minimum principal strain as a function of position in grain, Level I.*

69

% STRAIN (ALL SIGNS NEGATIVE)
  0.2-0.3   0.6-0.7
  0.3-0.4   0.7-0.8
  0.4-0.5   0.8-0.9
  0.5-0.6   >0.9
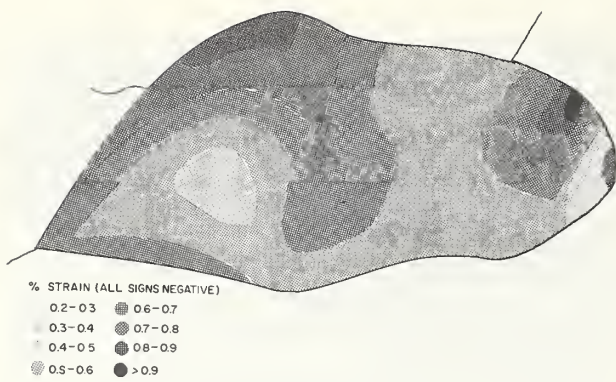
FIGURE 29b. *Minimum principal strain as a function of position*

STRESS: GN/m²
  -1→0
  0→1
  1→2

FIGURE 30b. *Maximum principal stress in GN/m² as a function of position in grain, Level II.*

% STRAIN (ALL SIGNS NEGATIVE)
  0.3-0.4   0.7-0.8
  0.4-0.5   0.8-0.9
  0.5-0.6   >0.9
  0.6-0.7
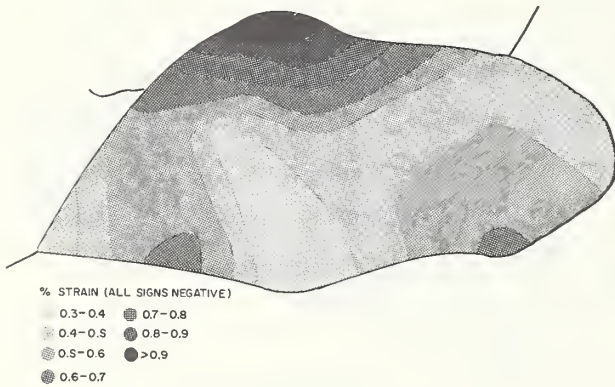
FIGURE 29c. *Minimum principal strain as a function of position in grain, Level III.*

STRESS: GN/m²
  -1→0
  0→1
  1→2
  2→3
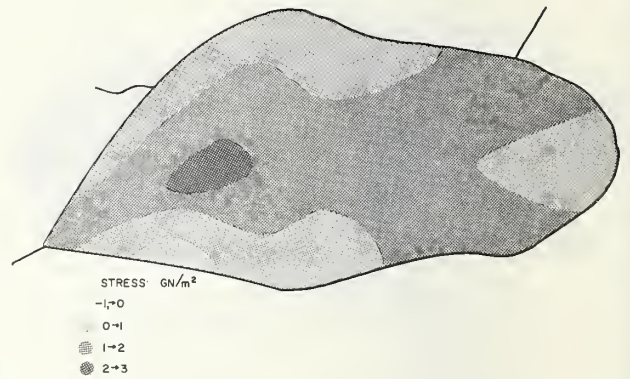
FIGURE 30c. *Maximum principal stress in GN/m² as a function of position in grain, Level III.*

STRESS: GN/m²
  -2,-1   2→3
  -1→0
  0→1
  1→2
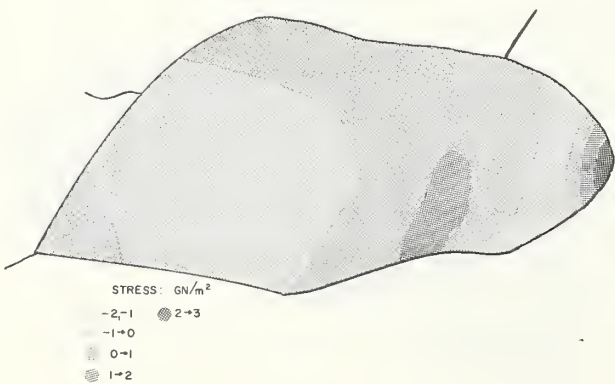
FIGURE 30a. *Maximum principal stress in GN/m² as a function of position in grain, Level I.*

STRESS: GN/m²
  -2,-1   2→3
  -1→0
  0→1
  1→2
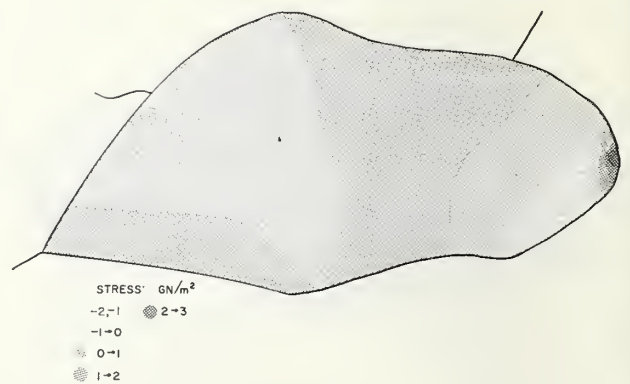
FIGURE 31a. *Intermediate principal stress in GN/m² as a function of position in grain, Level I.*
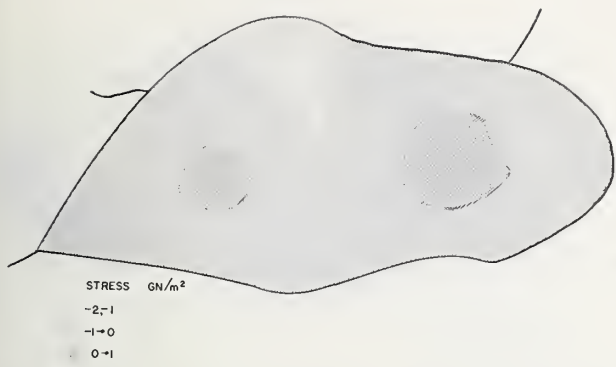
FIGURE 31b. *Intermediate principal stess in GN/m² as a function of position in grain, Level II.*
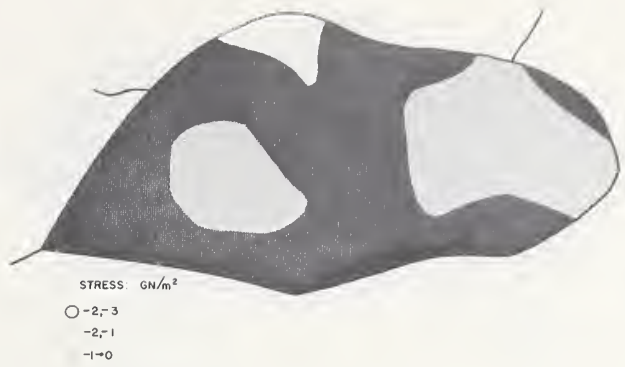
FIGURE 32b. *Minimum principal stress in GN/m² as a function of position in grain, Level II.*
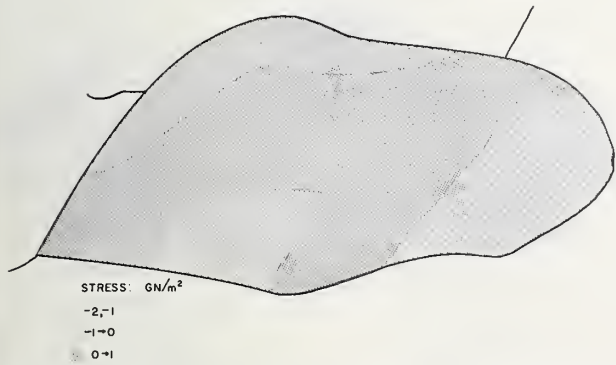
FIGURE 31c. *Intermediate principal stress in GN/m² as a function of position in grain, Level III.*
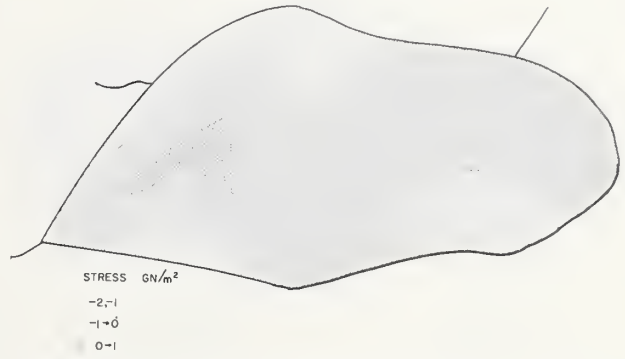
FIGURE 32c. *Minimum principal stress in GN/m² as a function of position in grain, Level II.*
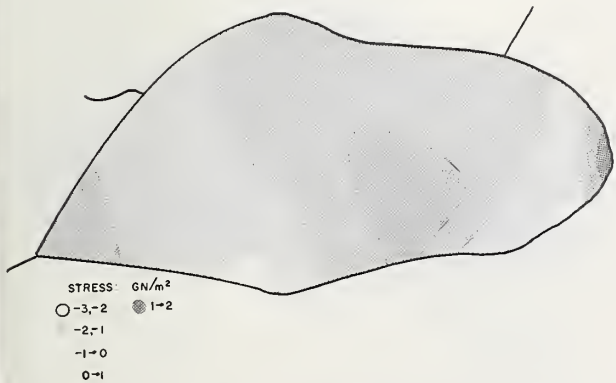
FIGURE 32a. *Minimum principal stress in GN/m² as a function of position in grain, Level I.*
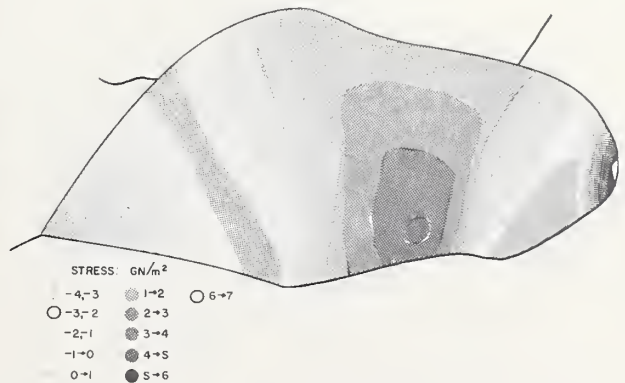
FIGURE 33a. *Algebraic sum of the three principal stresses, in GN/m², as a function of position in grain Level I.*

71
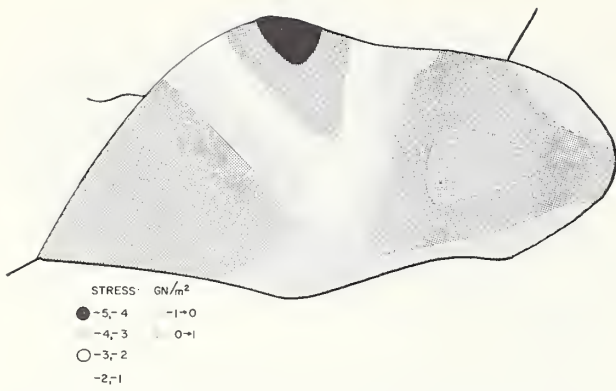
FIGURE 33b. *Algebraic sum of the three principal stessses, in GN/m², as a function of position in grain, Level II.*

FIGURE 35a. *Total stored elastic energy, W, in MN/m² × 10⁻², as a function of position in grain, Level I.*
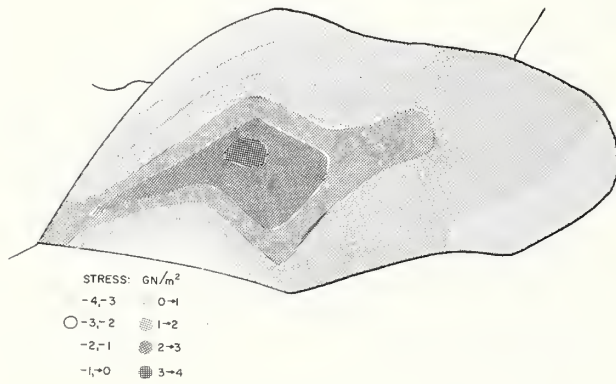
FIGURE 33c. *Algebraic sum of the three principal stresses, in GN/m², as a function of position in grain, Level III.*
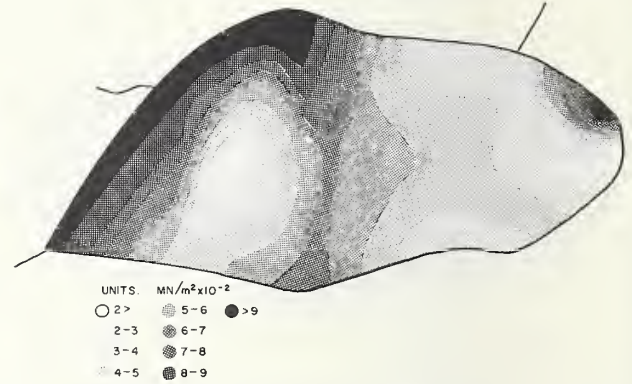
FIGURE 35b. *Total stored elastic energy, W, in MN/m² × 10⁻², as a function of position in grain, Level II.*
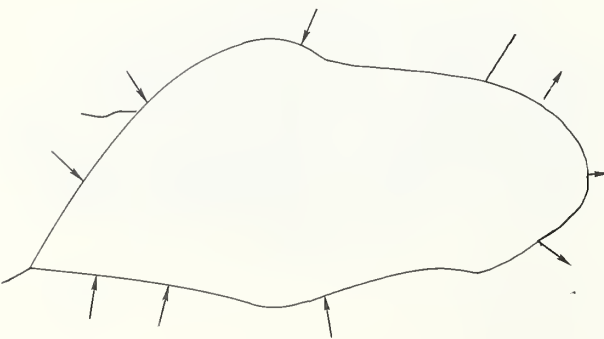
FIGURE 34. *Schematic view of stresses on grain.*
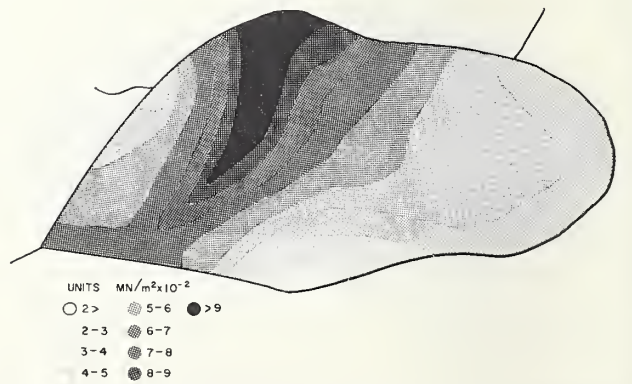
FIGURE 35c. *Total stored elastic energy, W, in MN/m² × 10⁻², as a function of position in grain, Level III.*

FIGURE 36a. *Shear stored elastic energy, W_s, in $MN/m^2 \times 10^{-2}$, as a function of position in grain, Level I.*
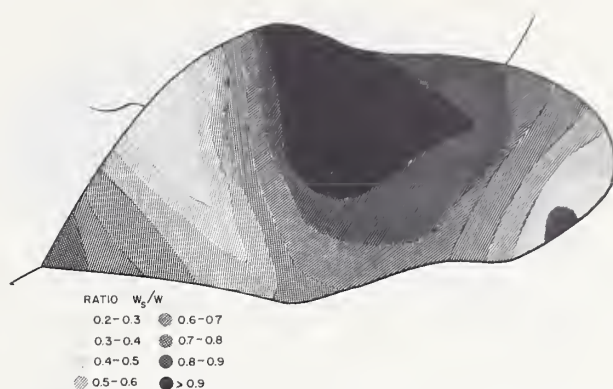
FIGURE 37a. *Ratio of Ws/W as a function of position in grain, Level I.*
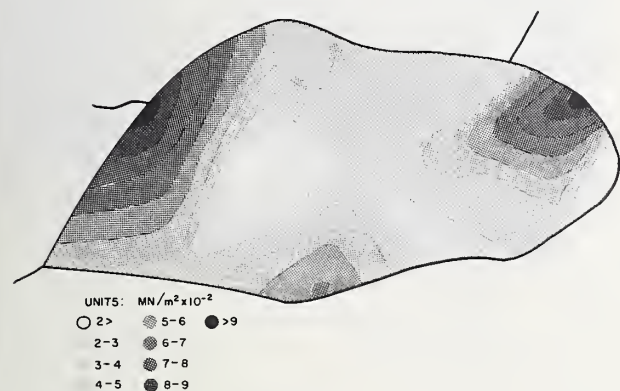
FIGURE 36b. *Shear stored elastic energy, W_s, in $MN/m^2 \times 10^{-2}$, as a function of position in grain, Level II.*
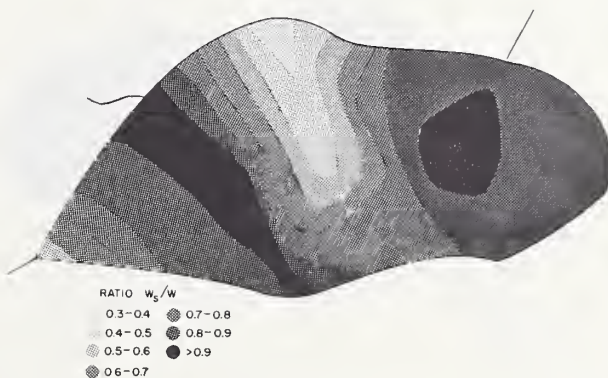
FIGURE 37b. *Ratio of Ws/W as a function of position in grain, Level II.*
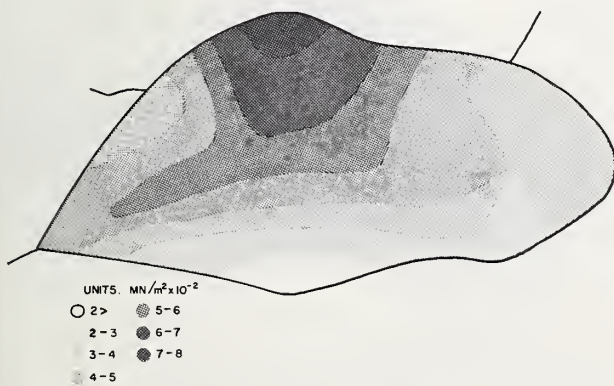
FIGURE 36c. *Shear stored elastic energy, W_s, in $MN/m^2 \times 10^{-2}$, as a function of position in grain, Level III.*
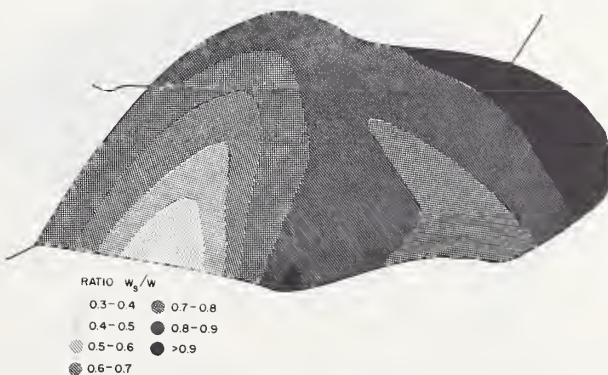
FIGURE 37c. *Ratio of Ws/W as a function of position in grain, Level III.*

73
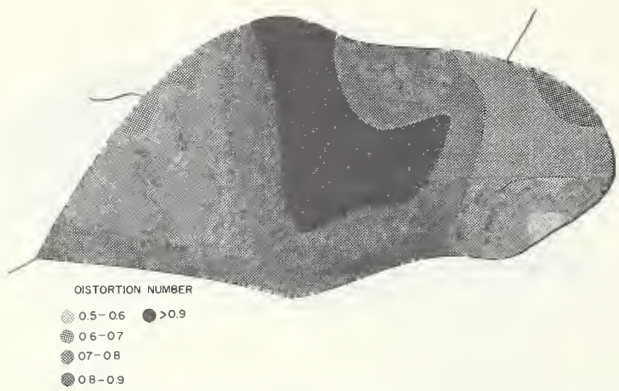
FIGURE 38a. *Distortion number as a function of position in grain, Level I.*
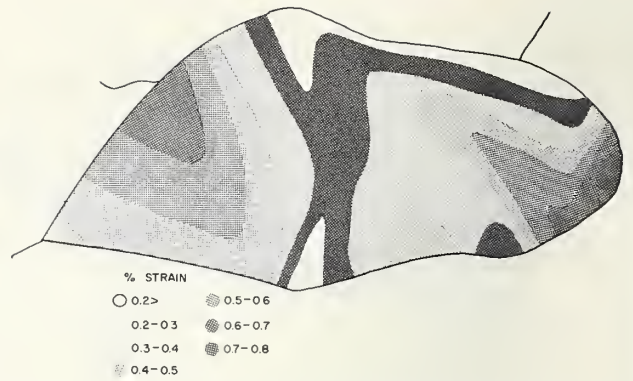
FIGURE 39a. *Absolute value of the maximum shear strain in the (112) plane as a function of position in grain, Level I.*
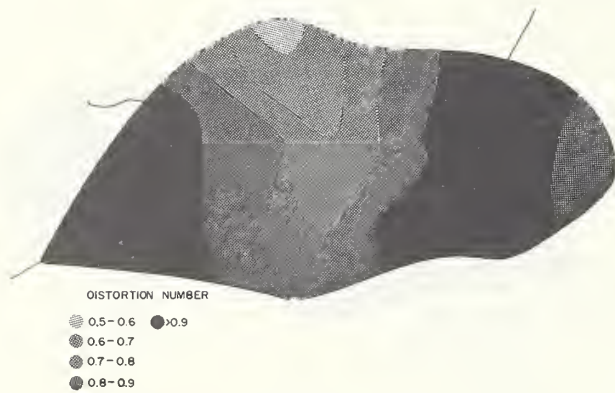
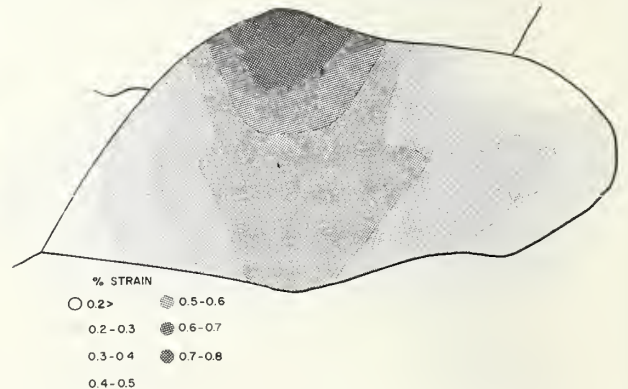FIGURE 38b. *Distortion number as a function of position in grain, Level II.*

FIGURE 39b. *Absolute value of the maximum shear strain in the (112) plane as a function of position in grain, Level II.*
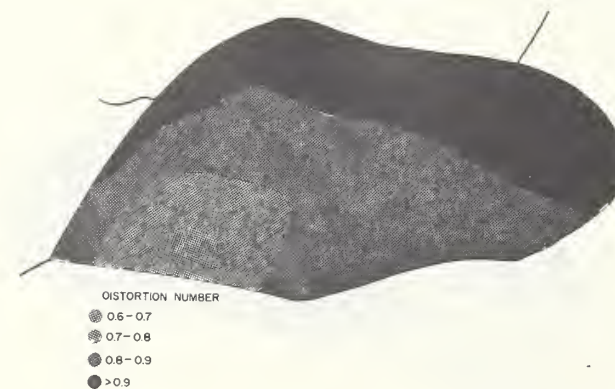
FIGURE 38c. *Distortion number as a function of position in grain, Level III.*

FIGURE 39c. *Absolute value of the maximum shear strain in the (112) plane as a function of position in grain, Level III.*

FIGURE 40. *Double pattern obtained near grain boundary. Mis-alignment is more than 3° of arc.*
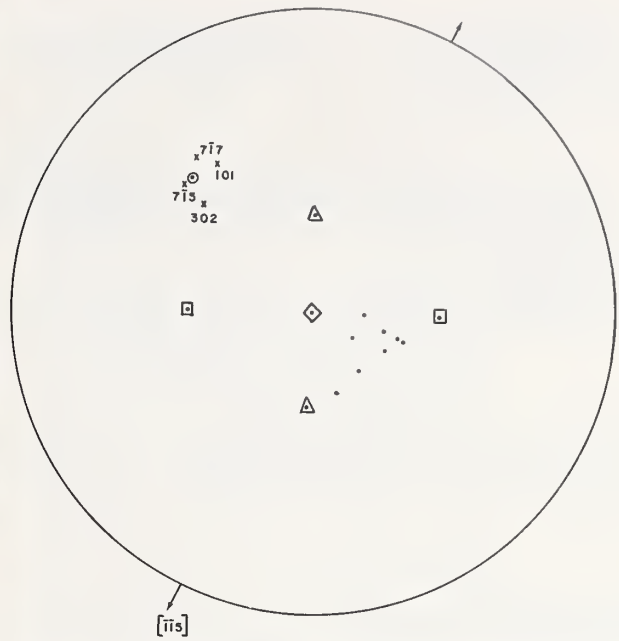
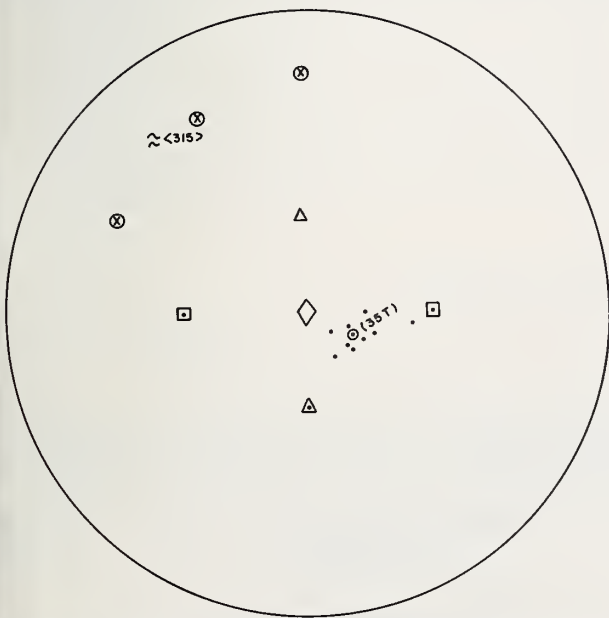FIGURE 41b. ⟨110⟩ *Stereographic plot of data in table XVIII for Level II, the line is at 31° to the {100} zone.*

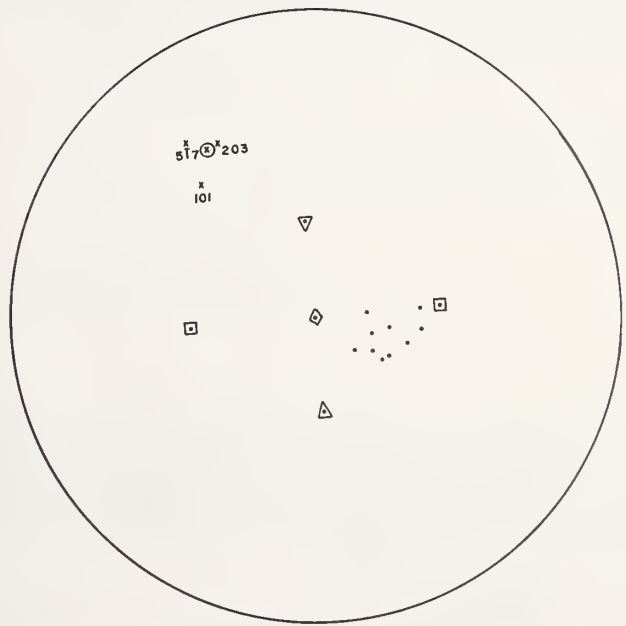FIGURE 41a. ⟨110⟩ *Stereographic plot of data in table XVIII for Level I, the line is at 31° to the {100} zone.*

FIGURE 41c. ⟨110⟩ *Stereographic plot of data in table XVIII for Level III, the line is at 31° to the {100} zone.*

U.S. DEPT. OF COMM. BIBLIOGRAPHIC DATA SHEET	1. PUBLICATION OR REPORT NO. NBS MN-130	2. Gov't Accession No.	3. Recipient's Accession No.
4. TITLE AND SUBTITLE The Divergent Beam (Kossel) X-Ray Method and its Uses in Measuring Strain Contours in an Individual Grain of Fe-3 Weight Percent Si Transformer Sheet		5. Publication Date August 1973	
		6. Performing Organization Code	
7. AUTHOR(S) Harvey Yakowitz		8. Performing Organization	
9. PERFORMING ORGANIZATION NAME AND ADDRESS NATIONAL BUREAU OF STANDARDS DEPARTMENT OF COMMERCE WASHINGTON, D.C. 20234		10. Project/Task/Work Unit No. 3120137	
		11. Contract/Grant No.	
12. Sponsoring Organization Name and Address Same as No. 9		13. Type of Report & Period Covered Final	
		14. Sponsoring Agency Code	

15. SUPPLEMENTARY NOTES

16. ABSTRACT (A 200-word or less factual summary of most significant information. If document includes a significant bibliography or literature survey, mention it here.)

Residual and impressed stresses and strains in Fe-3 wt. pct. Si alloy transformer sheet were studied. Results were obtained by the divergent beam (Kossel) x-ray microdiffraction techniques. The optically opaque Fe-3 wt. pct. Si alloy was mapped for residual and impressed stresses and strains. These maps are roughly analogous to polarized light stress analysis of transparent materials. The results showed that a variable strain distribution existed in the alloy sheet at the time it was ready for insertion into a transformer core. Small applied compressive and tensile loads tended to rearrange this variable strain distribution but not to appreciably alter the total stored elastic energy.

17. KEY WORDS (Alphabetical order, separated by semicolons) Divergent beam x-ray diffraction; electron probe microanalysis; iron-silicon alloy; Kossel; strain; stress; transformer sheet.

18. AVAILABILITY STATEMENT	19. SECURITY CLASS (THIS REPORT)	21. NO. OF PAGES
[X] UNLIMITED.	UNCLASSIFIED	80
[ ] FOR OFFICIAL DISTRIBUTION. DO NOT RELEASE TO NTIS.	20. SECURITY CLASS (THIS PAGE)	22. Price
	UNCLASSIFIED	95 cents

USCOMM-DC 66244-P71

NBS TECHNICAL PUBLICATIONS

PERIODICALS

JOURNAL OF RESEARCH
reports National Bureau of Standards research and development in physics, mathematics, and chemistry. Comprehensive scientific papers give complete details of the work, including laboratory data, experimental procedures, and theoretical and mathematical analyses. Illustrated with photographs, drawings, and charts. Includes listings of other NBS papers as issued.

Published in two sections, available separately:

• Physics and Chemistry (Section A)

Papers of interest primarily to scientists working in these fields. This section covers a broad range of physical and chemical research, with major emphasis on standards of physical measurement, fundamental constants, and properties of matter. Issued six times a year. Annual subscription: Domestic, $17.00; Foreign, $21.25.

• Mathematical Sciences (Section B)

Studies and compilations designed mainly for the mathematician and theoretical physicist. Topics in mathematical statistics, theory of experiment design, numerical analysis, theoretical physics and chemistry, logical design and programming of computers and computer systems. Short numerical tables. Issued quarterly. Annual subscription: Domestic, $9.00; Foreign, $11.25.

TECHNICAL NEWS BULLETIN

The best single source of information concerning the Bureau's measurement, research, developmental, co-operative, and publication activities, this monthly publication is designed for the industry-oriented individual whose daily work involves intimate contact with science and technology—*for engineers, chemists, physicists, research managers, product-development managers, and company executives.* Includes listing of all NBS papers as issued. Annual subscription: Domestic, $6.50; Foreign, $8.25.

NONPERIODICALS

Applied Mathematics Series. Mathematical tables, manuals, and studies.

Building Science Series. Research results, test methods, and performance criteria of building materials, components, systems, and structures.

Handbooks. Recommended codes of engineering and industrial practice (including safety codes) developed in cooperation with interested industries, professional organizations, and regulatory bodies.

Special Publications. Proceedings of NBS conferences, bibliographies, annual reports, wall charts, pamphlets, etc.

Monographs. Major contributions to the technical literature on various subjects related to the Bureau's scientific and technical activities.

National Standard Reference Data Series. NSRDS provides quantitative data on the physical and chemical properties of materials, compiled from the world's literature and critically evaluated.

Product Standards. Provide requirements for sizes, types, quality, and methods for testing various industrial products. These standards are developed cooperatively with interested Government and industry groups and provide the basis for common understanding of product characteristics for both buyers and sellers. Their use is voluntary.

Technical Notes. This series consists of communications and reports (covering both other-agency and NBS-sponsored work) of limited or transitory interest.

Federal Information Processing Standards Publications. This series is the official publication within the Federal Government for information on standards adopted and promulgated under the Public Law 89–306, and Bureau of the Budget Circular A–86 entitled, Standardization of Data Elements and Codes in Data Systems.

Consumer Information Series. Practical information, based on NBS research and experience, covering areas of interest to the consumer. Easily understandable language and illustrations provide useful background knowledge for shopping in today's technological marketplace.

BIBLIOGRAPHIC SUBSCRIPTION SERVICES

The following current-awareness and literature-survey bibliographies are issued periodically by the Bureau:

Cryogenic Data Center Current Awareness Service (Publications and Reports of Interest in Cryogenics). A literature survey issued weekly. Annual subscription: Domestic, $20.00; foreign, $25.00.

Liquefied Natural Gas. A literature survey issued quarterly. Annual subscription: $20.00.

Superconducting Devices and Materials. A literature survey issued quarterly. Annual subscription: $20.00. Send subscription orders and remittances for the preceding bibliographic services to the U.S. Department of Commerce, National Technical Information Service, Springfield, Va. 22151.

Electromagnetic Metrology Current Awareness Service (Abstracts of Selected Articles on Measurement Techniques and Standards of Electromagnetic Quantities from D-C to Millimeter-Wave Frequencies). Issued monthly. Annual subscription: $100.00 (Special rates for multi-subscriptions). Send subscription order and remittance to the Electromagnetic Metrology Information Center, Electromagnetics Division, National Bureau of Standards, Boulder, Colo. 80302.

Order NBS publications (except Bibliographic Subscription Services) from: Superintendent of Documents, Government Printing Office. Washington, D.C. 20402.